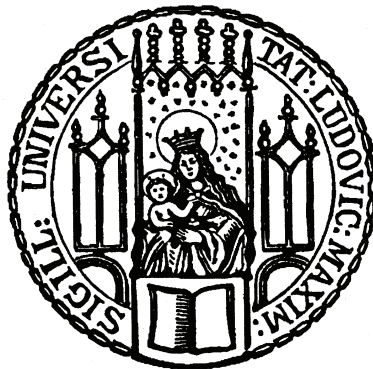# Multilayer Mirrors for Attosecond Pulse Shaping between 30 and 200 eV

Michael Hofstetter

München 2011

Multilayer Mirrors for Attosecond Pulse Shaping between 30 and 200 eV

Michael Hofstetter

Dissertation
an der Fakultät für Physik
der Ludwig–Maximilians–Universität
München

vorgelegt von
Michael Hofstetter
aus Regensburg, Deutschland

2011

To Elena

Abstract

Attosecond (as) physics has become a wide spreaded and still growing research field over the last decades. It allows for probing and controlling core- and outer shell electron dynamics with never before achieved temporal precision.

High harmonic generation in gases in combination with advanced extreme ultraviolet (XUV) optical components enable the generation of *isolated* attosecond pulses as required for absolute time measurements. But until recently, single attosecond pulse generation has been restricted to the energy range below 100 eV due to the availability of sources and attosecond optics. Multilayer mirrors are the up to date widest tunable optical components in the XUV and key components in attosecond physics from the outset.

In this thesis, the design, fabrication and measurement of periodic and aperiodic XUV multilayer mirrors and their application in the generation and shaping of isolated attosecond pulses is presented. Two- and three material coatings based on a combination of molybdenum, silicon, boron carbide, lanthanum and scandium covering the complete spectral range between 30 and 200 eV are developed and characterized. Excellent agreement between reflectivity simulations and experiments is based on the highly stable ion beam sputter deposition technique. It allows for atomically smooth deposition and the realization of aperiodic multilayer structures with high precision and reproducibility. XUV reflectivity simulation of lanthanum containing multilayer coatings are based on an improved measured set of optical constants, introduced in this thesis.

This work enabled the generation of the shortest ever measured isolated light pulses so far, the creation of the first isolated attosecond pulses above 100 eV, the first demonstration of absolute control of the "attochirp" by means of multilayer mirrors and the formation of spectrally cleaned attosecond pulses, in a spectral region which lacks appropriate filter materials, for a never before achieved combination of spectral and temporal resolution at 125 eV.

Here presented concepts are in principle not restricted to specific energies or experimental set-ups and may be extended in the near future to enter completely new regimes of ultrashort physics.

Zusammenfassung

In den letzten Jahrzehnten hat sich die "Attosekundenphysik" zu einem weit verbreiteten und stetig wachsenden Forschungsfeld entwickelt. Sie ermöglicht sowohl die Untersuchung, als auch die Kontrolle der Dynamik von Elektronen aus inneren und äusseren Schalen mit vorher nie erreichter Präzession. Durch die Erzeugung hoher harmonischer XUV Strahlung in Gasen in Kombination mit optimierten XUV Optiken können *isolierte* Pulse erzeugt werden und Absolutzeitmessungen werden möglich. Bis vor kurzem war die Erzeugung isolierter Attosekundenpulse auf den Spektralbereich unterhalb von 100 eV begrenzt. Das lag vor allem an der Verfügbarkeit von geeigneten XUV Quellen und Optiken. Die spektralen Eigenschaften von XUV Multilagenspiegeln sind in einem weiten Bereich einstellbar, weshalb sie seit jeher Schlüsselkomponenten in der Attosekundenphysik sind.

Die vorliegende Arbeit widmet sich dem Design, der Herstellung und der Messung von periodischen und aperodischen Multilagenspiegeln, sowie deren Applikation in der Generierung und Optimierung isolierter Attosekundenpulse. Zwei- und Drei-Material-Stapel bestehend aus den Materialien Molybdän, Silizium, Borcarbid, Lanthan und Scandium werden vorgestellt und deren Eignung für eine komplette Abdeckung des Energiebereichs zwischen 30 und 200 eV wird untersucht und experimentell bestätigt. Die nahezu perfekte Umsetzung von Spiegeldesigns in reale Optiken zeigt sich in der hohen Übereinstimmung von gerechneten Modellen und Reflektivitätsmessungen und basiert auf der hohen Stabilität des Ionenstrahlsputterns. Diese Technik ermöglicht die Deposition nahezu atomar korrekter Schichten und damit die Herstellung selbst aperiodischer Strukturen mit hoher Genauigkeit und Reproduzierbarkeit. Hier gezeigte gerechnete XUV Reflektivität von Lanthan basierten Multilagenspiegeln, beruht auf neuen, hier vorgestellten, spektral hochaufgelösten Messungen des Brechungindexes von Lanthan im XUV und nahem Röntgenbereich.

Die vorliegende Arbeit ermöglichte die Erzeugung der kürzesten, isolierten je gemessenen Lichtblitze, die erstmalige Generierung von isolierten Attosekundenpulsen mit Zentralenergien oberhalb von 100 eV, die erstmalige quantitative Kontrolle des "Attochirps" von isolierten Pulsen mit Hilfe von Multilagenspiegeln, sowie die Erzeugung spektral gereinigter Attosekundenpulse. Letzteres Konzept ermöglichte erstmalig Einzel-Attosekundenexperimente mit hoher spektraler und zeitlicher Auflösung in Energiebereichen ohne verfügbare XUV Filter.

Die hier präsentierten Konzepte sind prinzipiell auch für andere Energiebereiche und Experimentaufbauten adaptierbar und werden in naher Zukunft dazu beitragen, in völlig neue Regime der Ultrakurzpulsphysik vorzudringen.

Contents

Chapter 1

Introduction: Extreme Ultraviolet- the spectral range of attosecond physics

Pump-probe experiments with isolated attosecond ($1\ as = 10^{-18}\ s$) pulses allow for the direct investigation of the timing of electronic motion and the relative delay between certain electronic transitions with never before achieved temporal precision [1], [2]. Such experiments test current theoretical models and may force a review of the theory of such basic electronic processes as photo-ionization [3], [4], charge transport [5], charge screening, Auger decay [6] or nano-plasmonic oscillations [7]. This paves the way towards a far deeper understanding and finally the control of such transitions.

The time scale of a certain process is inevitably connected to its transition energy as e.g. indicated by Fermi's golden rule. This fundamental law reveals that the transition time $\tau_{i \to f}$ of an electron moving from an initial state i to the final state f scales inversely with the squared energy separation $|V_{fi}|$ of the two states as well as the density of states $\rho(E_f)$ [8], [9].

$$\frac{1}{\tau_{i \to f}} \propto \rho(E_f)|V_{fi}|^2 \tag{1.1}$$

This interrelation of time and transition energy becomes more obvious when one calculates the dipole oscillation period $\frac{1}{T_{osc}} = 2\pi\hbar|V_{fi}|$ of the quantum mechanical wave-packet, which is formed by a superposition of the initial and the final state [2]. Obviously, this

oscillation period is a measure for the time scale on which a certain process happens.
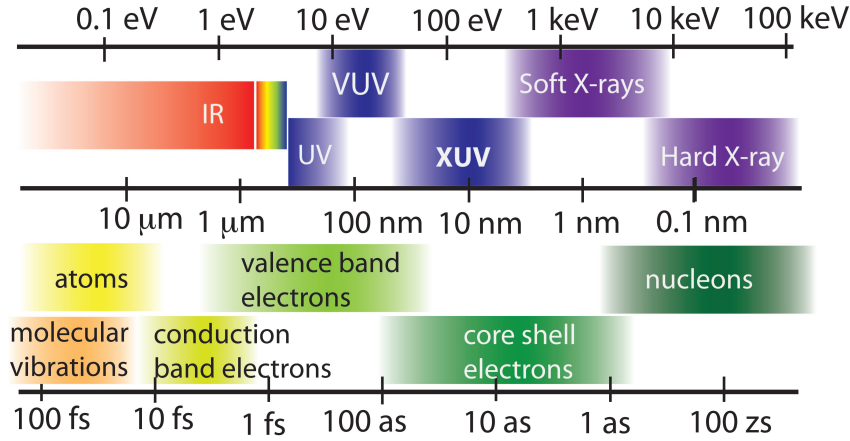
Figure 1.1: Correlation of transition energy and transition times: Upper row: Spectrum (taken from [10]); the XUV range is commonly defined between $\approx 30\ eV$ and the $C\ K1s$ line at $284.2\ eV$ ($4.4nm$). Lower row: Characteristic time scales (given by the dipole oscillation period) connected to the energy level spacing of transition intervals together with selected fundamental processes (taken from [2])

Figure 1.1 displays the transition energies and the oscillation period exemplarily for selected physical processes. Atoms and molecular motion last a few hundred fs to even ps. Outer shell electron transitions (typically in the meV to 10 eV energy range) happen on time-scales of fs to ps and can e.g. in the case of Rydberg atoms with electrons in very high states reach even μs. Also chemical reactions -as follow up events on valence electron transitions- usually happen within a few fs to ps. In contrast inner shell electrons are strongly bound within atoms with typical binding and transition energies in the spectral range of the extreme ultraviolet (XUV, also EUV) and soft to hard X-rays. Those happen therefore on time-scales of a few fs and even sub-fs;

Thus, to gain insight into the dynamics of electronic motion in atoms, molecules or surfaces attosecond XUV pulses are required. Further, every attosecond pump-probe spectroscopy experiment requires its taylor-made pulse synchronized in its certain central energy and dispersion and with a spectral or temporal resolution

appropriate to investigate the process of interest.

The limited tunability of sources and the experimental need for focused and directionally guided attosecond pulses asks for sophisticated attosecond optics. Multilayer-coated XUV mirrors [11], [12], [13] are key components in attosecond metrology and served attosecond experiments from the very beginning [14], [15], [16], [17]. As will be confirmed in this thesis, such optics enable not only attosecond metrology by reflecting, focusing and filtering single attosecond pulses from coherent high harmonic radiation; they further stand out due to their high degree of freedom in shaping both the spectral and the temporal structure of an attosecond pulse by design-optimized aperiodic coatings.

About ten years ago, the first isolated attosecond pulses (≈ 650 as long) could be characterized. These were generated by high harmonic generation in noble gas reaching the XUV and soft X-ray regime [15], [18]. Since then -as demonstrated in the following- further development of sources and appropriate XUV optics enabled to improve this technique for the stable generation of taylor-made isolated attosecond pulses down to pulse lengths of less than 100 as [19].

In contrast to the development of chirped dielectric mirrors in the visible, the realization of aperiodic XUV multilayer mirrors requires new approaches in computational design, manufacturing and characterization, which have not been available and combined until now.

Chapter 2

Background on attosecond pulse shaping

The ultimate goal is the design of optics for the absolute control over all relevant attosecond pulse parameters. These are namely the central energy, the spectral shape, the spectral and temporal phase and the pulse duration. For the best compromise between these, detailed knowledge about how the spectral and temporal properties of a pulse are connected is required; most importantly how the spectral bandwidth and the spectral phase influence the pulse length (section 2.1). In section 2.2 properties of the XUV spectral range in which all presented attosecond experiments take place are summarized; different attosecond XUV optics are analyzed according to their applicability in attosecond physics. The focus lies here on reflective multilayer coatings as introduced in section 2.2.4 as XUV optics with the highest tunability. Finally, in section 2.3 the principle of single attosecond pulse generation, their measurement via electron streaking and the experimental set-up, which is used for the following experiments is explained.

2.1 Influence of spectrum and phase on the pulse length

For the development of pulse shaping optics the quantitative relation between the spectral and the temporal pulse shape is required.

Qualitatively their connection is obvious and can be explained both in the temporal and in the spectral domain:

- In the *time domain,* the electric field of a pulse has to undergo at least one complete field oscillation. One complete oscillation of visible light lasts more than 2 fs and thus hinders the generation of much shorter pulses. The generation of only $\tau = 100 \ as$ long pulses on the other hand requires a central wavelength of less than $\lambda = c/\tau = 30 \ nm$ (40 eV). Generating a pulse of the same length at higher energies relaxes the constraints as more field oscillations are allowed.

- Looking on a pulse in the *spectral domain* its minimum pulse length is given by the number of constructively interfering spectral modes, thus by its spectral bandwidth. As will be shown, a Gaussian pulse of 100 as ($FWHM$) requires a spectral bandwidth of at least 18 eV . Its central energy must be on the same order. The higher the central energy, the less relative bandwidth $\Delta E/E$ is required.

The mathematical formulation of this time-frequency analogy is the Fourier transform. The one dimensional electric field of (coherent) light can be written as a product of the amplitude E_ω (E_t) and a phase factor $\phi_\omega = \phi_\omega(\omega)$ ($\phi_t = \phi_t(t)$) both in the spectral (ω) and in the temporal (t) domain:

$$E(\omega) = E_\omega e^{i\phi_\omega} \qquad resp. \qquad E(t) = E_t e^{i\phi_t} \qquad (2.1)$$

One can convert one representation into the other by the following transform

$$E(t) = \mathscr{F}(E(\omega)) = \frac{1}{\sqrt{2\pi}} \int_{-\infty}^{\infty} E(\omega) e^{-i\omega t} d\omega \qquad (2.2)$$

with the coefficients

$$E(\omega) = \mathscr{F}^{-1}(E(t)) = \frac{1}{\sqrt{2\pi}} \int_{-\infty}^{\infty} E(t) e^{i\omega t} dt. \qquad (2.3)$$

In the following, upper equations are applied to Gaussian pulses. Their temporal length is quantitatively related to their spectral bandwidth (section 2.1.1) and phase (section 2.1.2) as prerequisite for the design of pulse-shaping optics.

2.1.1 Time-bandwidth relation

Calculating the Fourier transform of arbitrary fields may be lengthy and is usually performed numerically. For selected cases as Gaussian pulses an analytical solution is rather easy. As deduced in appendix A, the electric field $E(t)$ of a Gaussian pulse in its (temporal) $FWHM$ representation takes on the form [20]:

$$E(t) = E_t e^{-2ln(2)\frac{t^2}{\tau_0^2}} e^{-i\omega_0 t} e^{-i\phi(t)} \qquad (2.4)$$

Here E_t is an amplitude factor, $\hbar\omega_0$ is the central energy of the pulse, $\phi(t)$ is an additional time dependent phase and τ_0 is the minimum $FWHM$ pulse length in the case that $\phi(t)$ is linear, as explained in more detail in the following.

In the case of a *vanishing phase term* $\phi(t) = 0$ it is easy to apply the Fourier transform (eq. 2.3) for the corresponding frequency domain representation. As deduced in appendix A the spectral shape of a Gaussian pulse is again Gaussian.

$$E(\omega) = E_\omega e^{-2ln(2)\frac{(\omega-\omega_0)^2}{\Delta\omega_0^2}} \qquad (2.5)$$

$E_\omega = \sqrt{\frac{\tau_0^2}{4ln2}} E_\tau$ is the amplitude factor. $\Delta\omega$ is the spectral bandwidth ($FWHM$) of the Gaussian. $\Delta\omega$ can be directly related to τ_0 from Fourier-transform analyses performed in appendix A (equation A.7):

$$\Delta\omega\tau_0 = 4ln(2) \approx 2.77 \qquad (2.6)$$

An equivalent handy formulation is:

$$\Delta E[eV]\tau_0[as] \approx 1824 \qquad (2.7)$$

One finds that the spectral and the temporal $FWHM$ of a pulse are inversely proportional to each other. This time bandwidth relation is plotted in figure 2.1.

As vanishing additional phase terms ϕ_t have been assumed the plotted pulse length is the lower limit for a given Gaussian spectrum. Pulses which fulfill this relation are usually referred to as
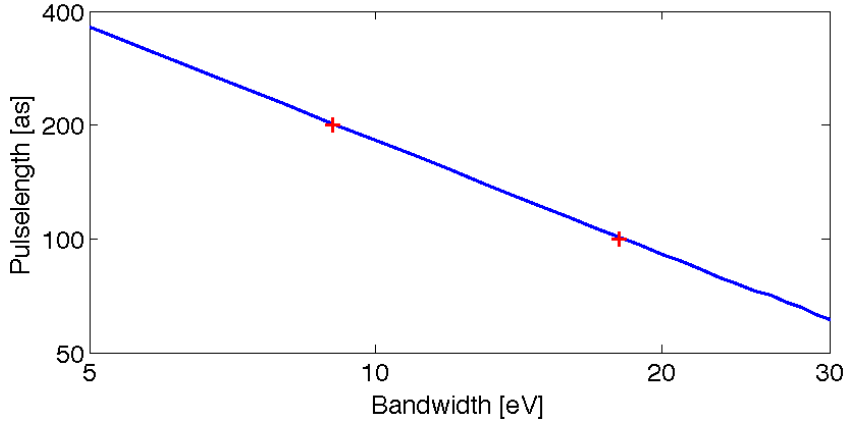
Figure 2.1: Fourier limited pulse length of a Gaussian pulse in dependence on its spectral bandwidth (double-logarithmic scale). Both the 100 as (18 eV bandwidth) and the 200 as (9 eV bandwidth) cases are highlighted.

"bandwidth- limited" or "Fourier-limited". As highlighted in figure 2.1 at least 18 eV (9 eV) bandwidth is required for a 100 as (200 as) long pulse.

Equation 2.7 is closely related to the uncertainty principle [21] and holds true also for non-Gaussian pulse shapes, but occurs with a slightly different constants on the right hand side of the equation, depending in the pulse shape.

2.1.2   Dependence of the pulse length on the spectral phase

Neglecting the temporal phase term ϕ_t in the last subsection yielded a Gaussian pulse in the spectral domain (equation 2.5) with vanishing additional spectral phase-terms ϕ_ω (see e.g. equation 2.1). Here now the spectral to temporal transform is performed to investigate the effect of the spectral phase ϕ_ω on the pulse length. Assuming again a Gaussian test pulse with a Gaussian spectrum

$$E(\omega) = \underbrace{E_\omega e^{-2ln(2)\frac{(\omega-\omega_0)^2}{\Delta\omega_0^2}}}_{G_\omega} e^{i\phi_\omega} = G_\omega e^{i\phi_\omega} \tag{2.8}$$

one can develop the spectral phase $\phi_\omega = \phi_\omega(\omega)$ in terms of a Taylor series around the central energy ω_0 [22].

$$\phi_\omega = \phi_0 - GD(\omega_0)\cdot(\omega - \omega_0) - \frac{1}{2}GDD(\omega_0)\cdot(\omega - \omega_0)^2 +$$

$$+ \frac{1}{6}TOD(\omega_0)\cdot(\omega - \omega_0)^3 + \dots \qquad (2.9)$$

Please find the definition of the used abbreviations below.

2.1.2.1 The carrier-envelope offset ϕ_0

The first term ϕ_0 adds a constant offset to the spectral phase. In the
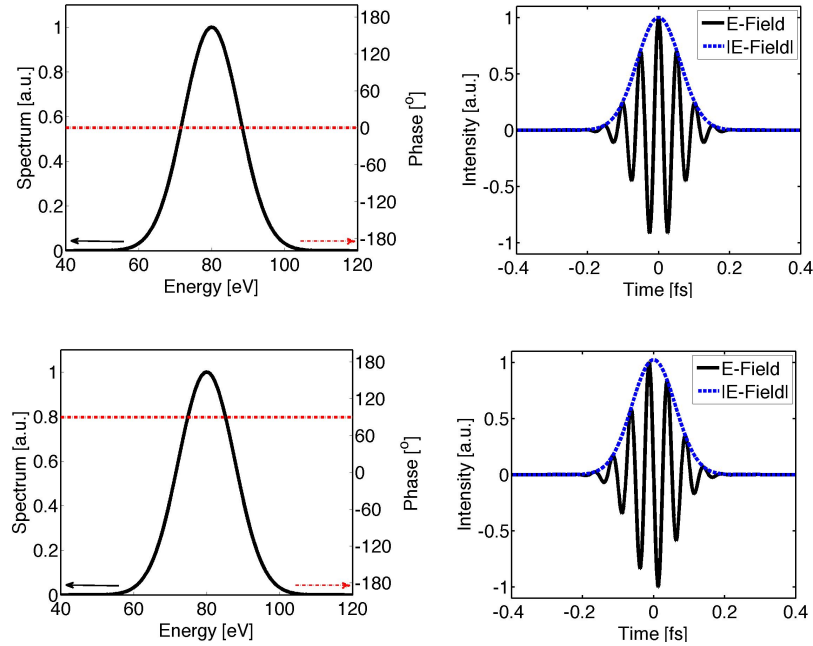
Figure 2.2: Simulation of two pulses, differing from each other by their phase offset ϕ_0 (Upper row: $\phi_0 = 0°$, lower row: $\phi_0 = 90°$). The left column shows the spectral intensity (black line) and the spectral phase (red dashed line), compared to the field (black line) and the field envelope (blue dashed line) in the temporal domain plotted in the right column. All fields and intensities have been normalized. The unperturbed pulse is a 100 as long Gaussian (thus, it has a bandwidth of 18eV), centered at 80 eV. Due to ϕ_0 the CEP changes from *cosine* to (-) *sine*.

temporal domain this yields a shift in the carrier-envelope phase

(CEP). The CEP is defined by the relative position of the electric field under the pulse envelope. If the maxima of the pulse envelope coincides with a maximum of the field (e.g. figure 2.2 panel b)) one inspects a *cosine* CEP, while the CEP is called *sine* like if the electric field vanishes at the envelope maximum. Figure 2.2 illustrates that exemplarily for an additional spectral phase term of 90°. Temporally the CEP is shifted from cosine (left panel) to (-) sine (right panel).

While the generation of high harmonic radiation from ultra-short IR/VIS laser pulses is largely influenced by the CEP of the driving pulse (e.g. section 2.3), it can be neglected when shaping the attosecond pulse length, as this term does not influence the intensity shape and thus the pulse length.

2.1.2.2 Group delay

The second term is the *group delay* and is inversely proportional to the group velocity v_g:

$$GD = -\frac{d\phi}{d\omega} = -\frac{L dk}{d\omega} \propto \frac{1}{v_g} \qquad (2.10)$$

Please note that throughout this thesis, the GD is defined as the *negative* derivative of the phase to match the sign of the GDD in the next subsection 2.1.2.3. The GD corresponds to a spectral phase term which is linear in energy. As a result there is a point in space, where all relative phase relations are identical to the case of $GD = 0$ at point zero. In the time domain this corresponds to a shift of the pulse envelope by $\Delta t = GD$ as plotted exemplarily in figure 2.3 for a pulse with a GD of $-200\ as$.

Please note that the pulse envelope is shifted in time by the GD, while the phase offset ϕ_0 remains unperturbed and thus the resultant pulse also has a different CEP.

The GD again does not affect the pulse length, so it can be as well ignored when designing optical elements for attosecond pulse shaping. Experimentally a different position of the optics, thus a different path length could compensate for the delay.
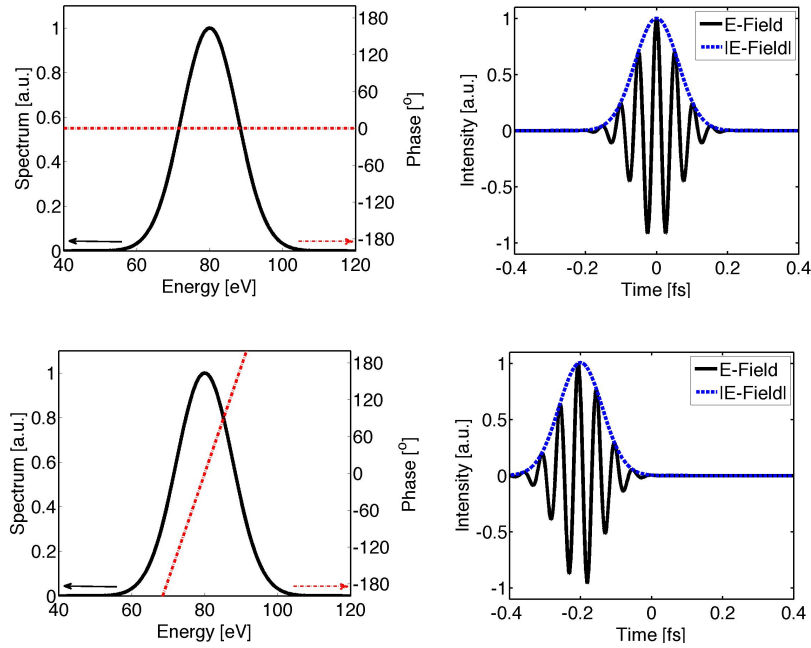
Figure 2.3: Effect of a group delay of $GD = -200 as$ (lower row) on the temporal electric field of a test pulse with $GD = 0\ as$ (upper row). For details on the plots and the test pulse characteristics, see caption figure 2.2.

2.1.2.3 Group delay dispersion

The $GDD = \phi'' = \frac{d\,GD}{d\omega} = -\frac{d^2\phi}{d\omega^2}$ is the lowest order phase term that temporally broadens a pulse as explained in the following. The GDD term yields an energy dependent group delay:

$$\phi'' = -\frac{d}{d\omega}\frac{d\phi}{d\omega} = -\frac{d}{d\omega}\frac{1}{v_g} \tag{2.11}$$

Differently spoken, due to GDD different frequencies are shifted differently far in time, thereby all frequencies are temporally lined up and the pulse gets "chirped". By definition, a negative GDD yields a negative chirp in time, meaning long wavelength components ("red") are trailing short ones ("blue") and vice versa [23] for the case of positive chirp.

Figure 2.4 shows this exemplarily for the case of $\phi'' = 4000\ as^2$. The pulse is being stretched from 100 to 150 as and the wave oscillation period decreases with time.
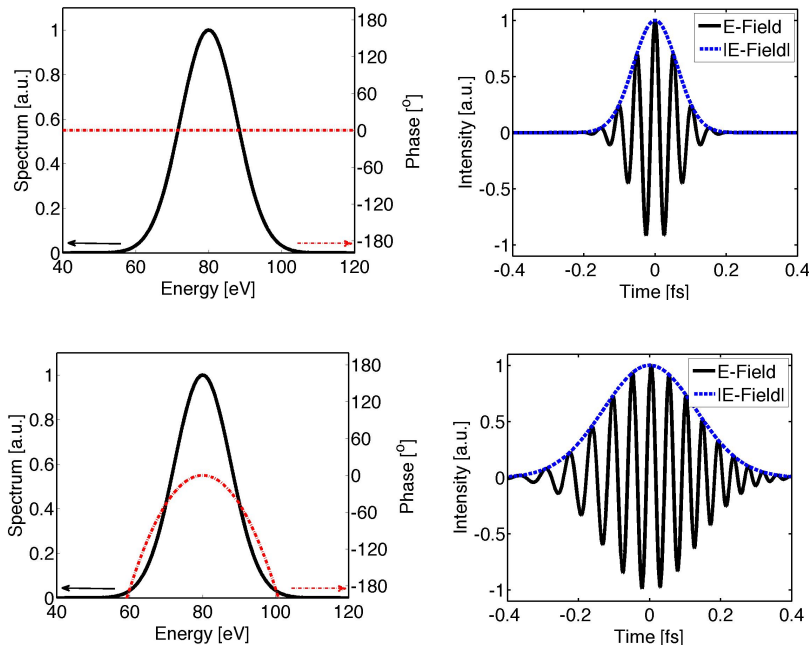
Figure 2.4: Chirping and broadening (lower row) an originally 100 as long test pulse (upper row) as a consequence of $GDD = 4000 as^2$. For plot details and the test pulse parameters please read caption of figure 2.2.

(a) GDD dependence   (b) TOD dependence
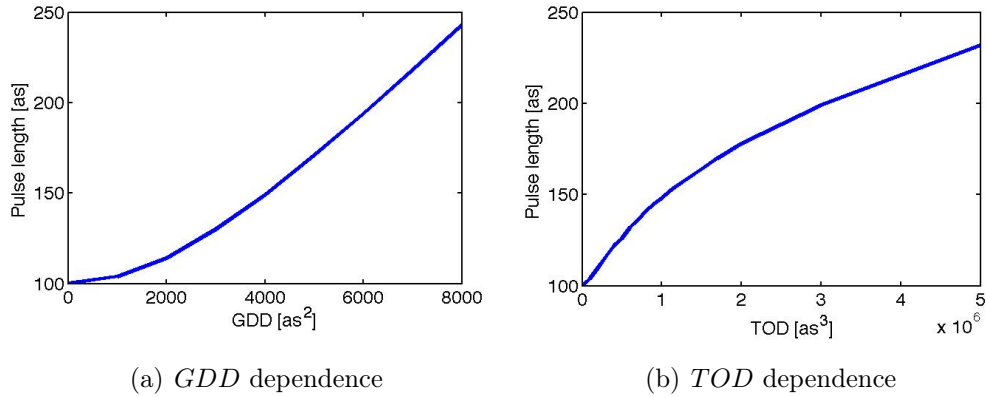
Figure 2.5: Simulated pulse length of a Fourier limited 100 as test pulse centred at 80 eV in dependence on constant GDD (panel a)) and TOD (panel b)).

As deduced in the appendix A, one can even retrieve an analytical relation for the pulse length $\tilde{\tau}$ of a Gaussian pulse depending

on its GDD ϕ'' and its Fourier limited pulse length τ_0:

$$\tilde{\tau} = \tau_0 \sqrt{1 + \frac{16(ln2)^2\phi''^2}{\tau_0^4}} \qquad (2.12)$$

Please note that this broadening is independent of the central energy ω_0. In terms of intensity this broadening appears to be symmetric. Relation 2.12 is plotted figure 2.5 a).

2.1.2.4   Third and higher order dispersion

The TOD is the third order dispersion term:

$$TOD = \frac{d^3\phi}{d\omega^3} \qquad (2.13)$$
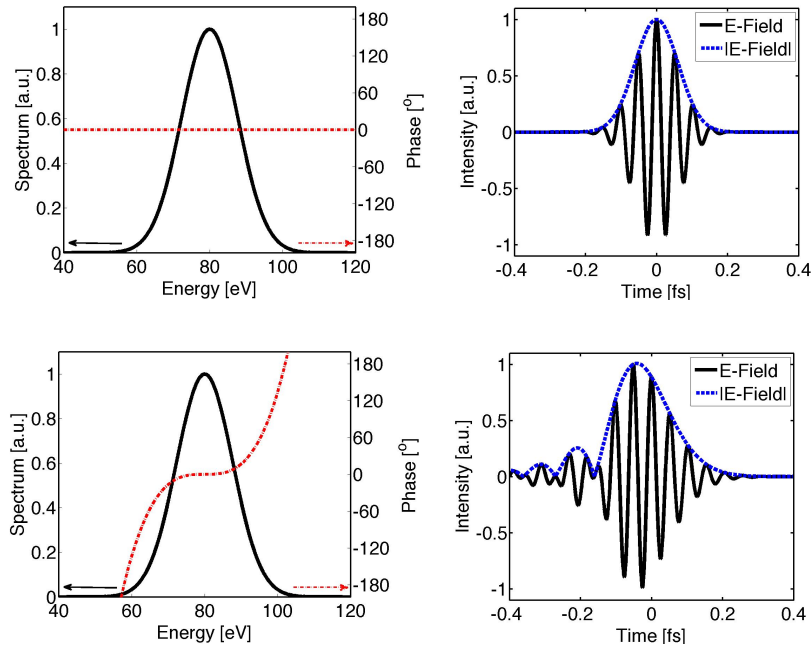
Figure 2.6: Asymmetrical broadening of a 100 as long test pulse due to a TOD of 40000 as^2. Please read caption of figure 2.2 for details on the plots and the test pulse characteristics.

Third and higher order phase terms also broaden the pulse. Compared to the GDD, their effect on the pulse length is usually less severe although not at all negligible. As plotted in figure

2.6 exemplarily for a Gaussian pulse with a Fourier limited pulse length of 100 as and an additional TOD of 40000 as^3, third and higher order phase terms manifest themselves in an asymmetric pulse broadening. The right panel of figure 2.5 displays the pulse length of a 100 as long Fourier limited Gaussian centred at 80 eV in dependence on the TOD amount.

2.1.3 GDD-noise

Beside constant phase terms, also the influence of "noisy GDD" on the pulse length has to be investigated when designing multilayer mirrors. This is being analyzed in the following.

Especially GDD-optimized aperiodic multilayer mirrors may suffer from GDD fluctuations around a mean value - mostly as a consequence of a discrete number of interfaces in a multilayer mirror or from discontinuities in the optical constants. Each mirror design is a trade-off between different target functions and the question arises, to which extend these fluctuations affect the final pulse length or to which extend these are acceptable in the designs.

I use an analytical approach to tackle this problem in the following, starting from the analytical description of the GDD dependent pulse length given by equation 2.12. In the following the GDD (ϕ'') is assumed to consist of a constant GDD term ϕ_0'' and an additional term $\Delta\phi''$, which accounts for fluctuations. Latter is assumed to result in normally distributed GDD around ϕ_0'' with a standard deviation σ:

$$\phi'' = \phi_0'' + \Delta\phi'' \tag{2.14}$$

One can calculate the expectation value $\mathscr{E}(\tau)$ for the pulse length as a function of the noise amplitude σ:

$$\mathscr{E}(\tau) = \tau_0 \mathscr{E}(\sqrt{1 + \frac{\alpha(\phi_0'' + \Delta\phi'')^2}{\tau_0^4}}) =$$

$$= \frac{\tau_0}{\sigma\sqrt{2\pi}} \int_{-\infty}^{\infty} dx \sqrt{1 + \frac{\alpha(\phi_0'' + x)^2}{\tau_0^4}} e^{-\frac{-x^2}{2\sigma^2}} \tag{2.15}$$
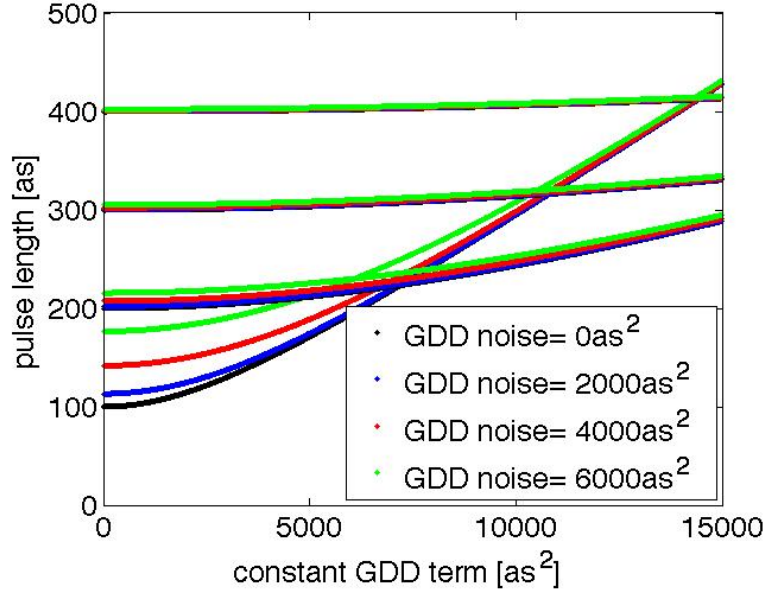
Figure 2.7: Simulated pulse length in dependence on a constant GDD term (horizontal axis) and additional normally distributed GDD for four different pulses with Fourier limited pulse lengths of $\tau \varepsilon [100\ as,\ 200as,\ 300\ as,\ 400\ as]$ (vertical bunches). Each color represents a certain noise amplitude.

with $\alpha = (4ln2)^2$ and $x = \Delta\phi''$.

The resultant pulse length is plotted in figure 2.7 as an outcome of a numeric calculation of relation 2.15[1]. One finds that both the constant GDD term and the GDD noise yield a longer pulse.

The validity of this approach can be confirmed by Fourier transform calculations of an $18\ eV$ broad Gaussian pulse where a periodic fluctuating GDD has been assumed.

$$\Delta\phi'' = Acos(\omega T_{osc}) \qquad resp. \qquad \Delta\phi'' = Asin(\omega T_{osc}) \qquad (2.16)$$

Figure 2.8 displays exemplarily the broadening of a $100\ as$ Fourier limited Gaussian (thus $18\ eV$ bandwidth) calculated depending on the oscillation period $2\pi/T_{osc}$ in $[eV]$. An oscillation amplitude $A = 10000\ as^2$ has been chosen exemplarily in this calculation, corresponding to an rms standard deviation of $\sigma \approx 7000\ as^2$. The

---

[1]For simple cases, as when $\phi_0'' = 0$ and the phase noise is small, an analytic solution can be retrieved as presented in appendix B.
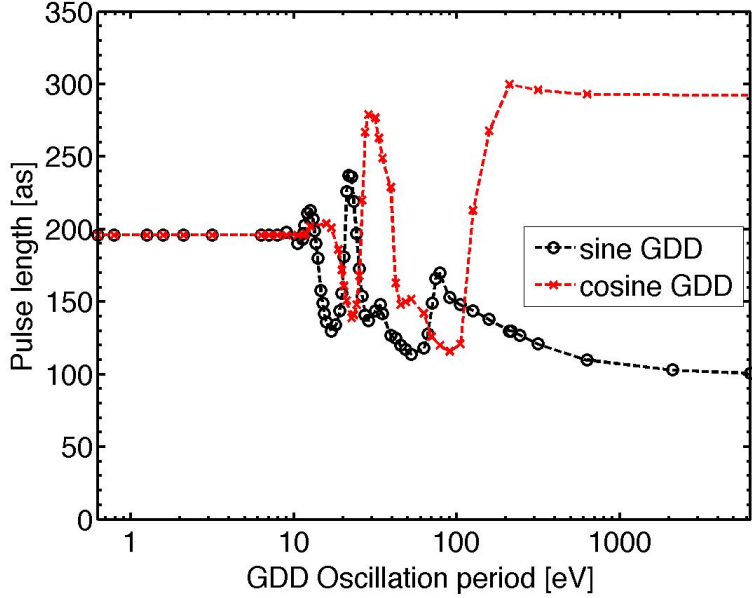
Figure 2.8: Pulse broadening of a Fourier limited $\tau_0 =100 \ as$ long test pulse as a consequence of periodic sinusoidal (black curve) and cosine-shaped (red graph) GDD oscillations. For more detailed information, please see text.

red dots in figure 2.8 assume a cosine-shaped GDD, the black symbols show the case with sine-shaped GDD.

Let us now analyze the results more quantitatively:
For very large oscillation periods, the GDD curves flatten out, thus the sine GDD converges to zero ($\tau \rightarrow 100 \ as$), while the cosine GDD converges to a constant GDD offset of $10000 \ as^2$ ($\tau \rightarrow 290 \ as$) as expected from calculations plotted in figure 2.5 a). Contrary to that, for small enough oscillation periods ($T < 2/3 \ \tau_0$) the pulse length converges to a value of $196 \ as$ for both a cosine-like and a sinusoidal GDD. This is in agreement with the outcome of the analytical model depicted in figure 2.7.

Summarizing, both the constant and the noisy GDD affect the pulse length in a very similar quantitative manner. While a constant GDD of e.g. $\phi_0'' =7000 \ as^2$ broadens a Fourier limited 100 as long pulse to nearly 220 as in time, normally distributed GDD around $\phi_0'' = 0$ and a standard deviation $\sigma =7000 \ as^2$ broadens the same pulse to about 190 as.

In reality there is a big difference between the two kinds of GDD terms. While it is possible to compensate constant GDD offsets by additional optics with opposite behavior, GDD fluctuations are not compensable.

2.1.4   Requirements on attosecond pulse shaping optics

Each individual attosecond experiment, requires its perfectly synchronized pulse. As a result from the previous sections the most important pulse requirements can be summarized as follows:

1. The **carrier wavelength** of a pulse needs to be synchronized with experimental spectral requirements. This is especially important in resonance measurements. But it might as well be a key issue in pump-probe experiments, where the kinetic energy of photoelectrons is used as signal; this is the case in almost all attosecond pulse measurement techniques (section 2.3). The photoelectron signal of interest may be superimposed by other electron sorts as e.g. by Auger electron lines occurring at distinct energies. Further, a coexistent IR/VIS laser pulse on the target (as present in the attosecond streak camera set-up (section 2.3.3.1)) additionally generates free electrons by multi-photon above threshold ionization (ATI) at low XUV energies, typically up to 30-40 eV. Choosing a higher central energy far off Auger lines, may yield a cleaner photoelectron signal of interest. Additionally a higher central energy relaxes the conditions for shorter pulses, as the required relative bandwidth is smaller. Beside all that, some applications require certain additional optics as thin metal filters. Their transmission opening energies are related to atomic absorption edges thus their availability is limited. For spectrally clean pulses one may also choose the central energy according to these.

2. The **spectral shape** of a pulse defines both the spectral resolution, but also the shortest possible pulse length τ_0. As we have seen, a high spectral resolution (thus a small bandwidth

ΔE) contradicts a high temporal resolution due to the time-bandwidth relation 2.7. Therefore one has to find a trade-off between those. In addition to that, spectrally and temporally clean pulses are of interest. Side structures of the pulse both in the spectral and temporal domain complicate a correct retrieval and therefore spectral cleaning by specially designed optics might be necessary.

3. The **spectral phase** ϕ_ω is extremely important as has been proven in section 2.1.2. In most experiments a flat pulse phase is desirable, yielding the Fourier-limited pulse length. When it comes to 2-photon XUV experiments, chirped pulses may allow for coherent control of photo excitation [24] or yield experiments with even higher temporal resolution as the distinct energies are lined up in a chirped pulse.

4. Last but not least, a **large photon number** (typically $> 10^7$ photons per second in attosecond experiments) is required for many experiments.

The limited tunability of coherent XUV sources asks for additional pulse-shaping optics to fulfill upper requirements. Table 2.1 comprehends those.

2.2   Extreme ultraviolet attosecond optics

The spectral range of Extreme UltraViolet (XUV, also EUV[2]) is commonly defined between about 30 eV (≈ 40 nm) and the CK edge at 284.2 eV (4.4 nm) as indicated figure 1.1 [26], [10]. It stands out due to the fact that all elements have inner shell absorption edges. This allows for a large variety of material selective spectroscopy experiments. Furthermore, the intrinsically short wavelength-nature of XUV radiation enables not only the generation of shorter pulses. It allows one to resolve and write

---

[2]While the "attosecond community" prefers XUV as a technical term, the term EUV is common in microscopy, lithography. Throughout this thesis "XUV" is used, but technical terms in specific applications as "EUV lithography" are employed.

Table 2.1: Requirements on attosecond optics

1	**Spectral selective optics** synchronized in **central energy** E_0 both with the available source and the experimental constraints are required.
2	The **bandwidth** of an attosecond optic must be **optimized** for the experimental needs and has to be chosen as a trade-off between spectral and temporal resolution. A distinct spectral shape as a **high signal to noise ratio** between certain spectral ranges is desirable.
3	Optics should be able to **compensate** or **introduce distinct amount of** GDD for adjustment of the pulse length and the chirp.
4	**Not angular disperse** optics are needed as these would lengthen the pulse. Therefore gratings [25] or zone-plates are to avoid.
5	**High throughput** optics are desirable as the photon flux often limits the functioning of a distinct experiment. Beside that, distinct optics allow for lateral shaping. E.g. focusing of a beam may enable an enhanced photon flux on the target.

much smaller structures[3] compared to visible light, as being utilized both in EUV microscopy [27], [28] and EUV lithography [29]. XUV experiments could thus in principle wed the high spectral, spatial and temporal resolution as e.g. proposed by Stockman et al. [7].

The high absorption of all materials on the other hand sets high constraints on the experimental conditions, especially the sources and the optics as all XUV experiments must therefore be fully contained in vacuum. That is one major reason why these became available not before the 1960s.

---

[3]typical sizes of a few nm

2.2.1 XUV optical constants

The interaction of XUV light with matter is dominated by (core-)electron-photon interactions. The macroscopic material specific interaction characteristics are described by the optical constants $\tilde{n}$. Throughout this thesis, the common definition of XUV optical constants is being used [10]:

$$\tilde{n} = 1 - \delta + i\beta \tag{2.17}$$

The macroscopic parameter $\tilde{n}$ can be directly related to the microscopic complex atomic scattering factor $f^0 = f_1^0 + if_2^0$ [10]:

$$\tilde{n}(\lambda) = 1 - \delta(\lambda) + i\beta(\lambda) = 1 - \frac{n_a r_e \lambda^2}{2\pi}(f_1 - if_2) \tag{2.18}$$

n_a is the density of electrons per unit volume, $r_e = \frac{e^2}{4\pi\varepsilon_0 m_e c^2}$ is the classical electron radius and λ is the vacuum wavelength of light. The atomic scattering factors describe light-matter interaction in multi-electron systems and can in some cases be even calculated in reasonable agreement with measurements by damped harmonic oscillator models.

The role of both the real part ($n = 1 - \delta$) and the imaginary part β of the index of refraction is easy to understand when analyzing a plane wave with energy $\hbar\omega$ and wave-vector $\vec{k}$ propagating in z-direction within a material which is characterized by its index of refraction $\tilde{n}$. The electric field of this wave at a point z can be written as:

$$E = E_0 e^{i(k_z z - \omega t)} = E_0 e^{i(\frac{2\pi}{\lambda}\tilde{n}z - \omega t)} = E_0 e^{\underbrace{i\omega(\frac{z}{c}-t)}_{(a)}\underbrace{-i\frac{2\pi\delta}{\lambda}z}_{(b)}\underbrace{-\frac{2\pi\beta}{\lambda}z}_{(c)}} \tag{2.19}$$

Here the proportionality of the absolute value of the wave-vector k_z and the index of refraction $\tilde{n}$ has been used:

$$k_z = |\vec{k}| = \frac{2\pi}{\lambda}\tilde{n} \tag{2.20}$$

The first phase term (a) in the exponent of equation 2.19 describes a plain wave propagating through vacuum. The second term (b)

contributes an additional phase shift proportional to δ due to the different optical density of the propagation medium. The last term (c) accounts for absorption within the medium. β can be directly related to the absorption coefficient α by squaring equation 2.19 [10]:

$$I = I_0 e^{-\alpha z} \qquad or \qquad \alpha = \frac{4\pi\beta}{\lambda} \qquad (2.21)$$

Equation 2.18 predicts that the real part of the XUV optical constants are typically smaller than 1 in contrast to the visible. The absolute values of δ and β decrease for higher energies ($\beta, \delta \propto \lambda^2 f^0 \propto f^0/\omega^2$) and thus $\tilde{n}$ of all materials assimilate and approaches unity. δ and β of a distinct material are typically on the same order e.g. typically $\sim 10^{-1} - 10^{-3}$ around 100 eV. Thereby the limited penetration depth of XUV radiation (of typically a few hundred nm) comes along with additionally low diffraction at an interface between two materials due to the similarity of the optical constants. This of course limits the performance of appropriate XUV optics. As we will see, XUV optics must either be very thin, be used in reflection under small grazing incidence angles or make use of the coherent summation of radiation reflected from different interfaces as utilized in multilayer mirrors.

2.2.2 The linearity of XUV optics

The limited number of photons with which XUV experiments are usually performed and the low multi-photon absorption cross section in the XUV are the main reasons, why up to now only linear XUV optical elements exist. Bright sources as the free electron lasers [30] or high intensity high harmonic generation sources [31], [32] allow one to enter the nonlinear regime and two photon ionization has also been used as signal [32]. But still we are far before utilizing these effects for nonlinear XUV optics as commonly used in the visible range.

The mathematical treatment of linear optical elements is rather easy [33], [22], [10]. E.g. a mirror is fully characterized by its spectral reflectivity amplitude $r_\omega(\omega)$ and its spectral phase $\phi_m(\omega)$

dependent on the angle of incidence θ and the polarization $\vec{p}$ of the incoming radiation. The spectral field $E_o(\omega)$ of the outgoing radiation is then given by a simple multiplication of the spectral field amplitude of the incoming light $E_i(\omega)$ (equation 2.1) and the spectral reflectivity of the mirror $r_m(\omega) = r_\omega(\omega)e^{i\phi_m(\omega)}$.

$$E_o(\omega) = E_{o,\omega}e^{i\phi_o} = E_{i,\omega}e^{i\phi_i}r_\omega e^{i\phi_m} = E_{i,\omega}r_\omega e^{i(\phi_i+\phi_m)} \qquad (2.22)$$

Spectral phases are additive.

In ultrafast physics one is interested as well in the temporal description of this interaction. The interaction of light $E_i(t)$ with the time structure of an optical element $r_m(t)$ is given by a convolution:

$$E_o(t) = \mathscr{F}(E_o(\omega)) = \mathscr{F}(E_i(\omega)r_m(\omega)) = \mathscr{F}(\mathscr{F}^{-1}E_i(t)\mathscr{F}^{-1}r_m(t))$$

$$E_o(t) = E_i(t) \otimes r_m(t) \qquad (2.23)$$

Finally one has to square the amplitudes (e.g. reflectivity r, transmission t, field amplitude E, ...) to get the intensity values (R, T, I,...).

$$R = |r|^2; \quad T = |t|^2; \quad I = |E|^2 \qquad (2.24)$$

2.2.3 Single interface reflectance and transmittance

Unlike in the visible range, where e.g. simple Ag-coated mirrors can be used for the broadband and effective ($R(\lambda{>}400\ nm){>}90\%$) guidance of light under nearly arbitrary angles of incidence, no comparable optics are available in the XUV range as will be investigated in the following.

The single interface reflectivity is given by the Fresnel coefficients. In the following the results from retrievals of both Snell's law and the Fresnel coefficients from Maxwell's equations [34] are summarized. The more detailed deduction of these can be found in appendix C. These formulas are prerequisites for the mathematical treatment of multilayer mirrors in the next section.

Figure 2.9 displays the model of two layers with the refractive indexes $\tilde{n}_1$ and $\tilde{n}_2$ forming an interface. Monochromatic light of wavelength λ, incident on the interface under a propagation angle θ_i is assumed. As derived in appendix C claiming continuity
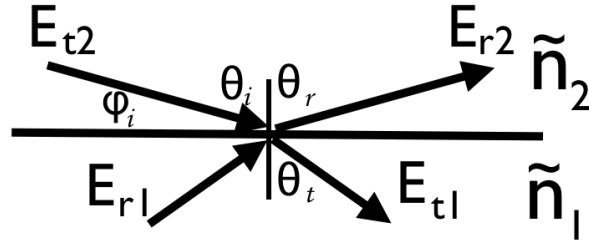
Figure 2.9: Schematic model of an interface between two materials 1 and 2.

of *parallel* electric field components at an interface at any time, directly yields *Snell's law*:

$$\theta_r = \theta_i \qquad \text{and} \qquad \tilde{n}_t sin\theta_t = \tilde{n}_i sin\theta_i \qquad (2.25)$$

The single interface reflectivity on the other hand can be deduced by utilizing continuity relations of the *perpendicular* field components (appendix C).

The resulting equations adopt a slightly different form, depending on the polarization of the incoming light. But one can actually separate each beam of arbitrary polarization into two components: One component, where the electric field vector is parallel to the plane of incidence (*p*-polarization) and one where the electric field vector is perpendicular to the plane of incidence (*s*-polarization) including a phase delay ϕ_{sp} between the two components:

$$\vec{E} = E_s \vec{1}_s + E_p \vec{1}_p e^{i\phi_{sp}} \qquad (2.26)$$

Thereby the reflection of each component can be calculated separately for s and p polarization and can be merged again by a superposition of the two reflected components following equation 2.26.

As deduced in appendix C one finally ends up with the polarization-dependent Fresnel coefficients, which generally describe the transmitted and the reflected field amplitude at an interface between linear, homogeneous, and non-magnetic media.

$$r_{1,2} = \frac{q_1 - q_2}{q_1 + q_2} = -r_{2,1}; \qquad t_{1,2} = \frac{2q_1}{q_1 + q_2} \qquad (2.27)$$

The equations in 2.27 have the same appearance both for s and p polarization; only the coefficients q_1 and q_2 differ. In the case of

s-polarization q_a ($a\varepsilon[1,2]$) is the momentum transfer and twice the perpendicular component of the absolute value of the wave vector $q_a^s = 2k_{a\perp} = \frac{4\pi}{\lambda}\tilde{n}_a cos\theta_a$. The p-polarized notation can be simplified to: $q_a^p = cos\theta_a/\tilde{n}_a$.

(a) s-polarization   (b) p-polarisation
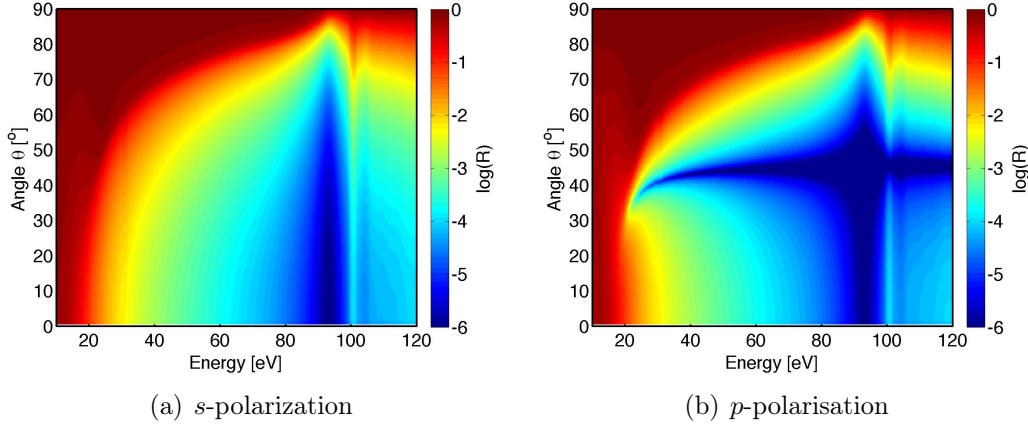
Figure 2.10: Simulated single interface reflectivity of an Si surface at vacuum dependent on both the incidence angle θ and the photon energy.

Figure 2.10 shows exemplarily the outcome of a simulation of a single Si surface for XUV light impinging under vacuum. The reflectivity $R_{1,2} = |r_{1,2}|^2$ is plotted in false color representation against both the angle of incidence θ and of the energy $\hbar\omega$. Each panel shows the result of one polarization.

Summarizing the most important features of this simulation, one finds:

- The single interface reflectivity of both for s and p polarized light drops with increasing energy as the optical constants approach 1.

- Only in the vicinity of an absorption edge (e.g. at 99 eV in the case of Si) where the optical constants exhibit discontinuities, upper tendency is broken and higher single interface reflectivity becomes possible.

- High reflectivity of nearly 100% is found at very small grazing incidence angles and total external reflection occurs if $cos(\theta) < \sqrt{2\delta}$ [33].

- In the case of s polarization, the single interface reflectivity increases with increasing angle.

- In the case of p polarization, the reflectivity drops around $\theta \approx 45^o$ due to Brewster angle reflection. $\theta_B = arctan(\frac{\tilde{n}_2}{\tilde{n}_1}) \approx arctan(1) = 45^o$.

2.2.3.1 Grazing incidence optics

The broadband and high reflectivity of single interfaces at small grazing angles allow one to use bulk reflectors for the guidance of attosecond pulses. The small penetration depth at total external reflection angles ensures a flat phase reflection. For example a gold coated parabola is being used as focusing optic in the attosecond beam-line setup $AS2$ (appendix F, [35]). But beside their high reflectance and broadband beam guidance, these optics exhibit no possibility for as pulse-shaping.

2.2.3.2 Normal incidence

All presented attosecond experiments are performed at $\theta = 5^o$ or 45°, thus far-off grazing incidence angles. In this case, equation 2.27 can be approximated and written depending on the differential of the real ($\Delta\delta = \delta_1 - \delta_2$) and the imaginary ($\Delta\beta = \beta_1 - \beta_2$) parts of the index of refraction [33] of two materials 1 and 2:

$$R_{1,2} = \frac{\Delta\delta^2 + \Delta\beta^2}{4cos^4(\theta_0)} \qquad (2.28)$$

One finds that the single normal interface reflectivity is proportional to the distance of the optical constants in the complex plain (Pythagorean theorem). So both a large separation of the diffraction part δ and in the absorption part β results in higher reflectivity. Please note, that the typical single interface reflectivity is very low ($\approx 1\%$ at $30\ eV$ and $\approx 0.1\%/\ 0.01\%$ at $100\ eV/200\ eV$). XUV optics with a higher reflectivity can be implemented by multilayer interference coatings as introduced in the following section.

2.2.4   Multilayer Mirrors

Multilayer mirrors are stacks of nanolayers of different materials. They are designed to make use to utilize constructive interference of partially reflected waves from the individual interfaces. Multilayer coatings can exhibit high normal incidence XUV reflectivity of up to 70 % in the case of Mo/Si near 95 eV [36]. Their reflectivity characteristics can be designed taylor made by a proper choice of the layer materials and the multilayer stack design. This allows for (spectrally) tuning and filtering extreme ultraviolet radiation with very high precision.

Beside that, multilayer coatings have the great advantage that one can deposit those on arbitrary surfaces. Super-polished substrates, spheres, ellipsoids and parabolas with low figure error can be used for focusing, imaging or beam guidance.

All these advantages decorate multilayer mirrors as key-components for their usage in attosecond physics.

First experimental investigations of multilayer XUV optics started already in the early 1970s [37]. Today, multilayer stacks with complex designs are developed by advanced deposition and design techniques [38], [23], [39] with almost atomically precise interfaces and layer homogeneity [40]. Demanding applications range from EUV lithography [41], [29], soft X-ray microscopy [25], XUV holography and (solar) astronomy [42], [43], XUV polarizers and phase retarders [44] to hard X-ray monochromators [45].

Lately, multilayer mirrors have been introduced in the generation of attosecond pulses to filter particular spectral bands from high-harmonic (HH) radiation and give a handle on shaping both the spectral and the temporal characteristics of attosecond pulses with a high degree of freedom [11], [46], [12], [47], [13].

2.2.4.1   Periodic stacks

One distinguishes periodic and aperiodic stacks. A periodic stack consisting of two different materials in alternating order as schematically plotted in figure 2.11. Periodic stacks are characterized by the following parameters:
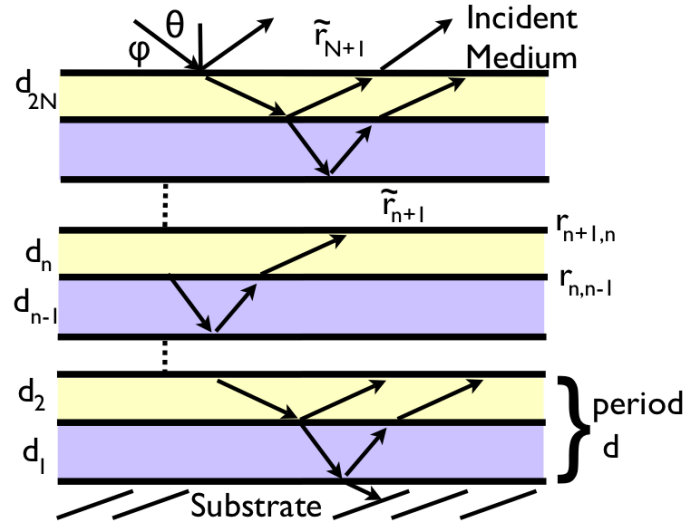
Figure 2.11: Schematic view-graph of a two material multilayer coating.

- The period number N is the number of bi-layers in the case of a two-material stack or of the repeating structures in a ternary, quaternary, ... stack.

- The period (thickness) d.

- The ratio of bottom layer thickness to the period $\gamma = d_{bottom}/d$. In the case of more than two materials per period, one γ_a per material a will be defined throughout this work (section 4.4.1).

- The interface roughness σ, which accounts for the loss of the single interface reflectivity due to interface imperfections.

For two-material stacks, one usually refers to the material with the lower absorption as *spacer* and to the other as *absorber*. The overall mirror reflectivity characteristics are given by the interference of all partially reflected wave packets. In the case of a periodic multilayer stack with period d highest reflectivity is achieved when all waves add up constructively. This is the case when light of wavelength λ intruding the stack under an angle θ fulfills the *Bragg* condition:

$$m\lambda = 2dcos\theta\sqrt{1 - \frac{2\bar{\delta}}{cos^2\theta}} \qquad (2.29)$$

Here $\bar{\delta}$ is the geometric average of all material specific δ_k values within one period (thickness d) in the stack $\bar{\delta} = \frac{\sum_k \delta_k d_k}{d}$, where d_k

is the individual layer thickness. The square root in equation 2.29 accounts for refraction effects and is sometimes neglected at normal incidence (as $\tilde{n} \approx 1$). One finds, that at normal incidence highest reflectivity is achieved when each optical period thickness $\bar{n}d$ is equal to $\lambda/2$. Thus, in normal incidence XUV coatings typical layer thicknesses range between one and five nm (e.g. $\approx 3 \, nm$ at $E_{max} = 100 \, eV$).

Beside that, the maximum reflectivity of a multilayer coating depends as well on the γ, thus the fraction of *spacer* (*absorber*) material within each period. Assuming without any loss of generality that γ is the ratio of *absorber* material within a stack one can distinguish two extreme cases.

- A *quarter-wave-stack* ($\gamma = 0.5$) is a stack where the (optical) thickness of each layer is exactly equal to a quarter of the wavelength. The reflectivity per period is maximum in that case[4].

- In a *Bragg stack* ($\gamma << 0.5$) the fraction of absorbing material is minimized. Consequently penetration depths are increased, yielding an increased number of contributing interfaces. This can yield a higher maximum reflectivity multilayer stacks with many periods.

The optimum γ is always a trade-off between those two extreme values and depends on the stack materials (with $\tilde{n}_1$, $\tilde{n}_2$, ...), the wavelength λ, the angle of incidence θ, but also on the period number N. As will be shown in the next subsection, periodic broadband optics as useful for attosecond pulse reflection consist of a few periods only. Here high single period reflectivity tends to be more important than a large penetration depth yielding attosecond designs close to quarter-wave stacks in the periodic case.

---

[4] One can express the bi-layer reflectivity R_{period} of a two material multilayer stack with material 1 and 2 in terms of the Fresnel reflectivity $r_{1,2}$, the ratio γ and the diffraction order m (usually $m = 1$) (appendix D, equation D.7)

$$R_{period} = 4r_{1,2}^2 sin^2(\pi m \gamma) \tag{2.30}$$

This value is maximum if $\gamma = 0.5$.

2.2.4.2 Kinematic approximation- Grating analogy

The Bragg condition (equation 2.29) already shows the close analogy of an interference multilayer coating and a diffraction grating. In approximation we neglect both absorption and multiple reflections within a stack and estimate the reflectivity spectrum of a multilayer using the grating analogy. Please note, that the following approximations hold only true for stacks much thinner than the penetration depth.

The maximum reflectivity scales with the number of contributing periods N[5]:

$$r \approx N r_{period} \qquad R \approx N^2 r_{period}^2 \qquad (2.31)$$

The intensity of the side peaks scales correspondingly with $\approx 1/N^2$ to the intensity of the main maximum.

And also the bandwidth of a multilayer reflection coating can be approximated from the number of contributing periods N:

$$\Delta\lambda/\lambda = \Delta E/E_0 \approx 1/N \qquad (2.32)$$

The time-bandwidth analogy (equation 2.7) shows the necessity of *broadband* attosecond optics. Therefore periodic multilayer mirror coatings may only consist of a few periods between $N = 2$ and $N = 30$, depending on the central energy E_0 and the wanted pulse-length τ.

2.2.4.3 Arbitrary stacks

In this subsection, the calculation of both the reflectivity and the transmission of an arbitrary multilayer stack is sketched [48], [49]. Please view figure 2.11 for the appropriate notation.

Calculating the electric fields inside and outside an arbitrary stack, including propagation effects (phase delay and absorption) and multiple reflections of every partially reflected wave-packet originating from each interface is a complex problem. But luckily, as presented in appendix C, the reflectivity of a single layer can be calculated from the reflectivity at its bottom r_{bottom} and the

---

[5]The reflectivity of a grating is given by $R \propto \frac{sin^2(Nk_\perp/2d)}{sin^2(k_\perp/2d)}$.

Fresnel reflectivity on the top r_{top}. One can easily expand this formulation to calculate the reflectivity of multilayer stack. By only looking at the nth layer, the reflectivity $\tilde{r}_{n+1}$ of a n layer high stack is given by the Fresnel coefficient on the top ($r_{n+1,n}$) and the overall stack reflectivity of the multilayer underneath ($\tilde{r}_n$).

$$\tilde{r}_{n+1} = \frac{r_{n+1,n} + \tilde{r}_n}{1 + r_{n+1,n}\tilde{r}_n} \tag{2.33}$$

In this representation, the reflectivity amplitude $\tilde{r}_n$ is defined as the quotient of reflected E_{r_n} and incident E_{t_n} fields, which are defined at the center of each layer[6]: $\tilde{r}_n = C_n^2 E_{r_n}/E_{t_n}$. Phase shifts due to propagation through the individual layers are included here in the propagation factors $C_n = exp(ik_{n\perp}\frac{d_n}{2})$ (with $k_{n\perp} = \frac{2\pi}{\lambda}\tilde{n}_n cos\theta_n$).

So starting from the lowermost layer of a stack, where the overall reflectivity of the underlying stack is simply given by the single interface reflectivity of the substrate and the first layer, one can walk through the multilayer stack, layer-by-layer from bottom to top, ending up with the overall reflectivity ($\tilde{r}_{ML} = \tilde{r}_{N+1}$) of the N layer high stack. Its reflectivity is then given by $R = |\tilde{r}_{ML}|^2$.

Analogically, the transmittance through an arbitrary stack can be calculated by using the following recursive formula:

$$E_{t_n} = \frac{1 - \tilde{r}_{n-1}r_{n-1,n}}{t_{n-1,n}}E_{t_{n-1}} \tag{2.34}$$

where again $\tilde{r}_{n-1}$ is the reflectivity of the $n-1$ layer high multilayer stack, $r_{n-1,n}$ and $t_{n-1,n}$ are the appropriate Fresnel coefficients and E_{t_n} $E_{t_{n-1}}$ is the field amplitude in the nth ($n - 1$st) layer.

These calculations are performable for any stack design, incidence angle and polarization.

2.2.4.4 Reflection from imperfect interfaces

Multilayer mirrors with ideal, abrupt and flat interfaces, as described by the pure Fresnel coefficients, are impossible to fabricate. Real multilayer mirrors have finite boundaries. With single

---

[6] Please spot the appendix figure C.1 for this notation and spot the detailed deduction in appendix C for more details.

layer thicknesses down to 1 nm or less it is clear that small -even atomic-scale- imperfections may affect the overall reflectivity.

Major interface imperfections are atomic displacement as inter-diffusion or intermixing on the one hand and interface roughness from corrugated interfaces on the other [50], [33]. But also chemical compound interlayer formation of two neighboring materials may yield deviations from the ideal case. A prominent example for latter is the formation of $MoSi_2$ interlayers in Mo/Si coatings: $Mo + 2Si \rightarrow MoSi_2$ [51], [52]. Such an interlayer can be modeled by including an additional layer in between the appropriate materials with its compound index of refraction; the validity of such a model depends on the value of characterization, namely the interlayer width, its chemical stoichiometry, any asymmetry in the interface formation and a correct quantification of the period thickness loss.

An example will be presented in section 3.5 where the $MoSi_2$ interlayer formation in ion beam sputter deposited Mo/Si stacks is investigated in detail.
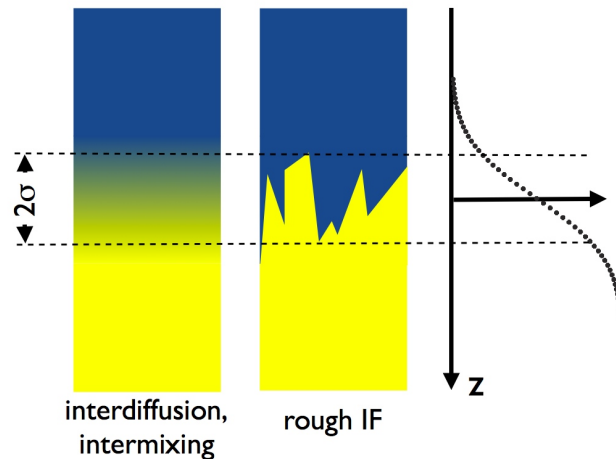
Figure 2.12: Imperfect boundaries: (left) inter-diffusion/inter-mixing; (center) roughness; (right) interface profile function as model for both boundary imperfections.

As illustrated in figure 2.12 both inter-diffusion and interface roughness being averaged over their lateral dimensions, yield the

same average refractive index which is continuously varying along z. Therefore both inter-diffusion and interface roughness can in first approximation be modeled with the same interface profile function $f(z)$ [50], [33]. A one dimensional error-function is usually used as interface profile function [33].

The question arises how to include that into the numerical simulation of an arbitrary multilayer stack. A straight forward way of modeling this continuos interface profile is by replacing each interface by a multilayer stack with thin layers of continuously varying index of refraction[7]. This is of course a time-consuming calculation and not appropriate especially when fitting and optimizing aperiodic designs with many layers.

Much faster is the Fourier transform method developed by Debeye and Waller [53, 54]. An error function like refractive index variation across an interface can be translated into a Gaussian *reflectivity profile*[8] in z-direction:

$$r(z) = r_0(z)f(z) = r_0(z)\frac{1}{\sigma\sqrt{2\pi}}e^{-\frac{z^2}{2\sigma^2}}. \qquad (2.36)$$

Fourier-transform of this relation to momentum space, yields a Gaussian reflectivity distribution dependent on both the wavelength λ and the perpendicular wave-vector amplitude $k_\perp$:

$$r(\lambda) = r_0(\lambda)\tilde{f}(\lambda) = r_0(\lambda)e^{-2k_\perp^2\sigma^2} = r_0(\lambda)exp(-\frac{8\pi^2n^2cos^2\theta\sigma^2}{\lambda^2}) \qquad (2.37)$$

Here, $r_0(\lambda)$ is the wavelength dependent Fresnel reflectivity of a distinct interface.

---

[7] In case of a error function-like varying refractive index from layer m (with $\tilde{n}_m$) to layer l (with $\tilde{n}_l$) across a boundary seated at z_0 with a width σ, the optical constants of a layer inside the "interface stack" at z is given by:

$$\tilde{n}(z) = \frac{\tilde{n}_m - \tilde{n}_l}{2}erf(\frac{z - z_0}{\sqrt{2}\sigma}) + \frac{\tilde{n}_m + \tilde{n}_l}{2} \qquad (2.35)$$

[8]

$$\frac{d(erf(\frac{z}{\sqrt{2}\sigma}))}{dz} = \frac{1}{\sqrt{2\pi}\sigma}e^{-\frac{1}{2}\frac{z^2}{\sigma^2}}$$

Nevot and Croce extended this method of Debeye and Waller to an even more realistic description [33], taking into account the different refractive indices and the different propagation angles of material 1 and material 2.

$$r(\lambda) = r_0(\lambda)exp(-\frac{8\pi^2 n_1 n_2 cos\theta_1 cos\theta_2 \sigma^2}{\lambda^2}) \qquad (2.38)$$

The Nevot-Croce roughness is being used throughout all simulations of this thesis.
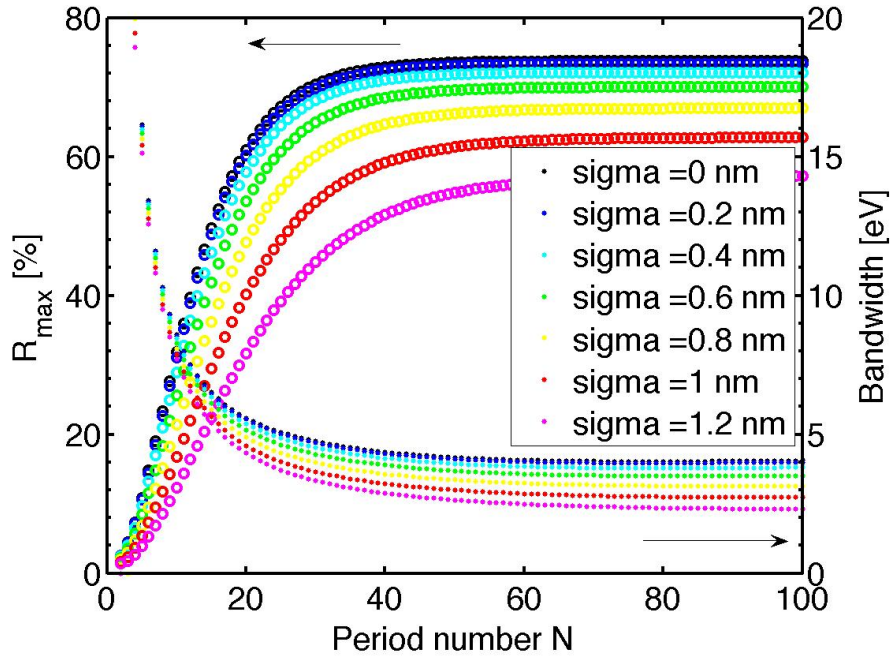
Figure 2.13: Simulated *XUV* reflectivity of a $\gamma = 0.5$ *Mo/Si* coating dependent on both the period number N and the roughness σ.

Figure 2.13 displays the maximum reflectivity calculated for a $\gamma = 0.5$ *Mo/Si* stack in dependence on both the roughness σ and the period number N. Interlayer formation has not been included in this simulation.

One finds, that beside the maximum reflectivity, also the reflectivity bandwidth decreases with increasing roughness in this model and underlines the need of including roughness into realistic multilayer simulations. The decreased bandwidth is a consequence of

the increased single interface transmission due to decreased single interface reflectivity and thus a larger number of contributing interfaces. $T = 1 - R$ is assumed. Please note that only part of the physical effects of boundary imperfections is implemented in the Nevot-Croce model. Non-specular or diffuse scattering, which accounts for non momentum conserved scattering into emergent angles different from the Snell reflection angle is neglected here. Therefore this model is true only if σ is small compared to the layer thickness.

Better models include non-specular scattering, distinguish between correlated and uncorrelated roughness and tackle roughness according to its spatial frequencies [50]. High frequency terms - on the order of the wavelength of the incoming light- yield out of pupil scattering and reflectivity loss and is partly described by the upper model. Mid and low frequency scattering terms on the other hand (including figure errors) can yield destructive interference of rays reflected from different positions of the mirror. These can add up to a bad imaging quality and destroy (partly) the focusing characteristic of the mirror as well as the temporal structure of a pulse.

2.2.4.5   Optimization of aperiodic multilayer coatings

Aperiodic designs offer the possibility of tuning both the spectral and temporal characteristics of a multilayer coating with high degree of freedom. In comparison to periodic stacks, these can be optimized for higher maximum reflectivity [33], larger integrated reflectivity [55], a distinct spectral reflectivity shape [56], negative and positive GDD as well as higher order phase terms [12], [57], [58] imprinted on a pulse upon reflection. They can in principle fulfill all the requirements on attosecond optics as concluded in table 2.1.

Aperiodic coatings for the visible range have yet become workhorses for the generation of ultrashort laser pulses [59], [19]. Adopting these concepts to the XUV spectral range is not straight forward due to high constraints on the optimization, fabrication and

characterization due to much thinner layers and the large absorption of all materials.

The design of all in the following presented multilayer mirrors for attosecond pulse generation/filtering is performed in the spectral domain while tracking the temporal pulse shape simultaneously during optimization. Please note for completeness, that pulse-optimization (e.g. for the shortest pulse) in the time domain is possible [39], but usually spectral constraints as the appropriate bandwidth of the source and requirements on the spectral resolution define the experimental boundary conditions.

The optimization of an aperiodic mirror for shaping attosecond pulses requires detailed knowledge on the experimental set-up namely the spectral characteristics of both the source and all additional optical components as thin metal filters. Secondly, the experimental tsaks as temporal and spectral resolution, a certain central energy or information on certain spectral bands one wants to avoid (e.g. certain Auger-lines in photo-electron spectroscopy experiments), a highest possible signal-to-noise ratio between different spectral ranges, or the need for a distinct amount of GDD have to be formulated and are required to set up reasonable optimization targets.

Figure 2.14 schematically sketches the typical optimization procedure exemplarily for an attosecond mirror designed to introduce chirp upon reflection. Panel a) and b) displays the model for the incident pulse once in the temporal, once in the spectral domain. In the spectral domain (panel b)), the pulse is defined by the source - a Fourier-limited Gaussian is used as reasonable model for the high harmonic cut-off spectrum (black solid line)[9]- together with the transmission (yellow line) and the phase of an additional filter (here 150 nm Zr)[10]. Their combined spectrum is depicted by the blue dashed line. Panel a) shows the temporal structure of the model pulse, including the phase of the filter. The field amplitude (black solid line) and the field envelope are displayed.

---

[9]Details on the high harmonic generation process, its spectrum and the generation of isolated attosecond pulses will be presented in section 2.3.

[10] Thin metal filters will be introduced and analyzed in more detail in section 2.2.5.

(a) Time structure of the incoming pulse, defined by the HH spectrum and the filter

(b) Setting up the target function

(c) Optimized spectrum and GDD

(d) Temporal structure of the optimized pulse
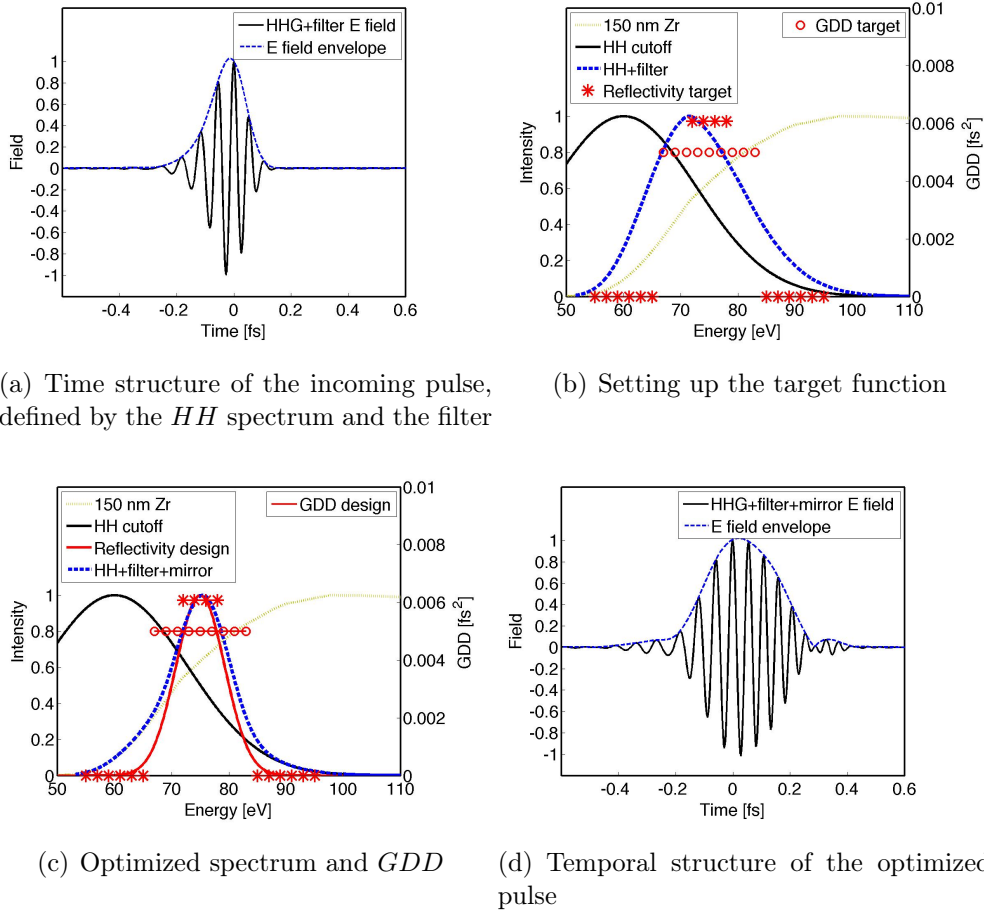
Figure 2.14: Illustration of the optimization strategy for designing attosecond multilayer optics. Please read text for a more detailed description.

Additionally a model target function is displayed in panel b). Discrete points $T_i(\omega)$ are defined in the spectral domain. In this distinct case (1) the pulse's chirp of 5000 as^2 (red circles panel b)), (2) high reflectivity, (3) suppression of the high and low energy reflectance for a (4) spectral bandwidth of the mirror of about 10 eV has been chosen (red stars). Panel c) displays an appropriate reflectivity and the GDD (red lines) of mirror as the model outcome of the optimization procedure. The final pulse intensity as a multiplication of the HHG, the filter and the mirror spectrum is depicted by the blue dashed line additionally. The temporal structure of the chirped pulse being reflected off the mirror is plotted in panel d) and has been calculated by Fourier transform of the

spectrum and the phase combined from the source, the filter and the mirror.

Throughout this thesis the design program *Optilayer*, a Fresnel code coupled to a "needle optimization" algorithm [23], [38] is being used for optimization in combination with self-written Fresnel code to ensure realizability.

The needle optimization [23] inserts small needle-like additional layers at certain positions in the stack, defined by the best figure of merit benefit. These layers are consecutively broadened to their optimum thickness.

Each optimization procedure consists of a number of iterations. Per step the mirror's current design is changed via random walk within user defined constraints. Every design is a trade-off between different target functions. The quality of a design $D_i(\omega)$ is quantized by the figure of merit including user-defined weights w_i that define the importance of the individual target functions $T_i(\omega)$.

$$merit = \sum_i w_i(D_i(\omega) - T_i(\omega))^2 \qquad (2.39)$$

The figure of merit further rules whether the new design is taken as start design for the next iteration step or not.

A properly chosen *start design* is most important for a reasonable result; a simple choice is a periodic (many-material) multilayer mirror consisting of the material combination best suitable for broadband or high reflecting mirrors in the spectral range of interest with an optimized γ value. The period number N of the start design is to be chosen according to the expected final period number. In the case of a nearly linear phase mirror the this thickness can be estimated via the required spectral bandwidth:

$$N = \frac{\Delta E}{E} \qquad (2.40)$$

Another approach is to calculate the penetration depth. Pulse components that are reflected at the top of the mirror must temporally interfere with pulse components being reflected at its bottom, which travel twice through the stack of height h with an average

index of refraction $\tilde{n}$. In the case of a chirped multilayer mirror the pulse-interaction length is defined by the pulse-length τ of either the incoming or the reflected pulse, whichever is longer.

$$h = \frac{c\tau cos\theta}{2\tilde{n}} \qquad (2.41)$$

For the start design of chirped multilayer mirrors one could as well utilize the close analogy of the design of a mirror and its time structure $r(t)$ to come up with a stack design that includes the desired chirp already. The time structure of a pulse reflected off a mirror is given via Fourier transformation ("FT") of its spectral reflectivity $r(\omega)$. Using the kinematic approximation ("KM") [33], one can come up with the following approximated relation[11]:

$$\int_0^\infty |r(t)|e^{i\phi(t)}e^{-i\omega t}dt \overset{\text{FT}}{\sim} r(\omega) \overset{\text{KM}}{\sim} \Sigma_{j=0}^{N}|r_{IF}|e^{2ik_\perp(\omega)z_j} \qquad (2.42)$$

Here r_{IF} is one of the Fresnel coefficients in a bi-layer stack, $k_\perp(\omega) = 2\pi\tilde{n}cos\theta/\lambda$ is the perpendicular modulus of the wave vector and z_j is the position of the jth interface and therefore the design of the stack. As proven e.g. by A. Aquila [60] a quadratically depth graded multilayer chirps or unchirpes a pulse upon reflection. In practice it turned out, that a periodic multilayer with the correct thickness is sufficient as a start design and thus used in the following as a much simpler approach.

Last but not least, the implementability of a final design has to be checked and converted into deposition times using a self-written Fresnel-code algorithm. Interlayer formation, structural changes yielding thickness losses (section 3.6) and a realistic Nevot-Croce roughness is included in the code and both the spectral and the temporal structure of the pulse is analyzed including both the source and the filter characteristics to be able to compare the most realistic pulse simulation with the experimental constraints. Ultra-thin layers as a consequence of the needle optimization procedure are either eliminated or broadened to a realizable value of at least

---

[11]For simplicity only one interface per period is taken into account. An extension to the complete stack with all interfaces is straight forward.

1 nm. If the final design does not fulfill the earlier formulated requirements a new design optimization is necessary either with a better start design or different design target points and weights.

2.2.5   Thin metal filters

Attosecond XUV pump/ IR probe schemes require the separation of the XUV pulse from the driving laser pulse. Thin metal filters of a few hundred nm thickness, which transmit XUV and eliminate laser light have to be used. Beside that, filters allow one not only to spectrally separate the IR/VIS laser from the XUV pulse, but their spectral transmittance characteristics can be utilized to shape the attosecond pulse [61], [62], [63], [19].

Figure 2.15 displays a selection of possible filters usable in the XUV range between 30 and 200 eV. The appropriate optical constants in these calculations have been taken from [64]. The colored curves show filter materials which have been successfully used in attosecond experiments as they withstand the laser.

All following experiments use a 150 (300) nm thick Zr or Pd filter. The lower panels of figure 2.15 depict the transmission of these two materials (in the case of 150 nm thickness) together with the spectral GDD introduced upon transmission. Only near their spectral opening, N edge filters as Zr, Mo and Pd introduce some non-negligible amount of negative GDD. For higher energies the GDD approaches zero. While Pd adds a very small amount of GDD ($GDD_{max} < 1000$ as^2 per 150 nm thickness), Zr (Mo) brings in about twice the GDD of $\approx 2000as^2$ (2500 as^2) upon transmission.

A variation of filter thicknesses gives one a handle to vary both the transmitted XUV spectrum and the introduced GDD to some degree. Unfortunately the availability of filter materials is very limited (as displayed in figure 2.15) and thus one is restricted to a discrete amount of negative chirp and suppression of lower energy harmonics with a filter specific signal to noise ratio. For other spectral ranges, higher spectral resolution or a different amount of chirp (e.g. of positive sign) multilayer mirrors are additionally
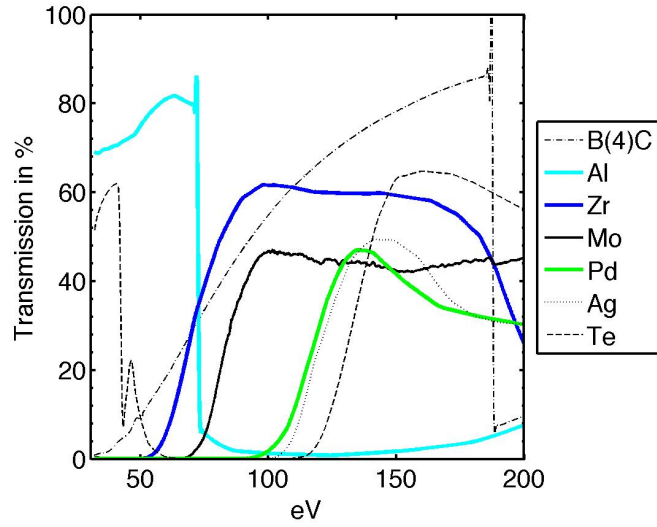
(a) Transmission of selected filter materials
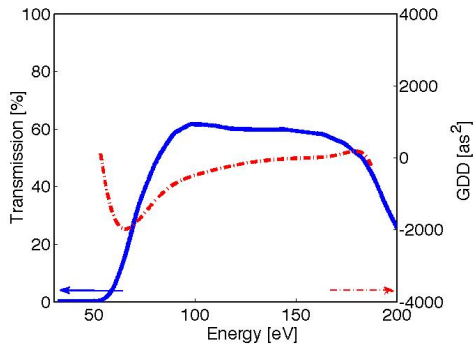
(b) 150 *nm Zr*
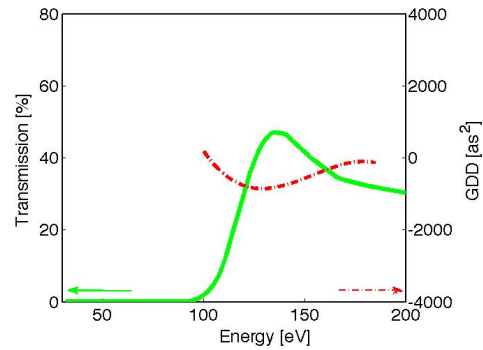
(c) 150 *nm Pd*

Figure 2.15: Panel a) Simulated energy dependent transmission of 150 *nm* thick selected filter materials. Panels b) and c) Transmission and *GDD* of *Zr* and *Pd*.

required.

2.3 Principles of attosecond pulse generation

Right after the invention of the laser [65] the run towards ever shorter light pulses began. The shortest achievable pulse length has always been closely related to technological developments e.g. *Q*-switching [66] or mode-locking. Nowadays, Kerr lens mode lock-

ing [67], [68] enables the generation of few fs long laser pulses in oscillators with titanium-sapphire ($TiSa$) crystals. Chirped pulse amplification (CPA) [69], their consecutive spectral broadening by propagation through gas-filled hollow-core fibers [70], [71] and their compression by aperiodic chirped multilayer mirrors [59] enable today the routine generation of nearly single cycle visible/IR laser pulses with pulse durations of less than 3.5 fs, wavelengths between about 400 nm and 1.2 μm [72], [73], [1] and $\sim mJ$ pulse-energies. These pulses can be phase stabilized [74], [19] and generated with high stability of both the CEP [75], the pointing and the pulse length and energy [76].

As has been analyzed in section 2.1, attosecond pulse generation requires coherent radiation at short wavelengths as from the XUV spectral range. Building an XUV laser in a classical laser setup is up to date not possible due to different reasons. Beside the large absorption of XUV radiation in every material and the consequent lack of high finesse optics, lasing requires population inversion in the lasing material. Due to Einstein [77], both the absorption rate $B_{1,2}$ and the stimulated emission rate $B_{2,1}$ decrease with a power of three in energy in comparison to the spontaneous emission rate $A_{2,1}$ [12] and prohibits population inversion beside in plasma [10]. Consequently different techniques are required to generate coherent XUV radiation and thus enable attosecond pulse generation.

Up to date there are only very few techniques available to generate isolated fs or sub-fs XUV to X-ray pulses: *Femtoslicing* [78] and *free electron lasers* (FEL) utilize the temporal structuring of an electron bunch which can be converted into ultrashort photon bunches using beamline devices as magnets and undulators. In short pulse operation mode, a FEL can produce highly brilliant XUV/soft-X-ray pulses with large photon numbers of $\approx 10^{13}$ within short pulses of a few fs. Photon energies up to 10 keV could be shown at $LCLS$ [30]. Just recently indications for sub-fs features within these pulses have been found [31]. Laser-plasma-accelerators give hope to table-top FEL setups in the future [79],

---

[12] $B_{1,2} = B_{2,1} \propto \frac{A_{2,1}}{\omega^3}$

[80].

Other techniques utilize fs laser pulses as initiators [78] to create plasma [81], for relativistic Thomson scattering [82] or for *high harmonic generation* (HHG).

HHG is the frequency up-conversion in nonlinear multi-photon processes. More detailed, an integer number of photons of the fundamental frequency ω_0 is converted into a single XUV photon, whose energy is a multiple of ω_0. HHG has first been demonstrated in solid targets [83] what is still a very promising method [84] for the generation of isolated attosecond pulses in the future. The following section focuses on HHG in gases, the method all experiments from this thesis have been carried out with and with which the up to date shortest attosecond pulses could be realized [19], [85], [86].

2.3.1   High harmonic generation in gases

HHG in gases is up to date the only technique for the stable generation of attosecond pulses (with $\approx 10^7$ photons) in the XUV. It requires laser intensities on target of about 10^{13} W/cm^2 [87] and has first been observed in 1988 [88]. XUV photon energies far above the water window range have been observed [89], [90].

The spectra of gas harmonics appear with a typical spectral shape: The individual harmonics are spaced by $2\omega_0$. After a steep drop in photon number within the first few harmonics (the *perturbative* regime), a *plateau region* emerges up to the high-energy *cut-off*. A typical measured HH cut-off spectrum, generated with a CEP stabilized laser and filtered by a 150 nm Zr-filter is shown in figure 2.16. The low energy region, thus the perturbative regime and part of the HH plateau region is suppressed here by the filter.

The semi-classical three-step model: The HH spectral shape appeared first unexpected and perturbative models failed to explain the arise of the UV plateau region [91]. The semi-classical three step model [92], [93], [94] had to be developed. Its principle is plotted in figure 2.17.
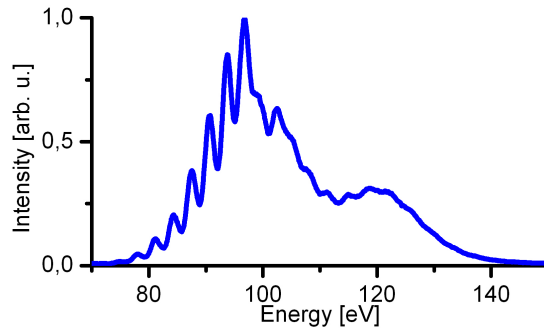
Figure 2.16: Typical HH cut-off spectrum filtered by a Zr filter. This spectrum has been measured at the $AS2$ (appendix F) at the MPQ. (Taken from [35].) The filter suppresses the low energy harmonics from the perturbative and most of the plateau harmonic regime.
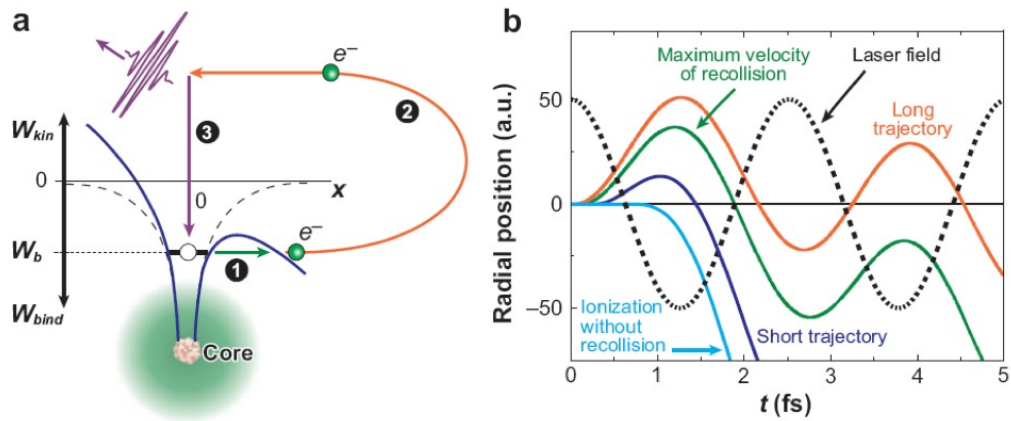
Figure 2.17: a) Schematic view-graph of the HHG three step model. b) Model of the electron trajectories in dependence on their release time (taken from [95]).

The model describes light-matter interaction in that case, where the electric field strengths of the laser *is comparable* in magnitude to the electronic binding field in the atom. The transition energy which separates the "perturbative regime" -in which predominantly conventional single- or multi-photon ionization occurs- from the "suppression barrier regime"[1] -which is described in more detail

in the following- can be estimated by the Keldysh parameter γ [13] [96].

In the presence of strong laser electric fields ($\gamma \lesssim 1$) the atomic binding potential is bent significantly down and electrons can tunnel through the left over potential barrier formed by a superposition of the atomic binding potential I_p and the external laser field (figure 2.17 a) (1)) [95].

These tunneled electrons can be treated (classically) as free [92] with a negligible average initial momentum [1]. These electrons are then accelerated (figure 2.17 a) (2)) by the laser field away from the ions. With the laser field switching sign each electron is decelerated and then redirected in space back to its parent ion. There is a non negligible probability [97] of about $\approx 10^{-5}$ [1], [20] that an electron recombines with its parent ion (figure 2.17 a) (3)), releasing its kinetic energy -picked up from n laser photons- in one single XUV photon of the energy:

$$h\nu_{XUV} = n\hbar\nu_{laser} \qquad (2.44)$$

The semi-classical three step model allows for the accurate simulation of both the probability of the tunneling, the electron trajectories and the released XUV HH photon energy by recombination [98] in very good agreement with complex quantum mechanical dipole response numerical simulations [1]. The temporal confinement of the electron release and the defined acceleration and recombination yields yet a high temporal coherence of HHG radiation.

Attosecond pulse trains: Even the time structure of the emitted HH radiation can be explained by the three step model [1]. In longer laser pulses HHG occurs once in every half cycle of the laser field, whenever the electric field is strong enough to enable

---

[13] The Keldysh parameter is a measure for the nature of a photo-ionization process and compares the maximum laser field strength E_{max} with the ionization potential I_p. ω is the carrier frequency.

$$\gamma = \frac{\sqrt{2I_p}}{E_{max}}\omega \qquad (2.43)$$

electron tunneling. One finds a train of attosecond pulses, spaced with $\tau = \frac{2\pi}{2\omega}$ as first observed by Paul et al. [99]. From Fourier analyses this corresponds to a peaked spectrum with harmonics equally spaced by $\Delta\omega = 2\omega$ (see also figure 2.16, where $\omega_0 \approx 1.6$ eV). The cancellation of even harmonics is a consequence of the spatial symmetry of gases. HH spectra generated in media with broken symmetry (such as surfaces) exhibit the even harmonics in addition [100].

HHG cut-off and long and short trajectories: As depicted by the green line in figure 2.17 b) the high energy XUV cut-off photons stamp definitely from electrons, which are released right after the maximum laser electric field ($CEP \approx 0.05/2\pi$). HHG electrons recombine with the core close before the zero crossing of the field at a CEP of $\sim 0.05/2\pi$.

But the electron release and the consecutive recombination with the ion is not restricted to that single point in time. One distinguishes two sorts of electrons [95], [101], [1], [2]:

- Electrons that are released slightly after the high energy "cut-off electrons" recombine earlier and their released XUV energy is lower due a lower kinetic energies at the time of recombination. Radiation from these "short trajectory electrons" is therefore *positively chirped* (dark blue line in figure 2.17 b).

- Electrons which are released earlier travel a longer distance and get decelerated again by the sign switching laser field before their recombination (orange line in figure 2.17 b)). "Long-trajectory electrons" therefore release *negatively chirped* radiation. Due to their longer travel time their recombination probability is lower compared to the short trajectory electrons.

The preferably generated sort of trajectories can be chosen experimentally by the position of the HH gas target in respect to the laser focus [2]. To avoid destructive interference of generated HH radiation, phase matching over the complete generation volume is

required. Therefore, to avoid the Gouy phase shift of the laser focus the interaction volume and thus the gas target has to be placed outside the focus anyway . Due to their higher efficiency one preferably works with *short* trajectory high harmonics, thus HH radiation is usually *positively* chirped. Mairesse et al. have shown that far off the cut-off, the GD scales about linearly with energy [102] and steepens when reaching the cut-off. Quantum-mechanical calculations [103] reveal in agreement with experimental observations, that the chirp in the cut-off range is mostly negligible.

Finally, for too large laser intensities ($\gamma << 1$), the electric laser field bends the binding potential such, that the electrons can leave the core freely without tunneling. The probability for recombination and thus the probability for HHG gets highly suppressed as most electrons miss their parent ion spatially due to non-vanishing kinetic energies at their release [104], [105]. There is an upper limit for the maximum achievable cut-off energy

$$E_{cutoff}^{max} = I_p + 3.17 \cdot U_p \qquad (2.45)$$

$U_p \propto I/\omega_L^2$ is the ponderomotive potential[14], the cycle-averaged quiver energy of the laser field. So for higher cut-off energies one must either generate HH from systems with a higher binding energy (such as ions), or by driving lasers with larger central wavelengths ω_L.

In analogy, elliptically polarized laser pulses generate hardly HH radiation as again the electrons spatially miss the ions.

2.3.2   The generation of single attosecond pulses

As has been explained in the last section HHG with long driving laser pulses yields the generation of an attosecond pulse train. But many pump probe experiments, as absolute delay measurements in photo-emission from different states [3] or the investigation of

---

[14]

$$U_p = \frac{Ie^2}{2m_0\varepsilon_0c\omega_L^2}$$

Here e is the electron charge, m_0 is the electron mass, c is the velocity of light.

absolute dynamics of a certain sort of electrons [106] require single attosecond pulses to be able to relate the observations to a unique event.

There are in principle two different strategies on how to generate single attosecond pulses: One can either limit the HHG process to such a small time window ("temporal gating"), that only one single attosecond pulse is generated; or one can spectrally filter that part of the HH radiation, from which is known that it stamps from a single attosecond pulse only ("spectral gating"). In the experiment usually a mixture of these two strategies is utilized. Anyway, the next paragraph focuses on the spectral gating technique as major approach behind the experiments presented in this thesis.

Different experimental set-ups for single attosecond metrology have been built and tested over the last few years [18], [107], [63], [35], [108], [62], [109].

Spectral gating: The "spectral gating" technique [15], [110], [111], [18], [74], [35], [3], [112], [5] enabled the generation of isolated attosecond pulses for the first time [15] and the shortest isolated pulses up till now could be achieved [19] (section 4.1.2).

The stable generation of isolated attosecond pulses requires the focusing of few cycle laser pulses with a distinct CEP into a HHG gas target. To do so, one can either stabilize the laser pulse CEP by a feedback loop system [113]; or one can track the CEP of each laser pulse with a CEP meter (e.g. a stereo ATI) and assign it to the pulses afterwards [114]. For the single attosecond pulse generation, latter strategy decreases the effective repetition rate to only a fraction of the original laser repetition rate. Although active phase stabilization is not at all trivial to implement, such laser pulses can be generated routinely at various HHG beam-lines ($AS1$-$AS5$) at the MPQ. All here presented experiments have been performed at one of those.

For short enough driving laser pulses the CEP strongly determines the shape of the laser electric field. This strongly influences also the spectrum and the temporal structure of the nonlinear HHG process as illustrated in figure 2.18. Here, HHG using a 4
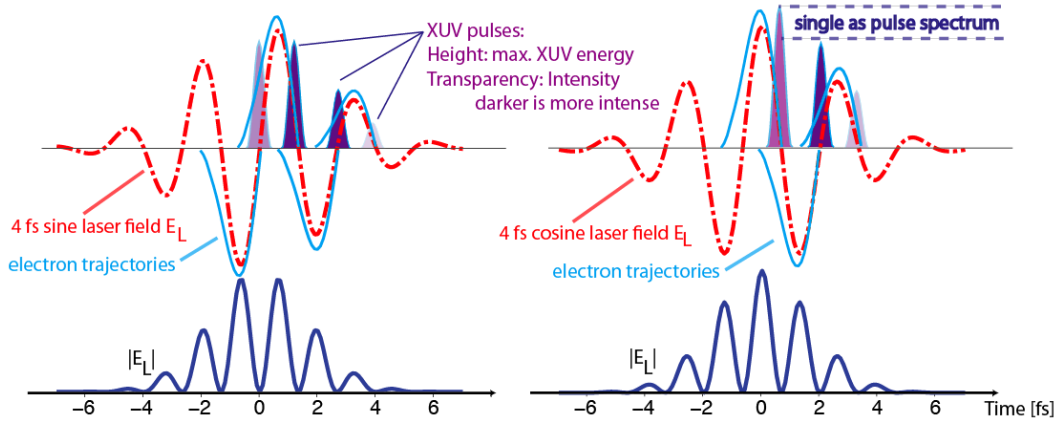
Figure 2.18: Sketch of the HHG attosecond pulse generation process by a 4 fs long pulse laser pulse (with a central wavelength of 800 nm) with a sine (left) and cosine (right) CEP pulse in comparison. For a more detailed explanation, please read the text. This figure has been plotted as a summary of similar figures in [115], [1], [2], [101].

fs driving laser pulse with a sine-like CEP (left panels) is compared to that of a pulse with a cosine shaped electric field (right column). Every laser field oscillation with a large enough maximum field amplitude generates an attosecond pulse (violet peaks). In approximation, the intensity of the individual attosecond pulses (depicted by the darkness of the attosecond pulses in figure 2.18) depends on the ionizing field amplitude at the moment of electron liberation, as this defines the suppression of the tunneling barrier. Its maximum generated photon energy on the other hand (depicted by the height of the attosecond pulses in figure 2.18) scales with the number of picked up photons and thus with the oscillation field amplitude of the following half cycle.

In the case of a cosine CEP laser pulse the maximum field of the central half cycle exceeds that of the neighboring oscillations and the high energy cut-off radiation clearly stamps from a single attosecond pulse. With a bandpass in the spectral range indicated by the black dashed lines in the right panel of figure 2.18 one can spectrally select components of just one pulse. In the case of a sine-like CEP pulse, two attosecond pulses with the nearly identi-

cal spectral components are generated which cannot be separated spectrally.

Spectral components which stamp from a single attosecond pulse appear unmodulated and smooth, while the presence of more than one XUV pulse, sharing the same spectral band, manifests itself in a modulated spectrum. Please view exemplarily the cut-off spectrum plotted in figure 2.16. While the high energy cut-off here appears mostly unmodulated, equally spaced harmonics are visible at the low energy side.

Unlike the usual approach of generating an isolated attosecond pulse with a cosine-like driving pulse, the generation of the shortest ever measured isolated pulses of 80 as (section 4.1.2) has been performed with nearly sine-like CEP laser pulses. The very special experimental conditions using nearly single cycle driving laser pulses allowed for the strong suppression of the "pre-pulse" (most left pulse in the left panel of figure 2.18) by about two orders of magnitude. The broad XUV continuum which could be generated exceeded that from the respective cosine CEP pulse far both in contrast and intensity. This broadband spectrum could be compressed by the consecutive optimized optics (please read section 4.1.2 for details).

Attosecond beam-line set-up: A typical collinear single attosecond pulse generation set-up is displayed in figure 2.19 [47]. Although not all experiments presented in the following have been carried out at this specific beam-line, all beam-lines share the same major components.

Measuring an attosecond pulse by the attosecond streak camera XUV pump- IR probe scheme (section 2.3.3.1) [16] requires an adjustable delay between the XUV and the IR laser pulse [17]. One makes use of the lower divergence of the HHG XUV radiation compared to the laser due to its higher frequency. A thin metal filter in the beam eliminates the laser from the inner traveling path. This filter is mounted at the center of an IR transmittive pellicle, so after passing the filter, the XUV beam co-propagates "inside" the IR laser pulse. Both the XUV beam and the laser beam are
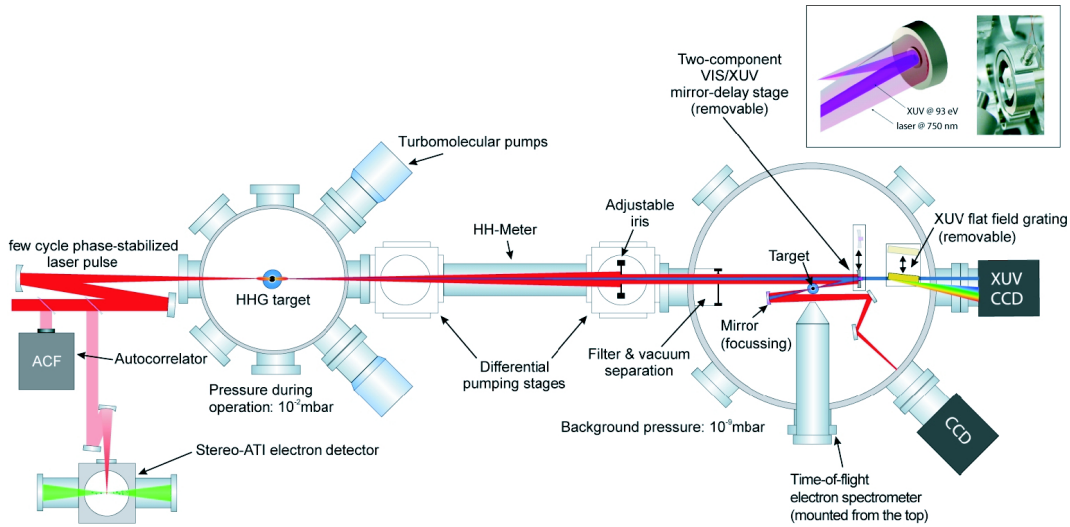
Figure 2.19: Typical collinear single attosecond generation set-up (taken from [47]). For explanation, please see text.

reflected and focused by a "double mirror" under an angle of about 5° normal incidence.

The double mirror: This "double mirror", viewable in the upper right corner of figure 2.19 is a key component in this set-up. Its inner core is movable with respect to the outer part of the mirror by a precision piezo stage. The inner part of the mirror is coated with an XUV multilayer. The outer part reflects the laser. There are three duties of the mirror in this set-up:

1. Focusing both the IR and the XUV pulse onto the sample (focal length is typically $\approx 15\ cm$).

2. Insertion of a delay between the XUV and the laser pulse by moving the inner part with respect to the outer one as required for the attosecond streak camera (section 2.3.3.1) [16].

3. Attosecond pulse shaping.

The final isolated attosecond pulse thus is a convolution of the HH cut-off radiation and the consecutive spectral high-pass consisting

of the filter and the multilayer mirror. Latter can be designed optimized attosecond pulse shaping.

An alternative 45 degree set-up: An alternative 45 degree angle of incidence set-up is introduced and plotted in the appendix F (in detail described in [35]). Here the laser path is spatially separated from the XUV beam path before collinear reunion (Mach-Zehnder-interferometer). A flat 45 degree multilayer coated XUV mirror is used instead of the XUV double mirror. A grazing incidence parabola is used for focusing both beams onto the target.

Thereby both the focusing and the delay is decoupled here from the mirror. As laser optics with high transmission exist off the shelf it is much easier to delay the laser pulse instead of the XUV pulse.

Our experimental proof of quantitative chirp control by multilayer mirrors (section 4.3) has been performed at this beam-line, as it allows for an easy and rapid exchange and fast alignment of the flat XUV optics. The spatial separation of laser and XUV pulse requires a sophisticated actively stabilized interferometric path-length regulation. But once implemented, this beam-line allows for a complete new generation of attosecond experiments, as the spatial separation of the beam paths allows the shaping of both the XUV and the laser pulse independently from each other.

2.3.3 Measuring attosecond pulses

Beside the generation of attosecond pulses, also their detection asks for advanced techniques as no electronics could ever be fast enough to map their temporal structure. First of all, in equivalence to the shutter time in ordinary photography, a gate or probe is required which changes on the time scale of the pulse length. Secondly, a "film" or interaction medium is needed, which uniquely maps this interaction such, that one can retrieve the temporal pulse structure.

Autocorrelation measurements are difficult as multi-photon absorption cross-sections in the XUV are very small [116] and measurements require very high photon numbers. E.g. Tzallas et al.

have used doubly ionized He ions [32] as intensity autocorrelation signal to measure attosecond pulse trains.

$S(\delta) = \int I(t)I(t + \delta t)dt$.

For moderate XUV intensities, as the single attosecond pulses presented in this thesis, two-color multi-photon interactions usually between the XUV pulse and a synchronized IR laser pulse is utilized. The photo-electron spectra from gases, surfaces or solids function as signal. Techniques as the attosecond streak camera [16] (which will be described in detail in the following) or $RABBITT$[15] [99], [62], usually use the HHG driving pulse as probe, as this is intrinsically synchronized with the XUV pulse via the HHG process.

2.3.3.1   The attosecond streak camera

The attosecond streak camera [117] (also named atomic transient recorder (ATR [16]) allows for a very accurate retrieval of both the temporal intensity shape of the attosecond pulse and the vector potential of the driving laser pulse. In addition, it can be used to reveal the relative dynamics between different photo-ionization channels [4], [118], [3], [74].

The ATR is a pump-probe measurement technique and requires the adjustability of delay between XUV and the laser pulse. The corresponding model is illustrated in figure 2.20.

Both the laser and the XUV beam are focused into the interaction medium, e.g a gas target. The XUV pulse creates photo-electrons (depicted by the blue Gaussian in figure 2.20) from each atomic sub-shell. Neglecting the spectral width of the sub-shell state, the corresponding electron pulse is an exact replica of the XUV attosecond pulse; this means, the electron pulse inherits the time dependent spectrum $\hbar\omega$ (shifted by the binding energy of the electron W_b) of the XUV pulse in terms of kinetic energy:

$$W_{kin}(t_0) = \hbar\omega - W_b \qquad (2.46)$$
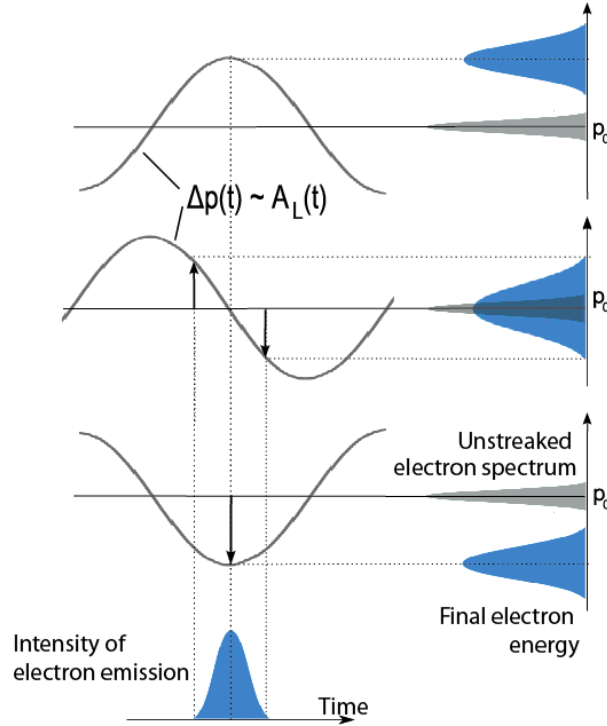
Figure 2.20: Illustration of the attosecond streak camera. The attosecond XUV pulse generates free photoelectrons from the target atoms, which are accelerated in the laser field. The final electron kinetic energy depends on the delay between the XUV and the IR laser pulse and therefore can be used as signal. For a detailed explanation, see text.

Before the ionization, the electrons are strongly bound within the atomic potential and hardly affected by the laser field. After ionization, the photo-electrons can be treated as free electrons with an instant momentum $p(t_0) = \sqrt{2mW_{kin}(t_0)}$. These electrons are accelerated by the laser electric field $E(t)$. Their time dependent momentum $p(t)$ is given by:

$$p(t) = p(t_0) - e \int_{t0}^{t} E(\tau)d\tau = p(t_0) - eA(t_0) + eA(t) \qquad (2.47)$$

After the laser pulse has passed, their final momentum gain is proportional to the vector potential at the time of their ionization $A(t_0)$[16]:

$$=> p(\infty) = p(t_0) - eA(t_0) \qquad (2.48)$$

---

[16] $A(\infty) = 0$ as no laser is present at $t = \infty$.

As the attosecond XUV pulse is shorter than one complete laser oscillation the average kinetic energy of the electrons is shifted in energy dependent on the delay between the laser and the XUV pulse as displayed in figure 2.20. Lining up all electron spectra due to their delay, yields a typical spectrogram or streaking trace as displayed in figure 2.21.
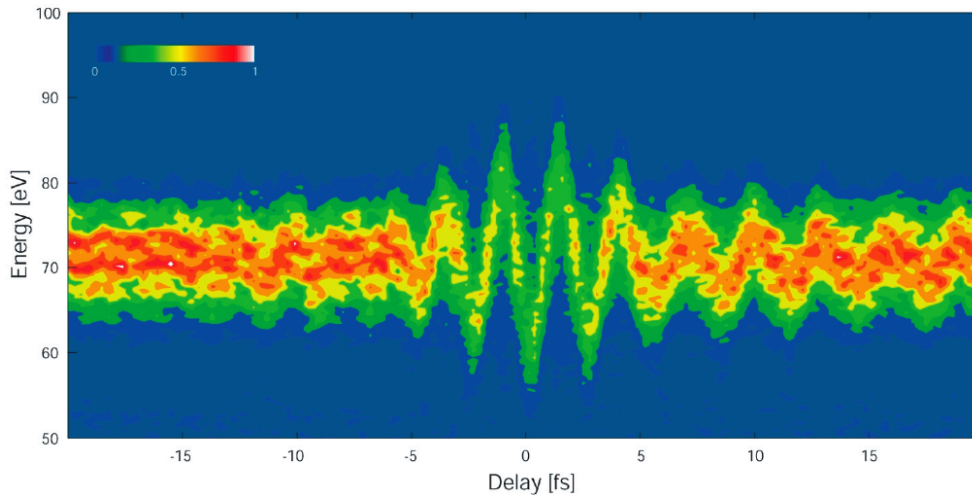
Figure 2.21: Typical streaking trace scanned over delays of 40 fs (taken from [47]). The streaking field shifts the $13eV$ broad electron spectrum by 8-9 eV.

Analyses of these spectrograms can be performed by Frequency-Resolved Optical Gating for Complete Reconstruction of Attosecond Bursts analyses ($FROG/CRAB$) as described in detail in [119], [120], [121], [122]. $FROG/CRAB$ allows for a complete reconstruction of both the vector potential of the IR laser and the intensity as well as nonlinear phase terms and thus the temporal structure of the attosecond XUV pulse. Via random walk optimization, the program adjusts parameters as the laser vector potential, the XUV spectrum and the XUV phase such, that best match is found between the calculated an the measured spectrogram. Throughout this thesis a "blind" $FROG/CRAB$ retrieval has been performed. This means, no additional information as the XUV spectrum is initially fed into the program.

Luckily, streaking spectrograms can be analyzed to some extend by bare eye without the need for complicated reconstruction

algorithms:

- The center of mass of a streaking curve is in very good approximation a direct measure of the laser vector potential as one can see when rewriting equation 2.48 in terms of energy:

$$W(\infty) = \frac{p^2}{2m_e} = \frac{1}{2m_e}(p(t_0)^2 - 2eA(t_0)p(t_0) + e^2A(t_0)^2)$$
(2.49)

  For typical moderate streaking laser fields, the last term is very small and the net gain in energy is directly proportional to the vector potential of the laser:

$$\Delta W(\infty) \propto \frac{ep(t_0)}{m_e}A(t_0)$$
(2.50)

- The spectrum of the attosecond pulse is given by the "broadness" of the electron streaking curve. As already stated, the electron pulse is in first approximation an (energetically shifted) replica of the XUV pulse. So the XUV spectrum can either be retrieved by $FROG/CRAB$ analyses or just identified as the shifted photo-electron spectrum in absence of the laser streaking field. Please note, electron spectra from different origins may overlap as will be explained in paragraph 2.3.3.2; their separation, and thus a correct interpretation of the signal is not always trivial.

- Even the sign and the magnitude of the chirp of an attosecond pulse can be easily identified from a spectrogram. A linear chirp of the pulse causes a linear sweep of initial photoelectron momenta over time depicted by the slanted black straight lines in figure 2.22. The laser field transfers a momentum Δp to the XUV-released electron that is proportional to the vector potential $A(t)$ of the streaking field at the instant of release. As a consequence, $A(t)$ also sweeps the electron momentum near its zero crossings. This laser-induced sweep is positive (negative) at the positive (negative) slope of $\Delta p(t)$ respectively. Depending on its sign, it increases or decreases

the initial sweep of photoelectron momentum imposed by the chirp of the ionizing attosecond XUV pulse. This, in turn, gives rise to a broadening or narrowing of the corresponding final momentum (energy) distribution (streak image) at the zero crossing of the laser vector potential.
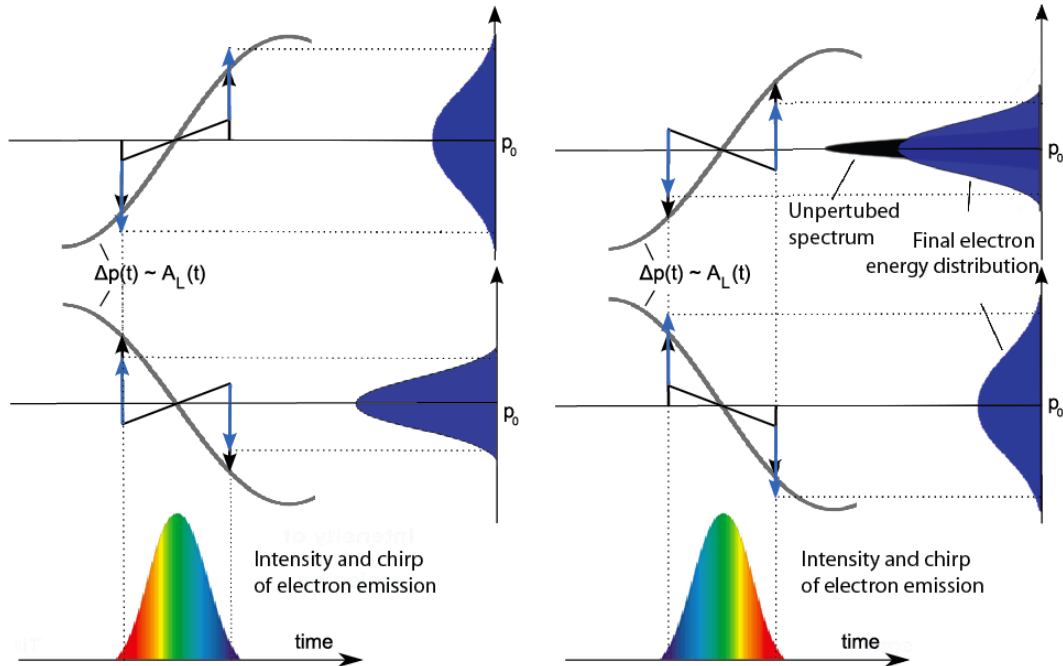
Figure 2.22: Streaking of a chirped pulse. The left and right panel corresponds to a positively and negatively chirped pulse, respectively. Dependent on the slope of the vector potential, the electron bunch is either broadened or narrowed as a consequence of additional momentum from the chirp. For a more detailed description, please see text.

2.3.3.2 Photo-electron spectra

The attosecond streak camera utilizes photoelectron spectroscopy. A perfect electron pulse replica as exhibited ideally from a single and infinitesimally sharp electronic state is assumed in the $FROG/CRAB$ retrieval. Experimentally each spectrogram contains electrons from different origins and their separation may be necessary for a correct result:
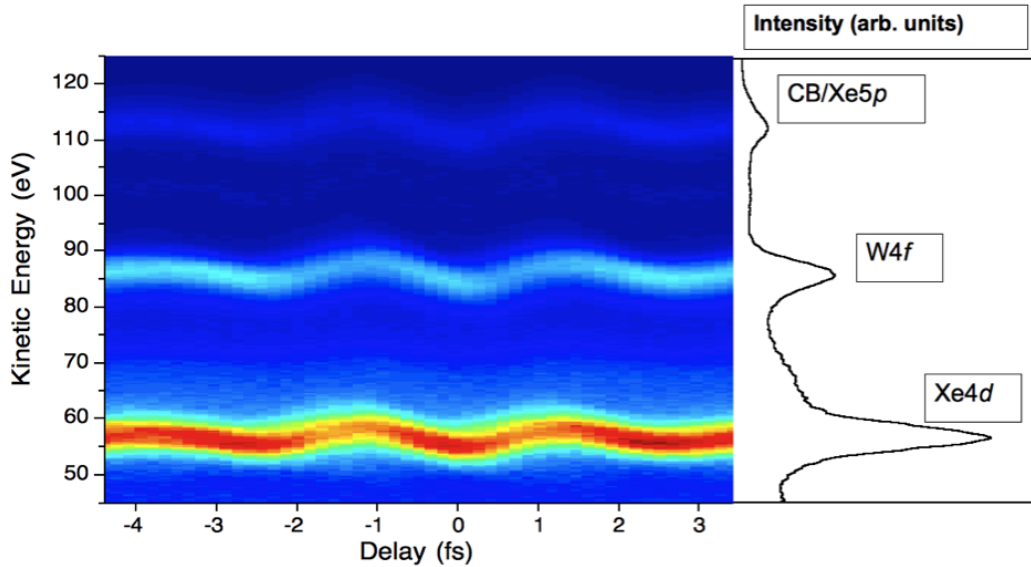
Figure 2.23: Measured spectrogram of a solid sample, where a Xe mono-layer has been prepared on a $W(110)$ crystal. This spectrogram has been measured at the $AS3$ beam-line with a spectral cleaning mirror in the right column of figure 4.21 in section 4.4. Delays between the individual ionization channels can be revealed by comparison of the center of mass of the individual traces [118], [123].

- A photo-electron XUV pulse replica is generated from every individual atomic sub-shells. If those are spectrally separated their classification is easy and even the relative delay between different photo ionization channels may be revealed by a simple comparison of the center of mass of the distinct streaking curves (figure 2.23 [118]), [5], [3]. On the other hand, the finite width and the manifold of states may be neglected if the electronic states are very close to each other. E.g. in Ne the $L2$ and the $L3$ states have an electron level width $< 10^{-3}$ eV and their binding energies are only ≈ 0.1 eV apart [64]. One usually assumes identical ionization times of both states. Partly overlaying spectra are difficult (or impossible) to separate and attosecond pulses with a smaller spectral width may be necessary. Appropriate small band optics with a high spectral signal to noise ratio for a clear separation of energetically

neighbored states will be presented in section 4.4.

- Each electron streaking curve is sitting on top of a low-energy background composed of inelastically scattered electrons and contributions from several shakeup channels and an ATI electron background (typically up to 30-40 eV) generated from multi-photon absorption from the co-propagating streaking laser. Due to its complexity the analytical form of its energy dependence is obscure, but it was found that a properly chosen cubic function appropriately models its behavior. An example of an experiment using a chirped mirror (section 4.3) is displayed In figure 2.24).

The subtracted function is fully described by the two highlighted points $x1$ and $x2$ together with the gradient at those points. By varying the endpoints $x1$ and $x2$ to within a reasonable margin and comparing various techniques to eliminate spectral components from the satellite pulse, it was found found that the retrieved GDD hardly changes.
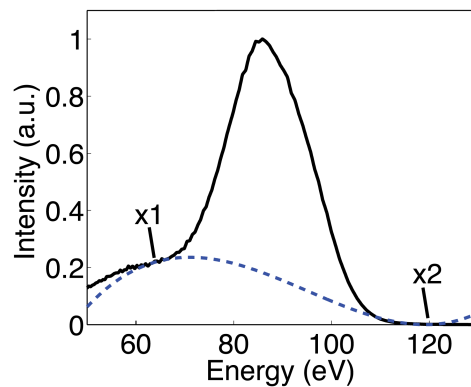
Figure 2.24: Illustration of the cubic background subtraction from photoelectron spectra (here Ne). The black curve displays the summed up spectrogram versus the energy. The dashed blue line curve illustrates the cubic background which is being subtracted. For more detailed information please read text.

Due to inelastic scattering solid state photo-electron spectra appear even more complicated as exemplarily visual in figure 2.23. Each primary electron peak is accompanied by a broad-

band low energy secondary electron tail, which again may be subtracted by a cubic function in analogy to figure 2.24.

- Even small contributions from satellite pulses generated half a laser oscillation before or after the main pulse yields their own complete streaking trace that overlays the main signal and shifted in time by π. In the chirped multilayer proof of principle experiment (section 4.3) contributions from such a small satellite pulse ($I_{satellite} < 10\% I_{main}$) could be well eliminated by numerically subtracting a shifted replica of the spectrogram from itself.

Chapter 3

Realization and characterization of XUV multilayer coatings

This chapter provides all necessary information on the fabrication and metrology of multilayer mirrors presented in this thesis. Ion beam sputter deposition and different multilayer characterization techniques are introduced (section 3.1). The calibration of material specific deposition rates of the five materials Mo, Si, B_4C, La and Sc is presented in section 3.2; deposition homogeneity is tested and could be improved as presented to the end of this section. The layer materials Mo, Si, B_4C, La and Sc allow for a coverage of the spectral range between 30 and about 200 eV with both high-reflecting and broadband multilayer optics as will be proven in section 3.4. The correct fabrication of multilayer mirrors requires the conversion from multilayer designs to deposition times and thus knowledge about interlayer formation or thickness compression/increase. Before summarizing the models which are used for a realistic implementation of the mirror-designs in section 3.6, compound silicide formation in Mo/Si multilayers is investigated in detail in section 3.5 as necessary prerequisite for a correct model for the implementation of (a-)periodic multilayer designs in the next chapter 4.

3.1 Methods

After presenting ion beam sputter deposition (IBD) different characterization methods are introduced. XUV and X-ray reflectometry, transmission electron microscopy (TEM) imaging, ellipsometry and profilometry have been used to characterize both the deposition rates and the multilayer coatings. For a reverse characterization of the mirror design, e.g. for the analysis of thickness loss due to interlayer formation, a self-written fit algorithm connected to a Fresnel code as described in appendix E has been utilized.

3.1.1 Ion Beam Sputtering

Today XUV multilayer coatings have been realized by various deposition techniques. The most prominent methods are electron beam evaporation [124], [125], [126] and magnetron sputtering [127], [128], [52], [129], [40] with which the up to date highest normal incidence Mo/Si reflectivity of $\approx$ 70 % near the EUV lithography wavelength of 13.5 nm could be realized [124], [127]. Beside these, pulsed laser deposition [130], [131], chemical vapor deposition [132] and ion beam sputter deposition [133], [134], [135] have been used. All of the following presented multilayer mirrors have been fabricated by the latter method.

Sputtering techniques as magnetron sputtering or ion beam sputtering are usually very stable deposition techniques. These allow for sputtering of all materials independently of their (e.g. melting point) characteristics, which is a big advantage compared to e.g. evaporation techniques. This allows for time- controlled deposition, without the need for in-situ thickness monitoring [33]. Typical single layer thickness errors below 0.01 nm are possible [33].

Ion beam deposition in particular uses an external ion source. Thereby the ion energy and the ion current can be controlled independently. Ion beam deposited films are very dense compared to e.g. thermal evaporated films [136]. Neutralizing the sputter ions avoids charging of the target materials and allows for the deposi-

tion of metals, semi-conductors and insulators. One disadvantage using an external ion source is the unavoidable implementation of sputter gas impurities in the deposited films. A large distance between the target material and the substrate diminishes this effect. Ion beam deposition rates are usually very low (typically between 0.01 and 0.1 nm/s in our case) what ensures a very controlled deposition, sacrificed by long fabrication times of several (1-20) hours per coating.
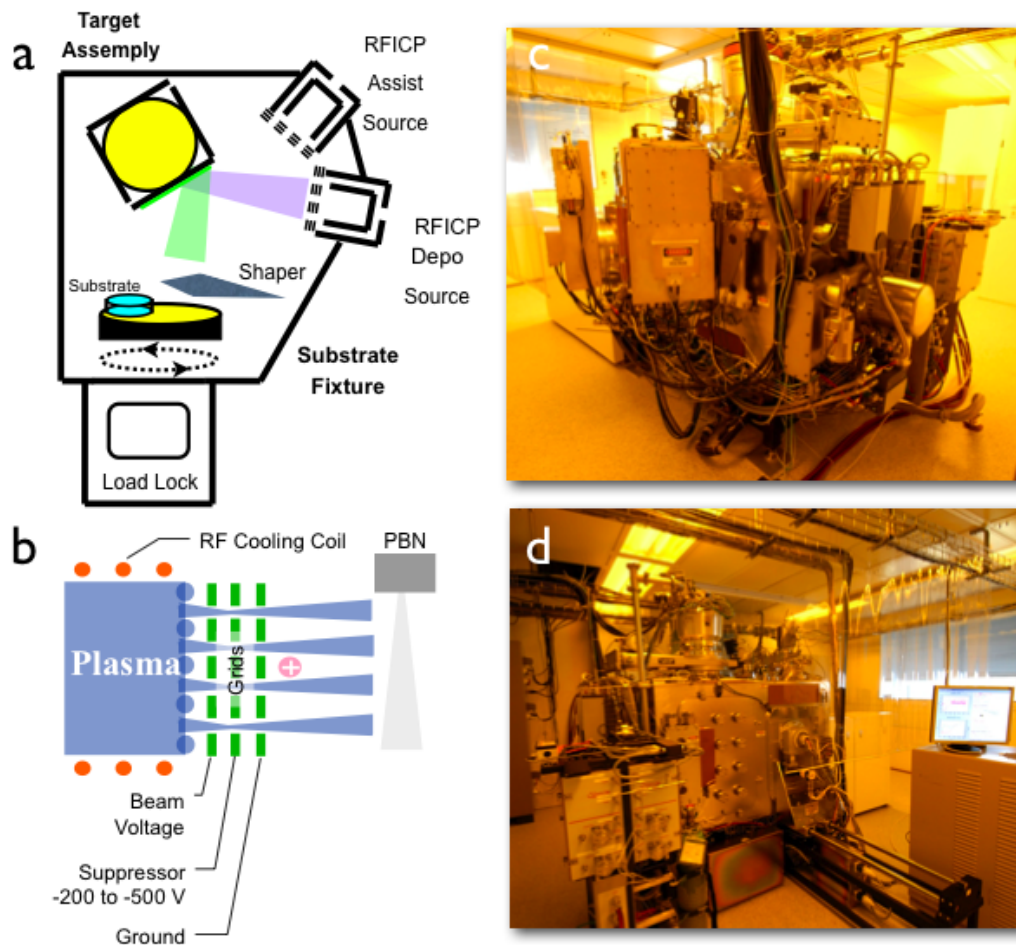

Figure 3.1: IBD located at the MPQ: a) Schematic set-up b) Illustration of the 3 grid ion optic (taken from [136]) c) ion source view d) front side view [137].

A schematic view-graph (a) of our ion beam deposition IBD tool (*Nexus IBD-0* of *Veeco Instruments*) and the 3 grid ion optic

(b) together with photographs of the complete experimental set-up (c,d) is displayed in figure 3.1. This sputter tool is completely load-locked and located inside a class 1000 clean-room environment.

Noble gas (usually Kr) plasma is generated by an inductively coupled RF generator. Electrons from a plasma bridge neutralizer (PBN) tungsten filament electron source trigger the first particle hits and start the plasma burning. Ions are extracted from the plasma, accelerated and focused onto target materials via a curved 3 grid ion optic [138]. The ion beam is neutralized on its way towards the target by means of the PBN to avoid charging of the target. The neutralized ions hit the target wheels (about 40 cm in diameter) under an angle of about 35 degrees normal incidence. Up to 4 targets are loadable at the same time. Material is ablated from the target wheel and deposited on the sample (near normal incidence), which is located ≈ 0.5 m away from the target. Typical background pressures of 10^{-8}-10^{-9} $mbar$ assure clean layers. The substrate holder is spinning during the deposition process with 40 rpm for an increased lateral deposition homogeneity.

For a beam of low divergence and a focus on the target without destroying the grid optics certain parameter constellations are required[1]. Typical ion energies are 600 eV. An ion current of 200 mA is achieved by a coupled in RF power of 210 W. The suppressor grid has an electric potential of -200 V to the first grid. The same beam parameters are used for all materials for a higher stability when producing multilayered samples.

Sputter yields and target energies have been calculated for the materials Mo, Si, B_4C, La and Sc and are comprehended in table 3.1. The simulation has been performed with the Monte Carlo particle simulation code $SRIM$ (The Stopping and Range of Ions in Matter) [140]. The 600 eV Kr ion energy has been chosen to

---

[1] supplied by Veeco Instruments [139]:

$$0.6 < V_b/(V_b + V_s) < 0.8 \qquad (3.1)$$

$$I \sim 2 \cdot 3216 \sqrt{40/Z_a} 10^{-9} (2 \cdot 2/(1+1))(V_b + V_s)^{3/2} \qquad (3.2)$$

All values are dimensionless. Here V_b and V_s is the beam and the suppressor grid voltage, respectively. I is the beam current, Z_a is the atomic number of the sputter gas.

sputter target ions with low kinetic energy on the order of ≈ 10 eV, which are expected to have a high sticking coefficient on the substrate [141] without sputtering the deposited film [140].

Table 3.1: Simulated sputter yield and target atom energy

Target material	Mo	Si	La	B	C	B_4C [2]	Sc
sputter yield (target atoms/ Kr atom)	1.3	1.0	1.4	0.5	0.4	0.7	0.6
kinetic energy of target atoms [eV]	27	11	34	10	12	14	11

3.1.2 XUV/ soft X-ray reflectometry
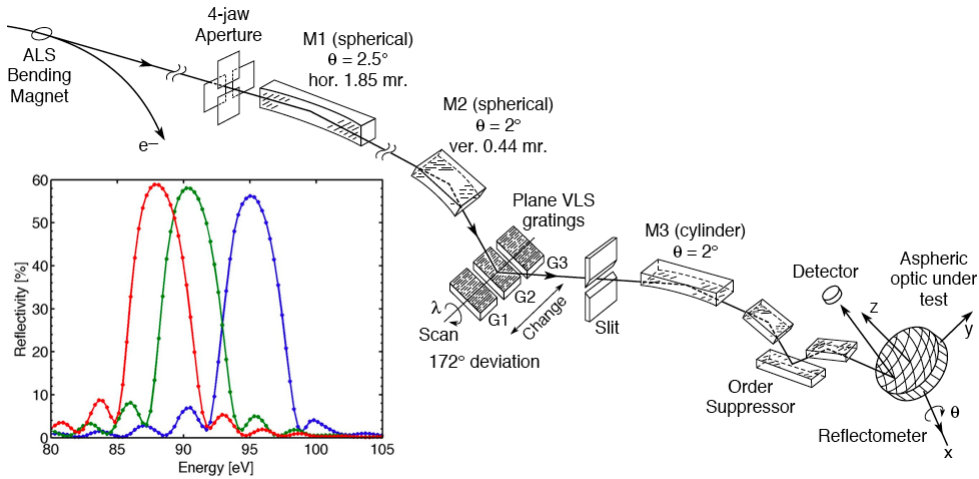
Figure 3.2: Sketch of ALS beam-line 6.3.2 (taken from [143]). The inset shows three XUV reflectivity measurements of a "graded" ($N = 30$, $\gamma = 0.45$) Mo/Si multilayer under an angle of $\theta = 5$.

An absolute measurement of the XUV reflectivity of a multilayer mirror requires a stable and well calibrated XUV source. Most XUV measurements have been performed at the beam-line 6.3.2 of the *Center for X-Ray Optics* ($CXRO$) at the *Advanced*

---

[2]From literature [142] it is known that B_4C is deposited mostly as stochiometrical B_4C. $SRIM$ calculations can only be performed with atoms. The atomic mass of Mn is close to the molecular mass of B_4C. To simulated the sputtering of B_4C molecules, the $SRIM$ simulations were performed for Mn assuming the B_4C bulk density of $2.52 g/cm^2$.

Light Source (*ALS*) [143]. This beam-line is especially designed for measuring optics in transmission or reflection as a function of the photon energy or the incidence angle.

The experimental set-up is depicted in figure 3.2. Different XUV/soft X-ray optical components as gratings, multilayer mirrors and apertures allow for the adjustment of the XUV/soft-X-ray energy between 30 eV and 1.3 keV. Absolute reflectivity measurements are possible by normalizing the reflected (transmitted) intensity $I(\omega)$ by the directly measured beam intensity I_0. Both measurements are corrected for the storage ring current (I_{ring} and $I_{0,ring}$) and dark current (I_{dark} and $I_{0,dark}$):

$$R(\omega) = (\frac{I(\omega) - I_{dark}}{I_{ring}})/(\frac{I_0(\omega) - I_{0,dark}}{I_{0,ring}}), \qquad (3.3)$$

Thereby one yields a measurement accuracy in the absolute reflectivity performed e.g. for a typical Mo/Si multilayer mirror with a central reflectivity around 90 eV of 0.1 % [143]. A wavelength accuracy of 0.1 %, a spectral purity of 99.75 % and a dynamic measurement range of 10^{10} have been achieved in this particular measurement[143]. Other XUV reflectivity measurements in this thesis have been performed at the $BESSY$ synchrotron multilayer beam-line with a similar accuracy and set-up [144].

3.1.3   Hard X-ray grazing incindence reflectometry (XRR)

Grazing Incidence X-Ray Reflectometry (XRR, also $GIXRR$) [145], [33] allows for analyzing the multilayer structure and reveals information on the Nevot-Croce roughness. In the following mostly a $Mo\ K\ \alpha$ source (17.4 keV) has been used. The experimental set-up is plotted in figure 3.3. Please note that unlike usual convention, the grazing incidence angle is denoted with ϕ throughout this thesis. A *Goebel* mirror, a multilayer coated paraboloid functions in this set-up both as monochromator and beam parallelizer and is needed to separate the $K\ \alpha_1$ from the $K\ \alpha_2$ line. Three apertures, one before the sample (typical width: 40 μm) and two behind the sample (typical slit widths are 200/ 250 μm)
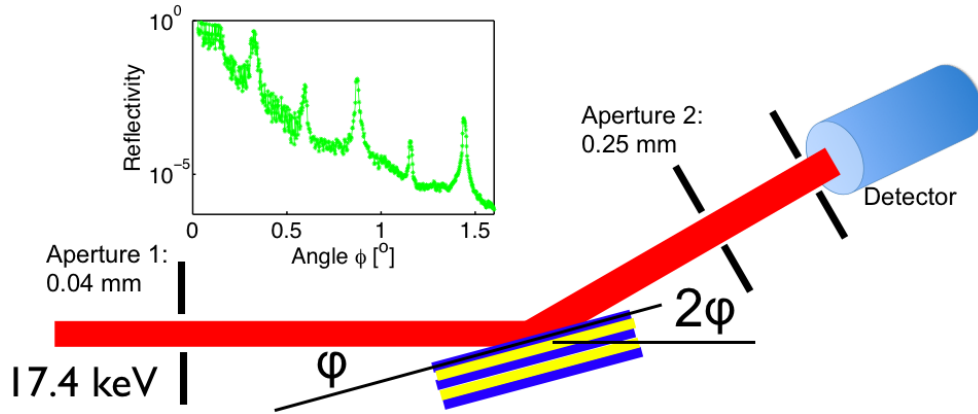
Figure 3.3: Sketch of the XRR ϕ-2ϕ (usually named θ-2θ) measurement set-up. The inset shows the XRR measurement of an 120 period, $\gamma \approx 0.4$, $d \approx 6.8$ nm Mo/Si stack.

define the illumination function and the acceptance angle. Each sample is scanned in a ϕ-2ϕ geometry between $\phi = 0^o$ and $\phi \approx$ 1-5°.

Two detectors are used to eliminate intensity fluctuations, one recording the intensity of the incoming light I_0, one that records the reflected signal I simultaneously. A typical measurement lasts for $\approx$ 6 hours. Calibration of the data is performed in the following way:

1. The average dark signal of ≈ 1 ct/s is subtracted from both I and I_0.

2. At grazing angles only part of the beam illuminates the sample and can be reflected towards the detector. This effect is compensated analytically by incorporating the measured illumination function.

3. The absolute reflectivity is given by $\frac{I}{I_0}$.

For a retrieval of the multilayer structure from the measurements, a self-written multilayer Fresnel code (appendix E) is used. For a good comparison between the measurement and the simulation signal averaging due to the finite source and the beam divergence is included in the simulation.

The Nevot-Croce roughness revealed in XRR measurements may occur lower than the corresponding value from the XUV measurement. This could originate from increasing roughness throughout the stack. Due to the deeper penetration of X-rays compared to XUV light, the average Nevot-Croce XRR roughness is measured farther within the stack by XRR. Beside that, material impurities may affect the XUV and XRR measurements differently. Other uncertainties can originate either from a bent sample, from alignment errors or slightly different source characteristics at different source powers.

3.1.4   Transmission Electron Microscopy (TEM)

Transmission electron microscopy images of multilayer cross sections have been taken with an electron microscope $TITAN$ of FEI [146]. This atomic resolution microscope allows for a spatial point resolution of $< 0.2\ nm$ [147]. Pictures in this thesis were recorded with 300 keV electrons. TEM imaging requires the preparation of ultra-thin cross section samples. Cross-section samples of multilayer coated Si wafer witness samples with tens of nm thickness only could be prepared by grinding and polishing.

3.1.5   Spectral ellipsometry

In situ white light ellipsometry is a powerful measurement technique that can reveal both of the $IR/VIS/UV$ optical constants and the structure of a sample at the same time [148]. Ellipsometry makes use of a change in polarization and intensity of radiation upon reflection off a (multi-)layered sample at a fixed angle of incidence. These changes are material- and wavelength- dependent, but as well influenced by the sample design. The energy dependent ellipsometric parameters $\Psi(\omega)$ and $\Delta(\omega)$ are defined by the ratio of the reflection amplitudes of p and s polarized light. For each frequency ω one gets:

$$\rho = \frac{r_p}{r_s} = \frac{|r_p|}{|r_s|} e^{i(\Phi_p - \Phi_s)} = tan(\Psi)e^{i\Delta} \tag{3.4}$$
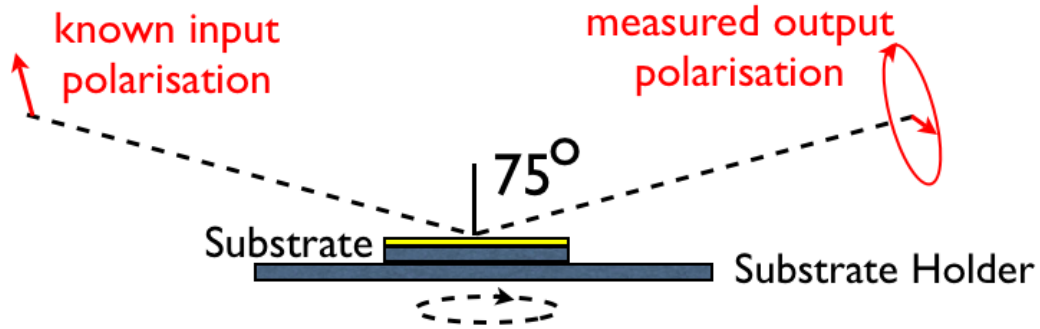
Figure 3.4: Sketch of the ellipsometer principle

Thus $tan(\Psi) = \frac{|r_p|}{|r_s|}$ and $\Delta = \Phi_p - \Phi_s$. From these parameters, one can calculate the optical constants $\tilde{n}$ and the film thickness using the appropriate Fresnel coefficients (equation 2.27). The calculation is straight forward but lengthy and is usually performed numerically.

As depicted in figure 3.4 a spectral ellipsometer EC-400 ($Woolam$) and a M-$2000VI\ Xe$ lamp is flunshed to our deposition chamber under an angle of 75° allowing for in situ ellipsometric measurement between 240 and 1700 nm during deposition.

In situ white-light ellipsometry allows for the measurement of the optical constants of a sample in a broad spectral range at a certain instance of time. Knowing the optical constants of the materials the individual layer thicknesses can be fitted. Ellipsometry is very accurate for measuring single layers or few layer stacks with an accuracy of $< 0.1\ nm$ assuming correctness of the model. In multilayered stacks of higher complexity also the models become more and more complex and the appropriate fits become less unique.

In this thesis ellipsometry has been used to measure the $IR/VIS/UV$ optical constants of the used materials and to calibrate the deposition rates. Analyses of the recorded data is performed with the "Easy-to-Use Acquisition/ Analyses Software for Spectroscopic Ellipsometry Program" ($EASE$) [149]. Appropriate fit models are already implemented and will be presented in detail in section 3.2.

3.1.6   Profilometry

Profilometry gives access to the surface profile of a sample. A cantilever rasters the surface along one line on typical length scales between a few μm to 200 mm. Here a *Dektak 150 Stylus Profiler* (*Veeco*) has been used. This tool is especially suitable for absolute height measurements at thick single layer samples (with typical layer thickness between 300 and 800 nm) and is used for rate calibration or comparison measurements for the deduction of thickness loss in multilayer samples. The error of a single measurement is about 5-10 nm basically originating from mechanical noise. Also the systematic calibration error of this tool can be estimated to that range. A large number of measurements on thick samples allows its reduction to a statistical error in the deposition rates to less than 1 ‰.

3.2   Deposition rate calibration

Multilayer coatings presented in the following consist of a combination of the semiconducting materials Si and B_4C [142] and the metals Mo, La and Sc. IBD rates are very stable and no changes from run to run have been observed[3]. Long term comparison including the exchange and reinstallation of target materials revealed a change in the rates of less than 5 %.

Profilometry on single-layers and in situ ellipsometry on few-layer samples is used for the deduction of the deposition rates.

In situ ellipsometry requires models on both the optical constants and the structure of the stack for a reasonable fit of the single layer thickness at an instant of time yielding the average deposition rate. A three layer stack model is used to simulate each coated Si wafer sample: $[Si_{cryst/bulk}/SiO_{2,amorph}/X]$, where X is the deposited material. Both the average offset angle -which can arise from a not perfect alignment, from bending of the sample or from a wobbling motion of the substrate holder, which is spinning during deposition and measurement- and the native SiO_2 layer

---

[3]*Veeco Instruments* specifies the repeatability to $< 1\%$ [136].

thickness -which is formed on top of the crystalline Si wafers- is fitted ellipsometrically before the deposition. This sample-individual information is included in the consecutive model. Typical SiO_2 thicknesses range between 15 and 25 Angstroms and offset angles of about 0 ± 0.05^o are found. Also metal "quasi-bulk" layers BL can be used as appropriate substrates and a model of the form $[BL/X]$ (again with the angle offset included) is used in that case. For the retrieval of the optical constants, which are required prerequisites for a reasonable fit of the layer thickness, material specific models are used and the strategy for their retrieval differs for metals and semiconductors.

Deposition rates/ optical constants of Mo, La and Sc

Due to the limited penetration depth of $IR/VIS/UV$ light in metals, their optical constants can easily be extracted from ellipsometrically recorded data of thick (typically $> 100~nm$) "quasi-bulk" samples. Here the ellipsometer parameters Ψ and δ do not change with increasing layer thickness and the optical constants can be read off by averaging a reasonable time interval. Once knowing the optical constants, the individual layer thicknesses can be fitted for each time step.

The extracted optical constants of Mo, La and Sc and the fitted thicknesses are plotted in figure 3.5(a), figure 3.5(b) and figure 3.5(c), respectively. The used models and the number of fitted samples is denoted in the figure legends.

As expected the thickness fits become less unique when approaching the limit of transparency; only a reasonable thickness range is used for the deposition rate retrieval. The average Mo deposition rate from five different samples yields a deposition rate of $0.060 \pm 0.016~nm/s$ fitted from thicknesses smaller than $50~nm$ (figure 3.5(a)). This is in reasonable agreement with the average value of $0.063 \pm 0.003~nm$ from profilometer height measurements on bulk samples. Equivalent studies on La (three samples) for layers smaller than $60~nm$ reveal a deposition rate from ellipsometer measurements (figure 3.5(b)) of $0.092 \pm 0.017~nm/s$ and
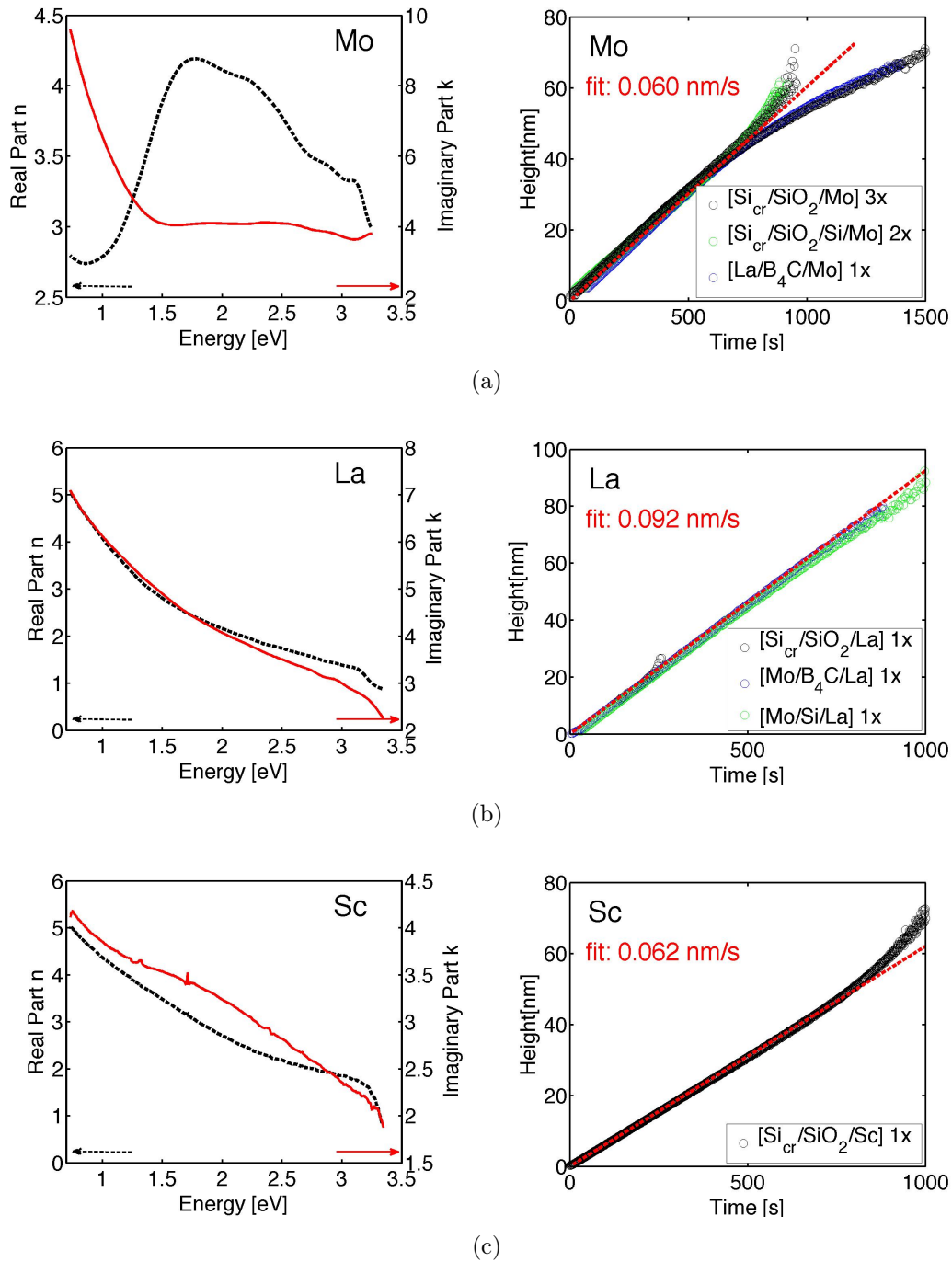
(a)

(b)

(c)

Figure 3.5: Left column: $NIR/VIS/UV$ optical contants of deduced from optically thick "bulk" layer. Right column: Fitted constant thickness increase (red dashed line) against deposition time, correspondingly. Each line shows the measurement for a distinct material (a) Mo, (b) La, (c) Sc.

$0.093 \pm 0.003 \ nm/s$ from the profilometer. Ellipsometrical measurements and fits for Sc and layer thicknesses smaller than $70 \ nm$ (figure 3.5(c)) give $0.062 \pm 0.031 \ nm/s$ compared to 0.058 ± 0.002 nm/s measured on average with the profilometer (figure 3.5(c)).

Deposition rates/ optical constants of Si and B_4C

The semiconducting materials Si and B_4C remain transparent in the visible range for even "thick" layers of a few hundred nm. Their thickness and the optical constants have to be fitted simultaneously by appropriate models. The *Lorentz-oscillator model* exhibits the characteristics of an amorphous semiconductor [148], [149]. TEM cross-sections of our multilayers confirm the deposition of Si and B_4C in an amorphous state (e.g. figure 3.14 in section 3.5).

In the Lorentz-oscillator model each electron is assumed to be bound to its atom with the resonant frequency E_i. The interaction with light can be described by a damped harmonic oscillator model. The complex dielectric function $\tilde{\varepsilon} = \tilde{n}^2$ can be thus written as

$$\tilde{\varepsilon}(E) = \varepsilon_1(\infty) + \sum_{i=1}^{N} \frac{A_i^2}{E_i^2 - E^2 - iB_iE}$$

where ε_1 is the real part of dielectric functions at large energies, N is the number of oscillators with the amplitude A_i, the central energy E_i and the bandwidth B_i of each oscillator. Setting E_i to zero represents the Drude term which models free electrons in a metal or a semiconductor [148]. The Lorentz resonator model is very well suited for modeling the optical constants in semiconductors above the band-gap [148]. But also at resonance energies, this model works very well and can be improved by more than one oscillator per electron.

We make use of that in the case of Si and use three oscillators to dynamically fit the ellipsometrically recorded data. Figure 3.6 displays a typical fit (black dashed lines) for certain selected wavelength (here only the data of Ψ is shown) using three oscillators. The appropriate retrieved oscillator parameters are summarized in
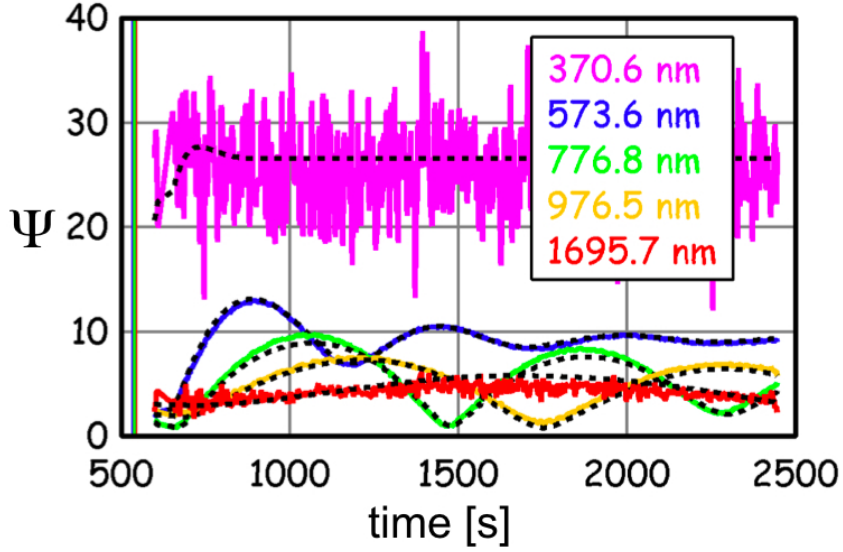
Figure 3.6: Colored curves: Measured data Ψ plotted for a selection of wavelengths during Si deposition. The black dashed lines display the appropriate fits using the Lorentz oscillator model from table 3.2.

Table 3.2: Lorentz Oscillator model parameters for Si. All A, B and E values are given in units of eV:

$\varepsilon_1(\infty)$	1		
osc. 1	$A_1 = 71$	$B_1 = 0.45$	$E_1 = 3.58$
osc. 2	$A_2 = -77$	$B_2 = 9.0$	$E_2 = 4.09$
osc. 3	$A_3 = 56$	$B_3 = 2.68$	$E_3 = 3.52$

table 3.2. Figure 3.7(a) (left panel) displays the corresponding optical constants.

The retrieved oscillator parameters fit well to the single oscillator model published by Tompkins et al. [148] who found $E = 3.85$ eV, a transition strength of $A = 15.1$ eV and a broadening energy B of 2.00 eV. We find a Si deposition rate (figure 3.7(a); right panel) of 0.061 ± 0.08 nm/s in excellent agreement with rates from profilometer measurements of 0.0605 ± 0.002 nm/s.

Also for B_4C the Lorentz oscillator model has been used. The lack of electronic resonances within the measurement spectral range allows for the sufficient usage of a single oscillator model (table 3.3). Figure 3.7(b) shows the retrieved optical constants and the thickness increase during sputtering. We deduce a rate of 0.0119 ± 0.027

(a)

(b)
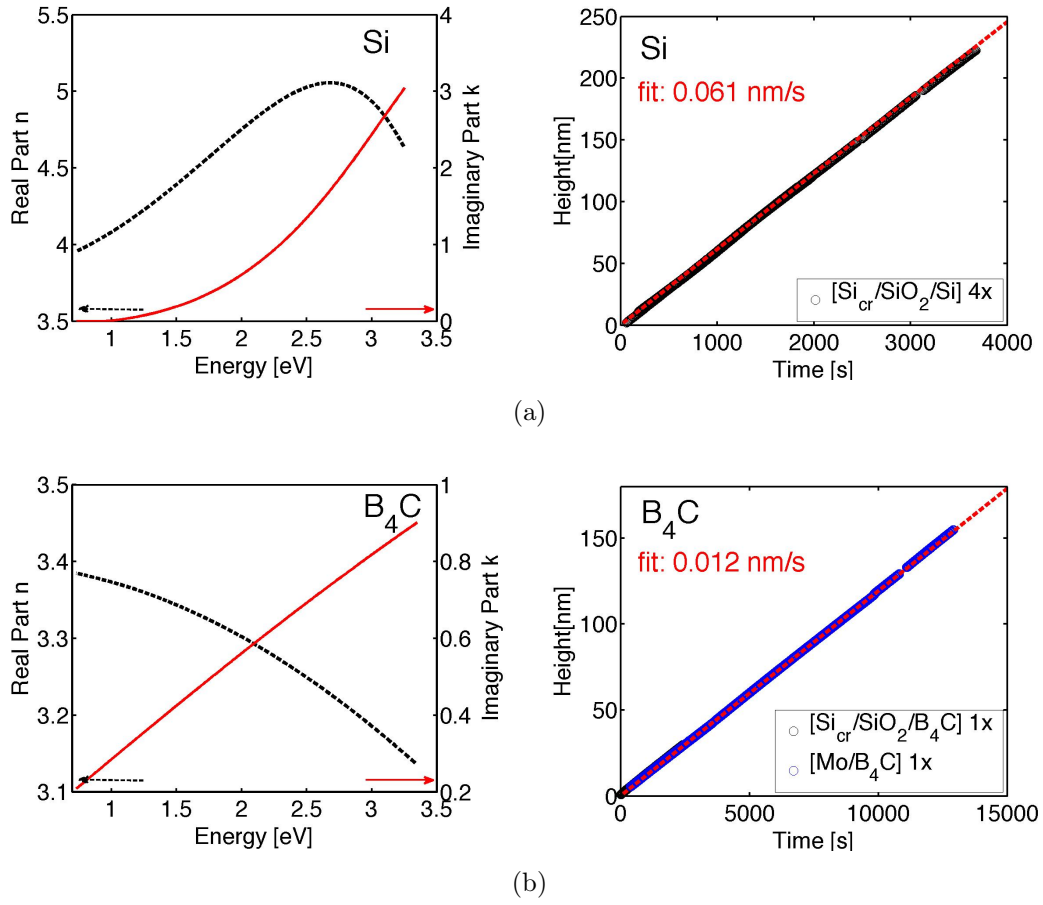
Figure 3.7: Left: $NIR/VIS/UV$ optical contants of Si (B_4C) from a triple (single) Lorentz oscillator model. Right: Fitted thickness (red dashed line) against deposition time .

Table 3.3: Lorentz Oscillator model parameters for B_4C. All A, B and E values are given in units of eV:

$\varepsilon_1(\infty)$	1		
osc. 1	$A_1 = 12.8608$	$B_1 = 16.9975$	$E_1 = 4.432$

nm/s, again in good agreement with the profilometric deduced rate of $0.0117 \pm 0.0005\ nm/s$.

The constant thickness increase and its agreement with profilometer values in all materials independent of the substrate, confirms the correctness of the used models.

3.3   Analyses and improvement of the deposition homogeneity

The effective deposition rate depends both on the distance of the substrate surface to the target and the deposition cone geometry; therefore the rates have to be calibrated both in lateral and in perpendicular direction of the substrate holder. For the realization
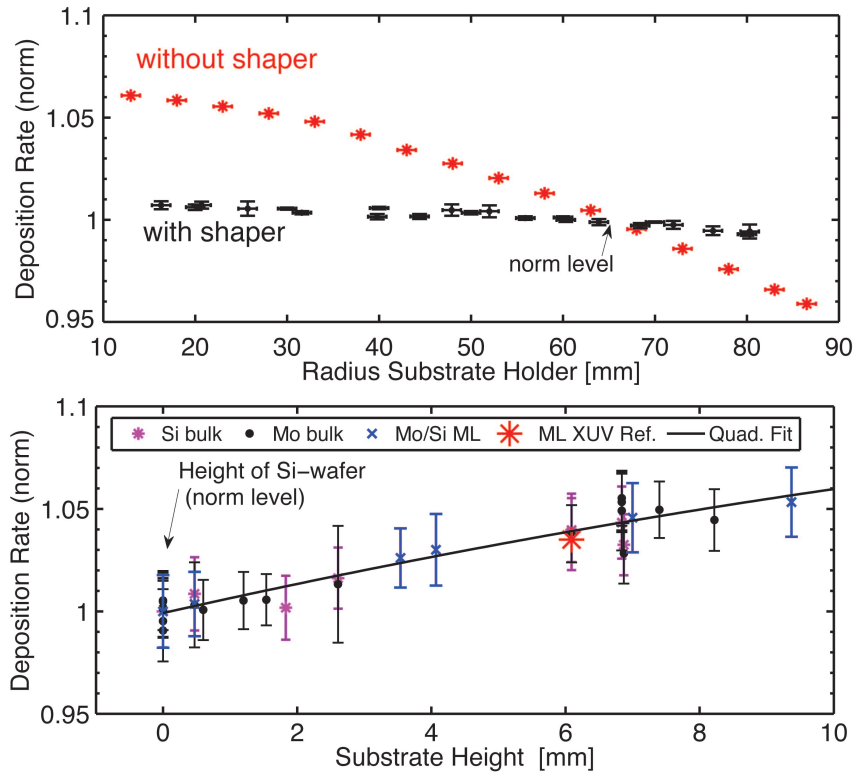
Figure 3.8: Upper panel: Homogeneity increase by a geometric shaper. Dependence on the lateral position of the substrate from the center of the substrate holder with (black dots, measured by profilometry) and without shaper (red stars, deduced by comparing the central energy E_0 of XUV multilayer reflectivity measurements [143]). Lower panel: Dependence on the height of the substrate surface above the holder. Beside the "red star" (multilayer XUV reflectivity measurement [143]), profilometer data of thick Si samples (violet stars), thick Mo samples (black dots), and Mo/Si multilayer coatings are shown and fitted (black line) for an analytical relation for the height-dependent deposition rate.

of lateral homogenous coatings, a geometrical shaper has been de-

signed and mounted in between the sputter target and the spinning substrate holder (as displayed in figure 3.1 a)). Thereby the lateral rate inhomogeneity could be reduced from $\pm 5\%$ deviation from the mean value to only $\pm 0.5\%$ in a lateral radius of 8 *cm* as plotted in the upper panel of figure 3.8. Rest deviations may originate from shadowed deposition and an a-centric spinning of the substrate holder.

Including this shaper, the geometrical rate dependence could be reduced to a dependence on the substrate height as displayed in the lower panel of figure 3.8. One can easily compensate that either by bringing all substrate surfaces to a fixed reference height on the substrate holder using jacks or by simply multiplying the sputter times with a height dependent factor (black line, figure 3.8).

3.4   *XUV* multilayer material selection between 30 and 200 *eV*

Both the achievable reflectivity in the spectral range of interest and the tunability of the spectral characteristics of multilayer mirror designs depend on its material combination. One benefits from low absorbing materials (small β) with refractive indices farthest separated in the complex plain[4] and low interface roughness.

The following simulations show, that by an energy dependent combination of the materials *La*, *Mo*, *Si*, B_4C and *Sc* one can cover the complete spectral range between 30 and 200 *eV* with both high reflecting and broadband multilayer mirrors. This case study is the basis for the choice of later fabricated and analyzed multilayer mirrors. In subsection 3.4.1 the optical constants are investigated in detail. As will be demonstrated in subsection 3.4.2 our analyses revealed the necessity of a new high-spectral-resolution measurement of the optical constants of *La*. In section 3.4.3 the best suitable material combinations are identified from reflectivity simulations of both the Fresnel coefficients and periodic multilayer

---

[4]Equation 2.28 shows that the single interface reflectivity scales with the distance of the optical constants $R_{singleIF} \propto \delta^2 + \beta^2$

mirrors.

3.4.1   Optical constants of Mo, B_4C, Si, La and Sc
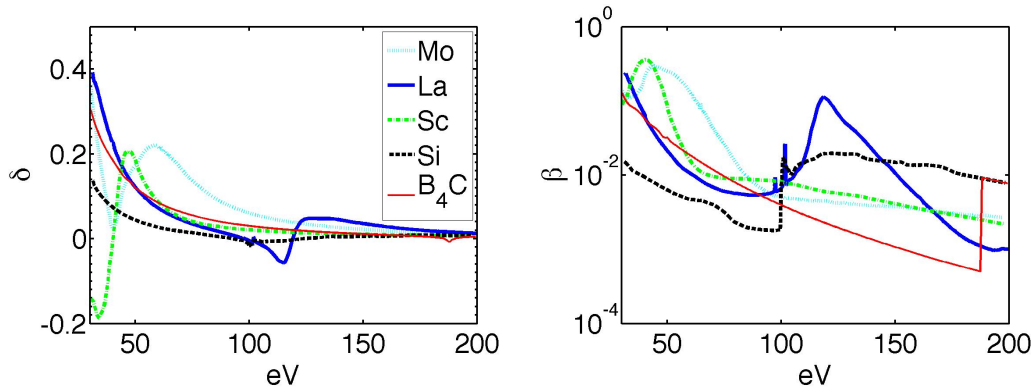
Figure 3.9: Optical constants of Mo, Si, La, Sc and B_4C in the spectral range between 30 and 200 eV. The left panel shows the $\delta = 1 - Re(\tilde{n})$, i.e. the deviation of the real part of the refractive index from 1 (linear scale). The right panel displays the imaginary part β of the refractive index (logarithmic y-scale).

Figure 3.9 displays the optical constants of Mo, B_4C, Si, La and Sc in the energy range between 30 and 200 eV. δ and β are typically on the same order of magnitude (about $10^{-1} - 10^{-3}$ at 100 eV) and exhibit a decline behavior with increasing energy as predicted by equation 2.18 ($\beta, \delta \propto \lambda^2$). Deviations from this trend occur only in the vicinity of electronic absorption edges. Table 3.4 comprehends those in the range between 30 and 200 eV (from [64] and [26]).

Apart from La, data for the optical constants of all materials plotted in figure 3.9 have been taken from the $CXRO$ database [64]. The presented refractive indices of Mo [153], Si [154], and B_4C [155] have been measured by Soufli et al., while A. Aquila and co-workers published the optical constants of Sc [156], [157].

When starting experiments on La based multilayer mirrors, it came to our surprise, that the commonly used optical constants of La [158] lack sufficient spectral accuracy especially in near-

Table 3.4: Absorption edges of *Sc*, *Mo*, *Si*, *La*, and B_4C between 30 and 200 *eV*; all energies are given in *eV*.

Element	Edge 1	Type 1	Edge 2	Type 2	Edge 3	Type 3
Sc	28.3	$M_{2,3}$[150]	51.1	M_1[150]		
Mo	35.5	N_3[151]	37.6	N_2[151]	63.2	N_1[151]
Si	99.2	L_3[26]	99.8	L_2[26]	149.7	L_1[150]
La	34.3	O_1[150]	102.5	N_5[150]	105.3	N_4[150]
	196.0	N_3[150]	205.8	N_2[152]		
B	188.0	K_1[150]				
C	-					

absorption edge features. Thus, the optical constants of *La* arise from our own measurements presented in detail in the following.

3.4.2 High spectral resolution measurement of *La* optical constants in the *XUV*/ soft *X*-ray range
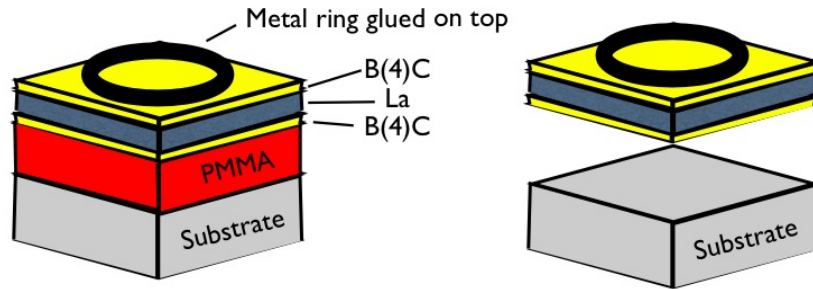
Figure 3.10: Preparation of free-standing *La* films for a retrieval of the optical constants.

High spectral resolution measurements of the optical constants of *La* have been performed at the beamline 6.3.2 at the Advanced Light Source (*ALS*) between 30 *eV* and 1.3 *keV* [143] using free-standing *La* foils of different thicknesses (50 *nm*, 75 *nm*, 100 *nm*, 150 *nm*) coated with 10 *nm* B_4C on both surfaces to suppress oxidation. The foils have been prepared by depositing three-layer $B_4C/La/B_4C$ coatings on *Si*-wafer substrates which have been pre-coated by a thin film of photo-resist (*PMMA*) as sketched in figure 3.10. The layer thicknesses were obtained from $Cu - K\alpha$

XRR measurements. Consecutive data analyses revealed e.g. a 49.95 nm thick La layer between two 9.99 nm thick B_4C layers on 149.7 nm $PMMA$ and similar good agreement for the other foils. The coated Si wafers were attached to filter supports and the photo-resist was dissolved, releasing the thin foil from the Si wafer (figure 3.10).

The XUV transmission data of the foils as a function of photon energy were recorded. The appropriate measurement step sizes are displayed in table 3.5.

Table 3.5: Spectral resolution of the absorption measurements of the La optical constants plotted in figure 3.11

Energy[eV]	32 -49	49-80	80-110	110-111.5
$\Delta E[eV]$	0.125	0.2	0.05	0.2

Energy[eV]	111.5-182	182-280	280-927	927-1300
$\Delta E[eV]$	0.4	0.5	1	2

The real part of the index of refraction δ has been calculated from the directly measured absorption part β via Kramers-Kronig relations[5] [159], [160]. For a more reliable Kramers-Kronig analysis data from other sources have been added for a full spectrum imaginary part of the index of refraction between 14 eV and 15 keV. Above 1.3 keV data from the $CXRO$ database measured in 2007 [64] has been used. Below 30 eV we completed our data-set with β values from Kjornrattanawanich and Seely et al. [161], [162]. After all we have obtained a consistency sum rule value of 55.1 electrons, which is in reasonable agreement to the ideal value of 56.6 [163].

Figure 3.11 compares our results (blue solid line) with the optical constants tabulated in [64] (depicted by the red dashed line). Due to the improved spectral resolution of the measurements, some deviations from the tabulated data could be revealed. This is most

---

[5] It is a common approach to only measure β (equivalent to f_2^0 due to equation 2.18) and then retrieve the real part δ (equivalent to f_1^0 due to equation 2.18) via Kramers-Kronig relation.

$$f_1^0(\omega) = Z - \frac{2}{\pi} P \int_0^\infty \frac{\tilde{\omega} f_2^0(\tilde{\omega})}{\tilde{\omega}^2 - \omega^2} d\tilde{\omega} \qquad (3.5)$$

This relation is valid for any meromorphic complex relation and relates its real to its imaginary part.
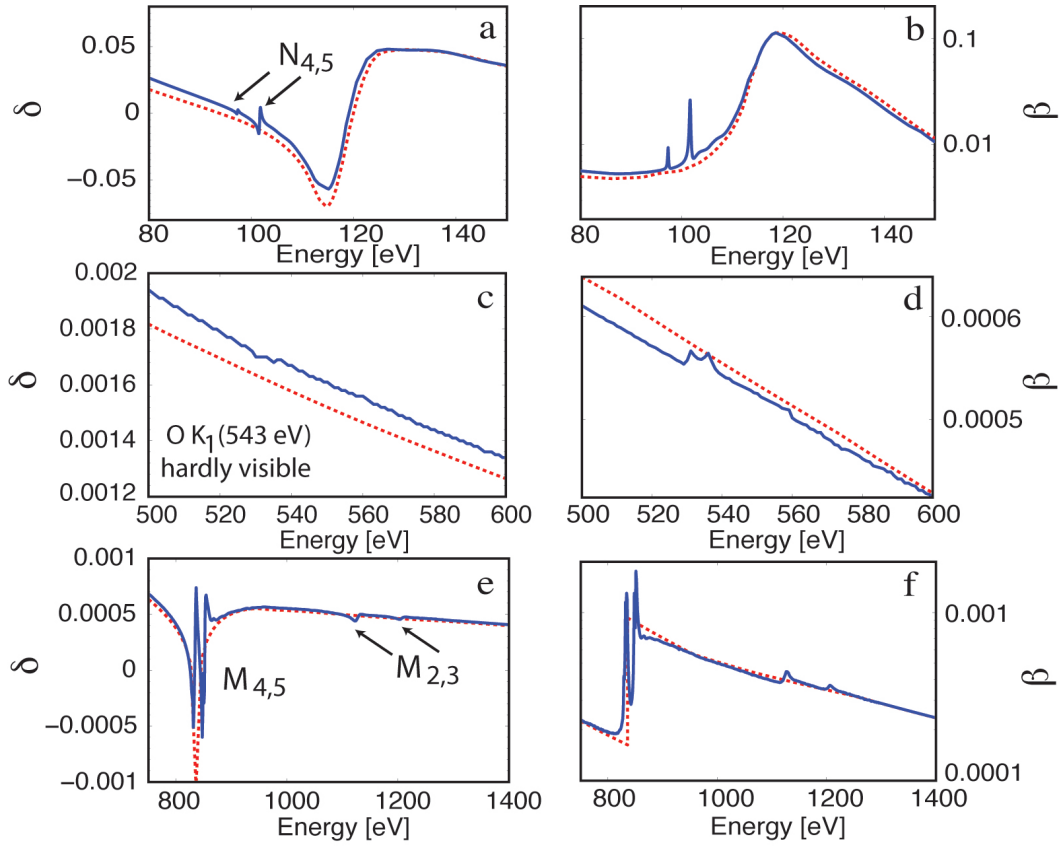
Figure 3.11: Novel measurement of the optical constants of *La*. *XUV*/soft *X*-ray optical constants (solid blue lines) are displayed in comparison to the commonly used ones from the *CXRO* database [64] (red dashed curves) for selected energy ranges. δ is plotted in the left column, β is plotted in the right column respectively on a logarithmic y-scale.

noticeable around 100 eV at the $N_{4,5}$ absorption edges (N_4: 105.3 eV; N_5: 102.5 eV [150]) (panels a and b) as well as around 840 eV at the $M_{4,5}$ absorption edges (M_4: 853.0 eV; M_5: 836.0 eV [150]) (panels e and f). Furthermore, the hardly visible oxygen (O) absorption edge at 543 eV (panels c and d) indicates that the freestanding La films are mostly oxygen-free. We thus expect that our La/Mo multilayer mirrors are free from La oxide. These measured optical constants of La are used throughout this thesis both for simulations and for optimizations of La based multilayer coatings.

3.4.3   Simulated reflectivity of broadband and high periodic multilayer stacks

Selecting materials for attosecond multilayer optics, low absorption (thus a high penetration depth) (figure 3.9), low interface roughness (section 2.2.4.4) and a high single interface reflectivity is needed for high reflecting XUV multilayer mirrors.   The normal
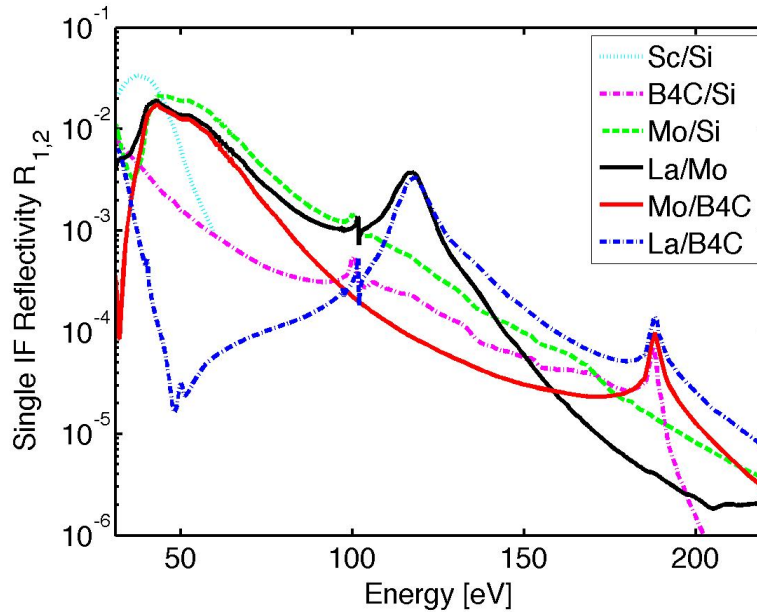
Figure 3.12: Energy dependent normal incidence single interface reflectivity (calculated from equation 2.28) of a selection of material-combinations consisting of Mo, Si, La, B_4C and Sc plotted in energy ranges where they exhibit large values.

incidence single interface reflectivity between two materials can be estimated from equation 2.28, which relates the single interface reflectivity to the distance of the optical constants in the complex plain ($R_{singleIF} \propto \delta^2 + \beta^2$). Figure 3.12 displays the single interface reflectivity of a selection of material combinations of Mo, Si, La, B_4C and Sc. Values between 10^{-2} and 10^{-1} can be reached at low XUV energies around 30 eV which drop to $\approx 10^{-5} - 10^{-4}$ at about 200 eV.

Figure 3.13 compares the maximum achievable reflectivity of periodic quarter-wave stacks for selected material-combinations in
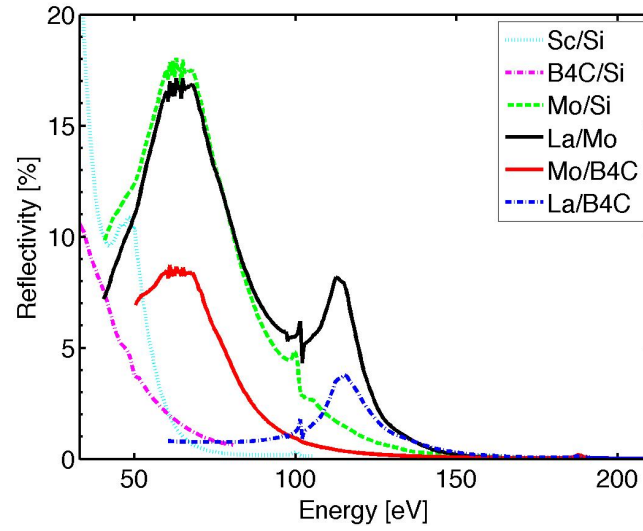
(a) N=4
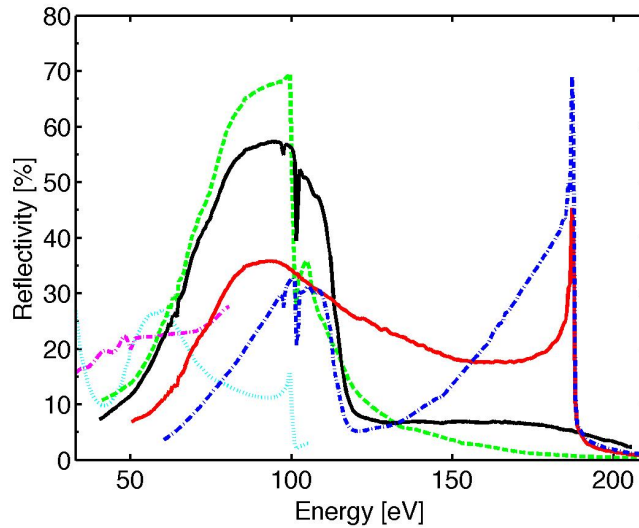
(b) N=300

Figure 3.13: Simulated maximum reflectivity for selected material combinations between 30 and 200 *eV* under near normal incidence of 5°. Panel a) shows the simulation for 4 periods only, panel b) displays the maximum reflectivity achievable for a stack with 300 periods. The simulations used the following roughness values: $\sigma_{Sc/Si} = \sigma_{Si/B_4C} = 1.3\ nm$; $\sigma_{Mo/Si} = 0.6\ nm$; $\sigma_{La/Mo} = 0.4\ nm$; $\sigma_{Mo/B_4C} = 0.5\ nm$; $\sigma_{La/B_4C} = 0.7\ nm$;

the energy range between 30 and 200*eV*. Each point corresponds to a multilayer stack with a certain period thickness. The simulations

have been performed using realistic interface roughness values, as an outcome from fabricated multilayer mirrors. While panel a) displays the result for broadband 4 period multilayer mirrors panel b) shows the simulated result for high-period ($N = 300$) stacks with saturated maximum reflectivity. When choosing multilayer materials for attosecond optics, materials with inner shell absorption edges in the spectral range of interest have to be avoided as non-linearities in the optical constants may distort the phase and thus the temporal length of a pulse upon reflection. Table 3.6 summarizes the most suitable multilayer material combinations, spectrally ordered. This table is base for realized mirrors presented later.

Table 3.6: Most suitable material combinations for maximum reflectivity of two-material mirrors between 30 and 200 eV built from Sc, Mo, Si, La, and B_4C both for high reflecting (upper rows) and for broadband (lower rows) stacks.

Energy range [eV]	30-60	60-100	100-130	130-150	150-200
high period	Si/B_4C	Mo/Si	La/Mo	Mo/B_4C	La/B_4C
2nd best	Mo/Si	La/Mo	Mo/B_4C	La/B_4C	Mo/B_4C
3rd best	Sc/Si	Mo/B_4C	Mo/Si	La/Mo	La/Mo
broadband	Sc/Si	Mo/Si	La/Mo	La/B_4C	La/B_4C
2nd best	B_4C/Si	La/Mo	La/B_4C	La/Mo	Mo/Si
3rd best	Mo/Si	Mo/B_4C	Mo/Si	Mo/Si	Mo/B_4C

The pure normal incidence reflection of ultrashort pulses requires low period, broadband mirrors. Normal incidence high period mirrors on the other hand exhibit small bandwidth and enable high spectral resolution experiments.

In off-normal incidence optics the criteria which drive the design and choice of materials are very similar although not the same. Here the larger Fresnel coefficients yield a decreased penetration depth. The number of contributing interfaces is even more decreased due to thicker layers (Bragg equation 2.29) and off-normal traveling angles. Thus, the larger the angle of incidence, the more important becomes the low absorption of the multilayer materials. When designing optics for attosecond pulse reflection, then the pulse length defines the maximum penetration depth and thus

also the tunability of aperiodic coatings decreases with the angle of incidence. All of the here presented attosecond experiments utilize multilayer optics either under near normal incidence or at $\theta = 45^o$, where appropriate designs are still possible.

3.5 Quantification of silicide formation in Mo/Si coatings

Mo/Si multilayer mirrors can be utilized both for high reflecting and broadband coatings between 50 and 100 eV (table 3.6). Such optics served the generation of single attosecond pulses from the very beginning [18] and many of the following presented mirrors contain both Mo and Si layers (ultra-broadband reflector for the generation of 80 as pulses in section 4.1.2; ternary spectral cleaning mirrors around 130 eV in section 4.4).

It has been shown in [127], [52], [51] that asymmetric silicide layers are formed in Mo/Si multilayers. As this formation consumes material, not only the index of refraction is varied along each interface; also the individual period thickness and thus the multilayer design is affected. Therefore the quantification of these interlayers is an important prerequisite for the correct modeling and realization of Mo/Si multilayer designs.

A. Aquila et al. have investigated the structural change in an aperiodic magnetron-sputtered Mo/Si multilayer by TEM imaging and XUV reflectometry [52]. Previous measurements indicated the formation of amorphous and nearly stoichiometrically pure $MoSi_2$ interlayers [164], [127]. Therefore, they assumed that per 1 nm formed silicide, 1 nm Si and 0.39 nm Mo is consumed.

A. Aquila et al. finally came up with a model, where the thickness and thus the asymmetry of the $MoSi_2$ layers depends on the individual Mo layer thicknesses. This is attributed to a phase transition in Mo from amorphous to polycrystalline at a layer thickness greater than about 2 nm. A polycrystalline Mo layer hinders the formation of a thick silicide layers on its top in contrast to the amorphous case.

In Aquila's model an $MoSi_2$ interlayer of 0.95 nm is always formed when Mo is deposited on Si. In the case of Si deposition on Mo two cases are distinguished. If the Mo layer is much thinner than 2 nm, then the $MoSi_2$ interlayer is as well about 0.95 nm thick, while it is only about 0.6 nm if underlying Mo is larger than 2 nm.

As the detailed values might depend on the deposition method and the deposition parameters, this process is investigated for ion beam sputter deposited Mo/Si multilayer stacks in more detail here. TEM cross-section images of two Mo-containing multilayer coatings produced by our IBD sputter tool confirm the occurrence of Mo in both amorphous and polycrystalline state as shown in figure 3.14. Consistent with Aquila's theory, amorphous Mo layers are found in the multilayer displayed in panel a) which only contains Mo layer thicknesses below 1.5 nm. In contrast to that, the more than 3 nm thick Mo layers in the multilayer of panel b) appear mostly polycrystalline.

In XUV reflectometry measurements of periodic Mo/Si coatings, the formation of asymmetric silicide interfaces can hardly be distinguished from a symmetric built up as both symmetric and asymmetric interfaces yield mainly a shift of the XUV central energy. It turns out, that the XUV reflectivity of an aperiodic mirror with a design of the kind shown in figure 3.15 b) is most sensitive to the silicide asymmetry. This design actually consists of three aperiodic multilayer stacks on top of each other. On a Mo/Si stack at the bottom of the stack follows a ternary $Mo/B_4C/Si$ stack, while a third Mo/B_4C stack builds the multilayer mirror top. Such a design yields higher reflectivity and will be discussed more detailed in section 4.4.

Assuming that also in ion beam sputtered Mo/Si multilayers, asymmetric silicide layers are formed, then the bottom Mo/Si stack contains two kinds of $MoSi_2$ thicknesses depending on whether Mo is deposited on top of Si or whether Si is deposited on top of Mo. In contrast to that, the middle $Mo/B_4C/Si$ stack only the thicker silicide layers, as Mo is always deposited on Si while each Mo layer is followed by $B4C$. In the top Mo/B_4C stack no $MoSi_2$
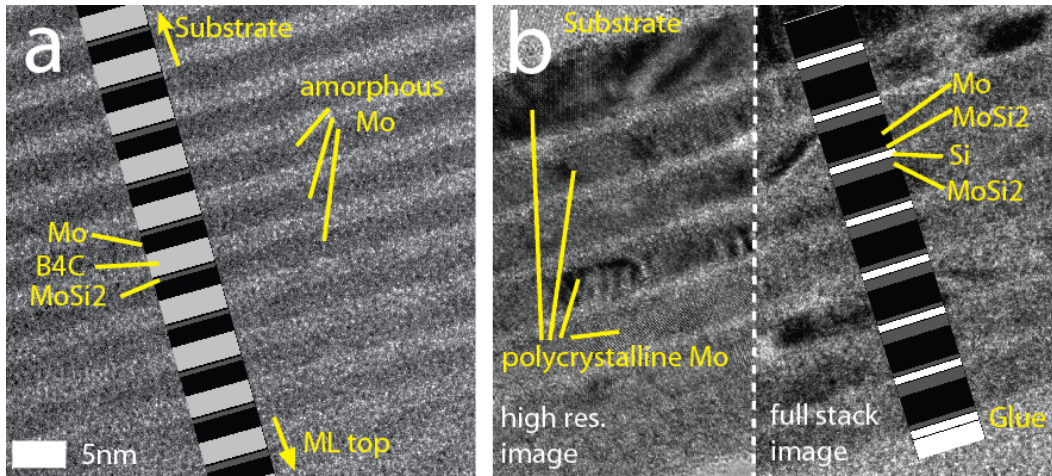
Figure 3.14: TEM images of two multilayer mirrors, both containing Mo. Panel a) Ternary $Mo/B_4C/Si$ stack with amorphous Mo layers. A complete conversion of Si to $MoSi_2$ is assumed, yielding a final design model of 100 periods of $[Mo(1.47 \ nm)/B_4C(2.28 \ nm)/MoSi_2(0.57 \ nm))]$. Panel b) shows a 8 period $\gamma = 0.55$ Mo/Si multilayer mirror originally designed for usage above 100 eV. The insets show the calculated design based on the models described in this section. The high-Z material Mo containing layers (Mo, $MoSi_2$) appear darker in the TEM images than Si and B_4C. The increased thickness of the first Mo layer in panel b) is of obscure nature and could not yet be explained.

is formed.

Figure 3.15 compares the reflectivity simulations of different Mo/Si_2 interlayer formation models with the measured reflectivity. For details please read the figure caption. Comparing the different reflectivity simulations only the asymmetric interlayer model (black solid line in panel b)) yields good agreement of both the energy of the maximum reflectivity and a correct XUV reflectivity shape. This is most noticeable at the low energy secondary reflectivity maxima in panel a). Thus the asymmetry is confirmed.

Comparing the simulated and the measured XUV reflectivity of this and other ion beam sputtered Mo/Si mirrors produced in our IBD tool, a model has been developed, which is very similar to that of Aquila et al. This model is based on the thickness consumption assuming pure $MoSi_2$ interlayers suggested above.
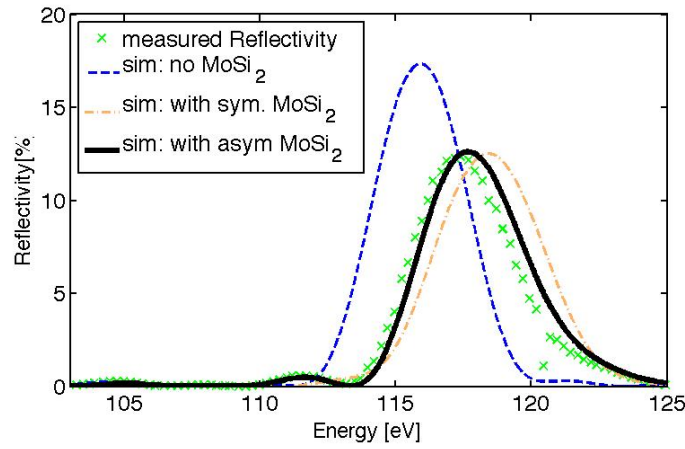
(a) Reflectivity comparison of XUV measurement and different $MoSi_2$ interlayer models
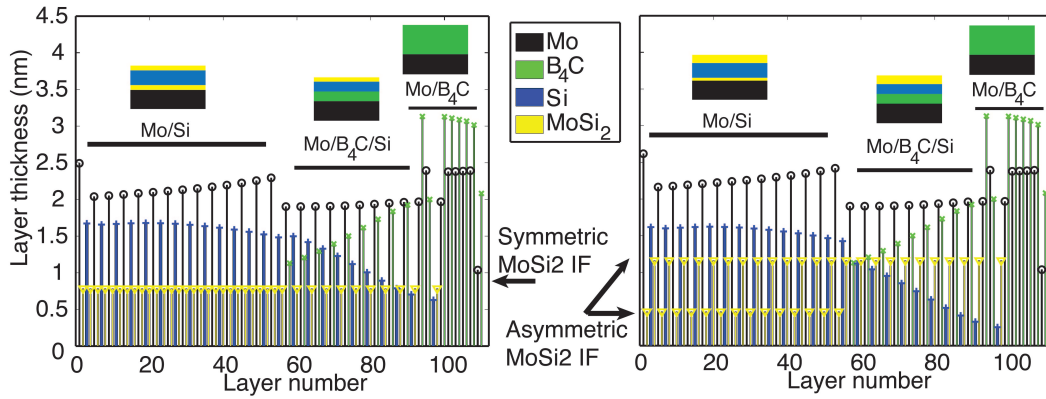
(b) Multilayer design model including (a-)symmetric $MoSi_2$ interlayers

Figure 3.15: Comparison of the XUV measurement (green stars) with three design models, once without any interface formation (bluue dashed line), once with symmetric $MoSi_2$ interfaces as displayed in panel b) (yellow dash dotted line), and once with asymmetric interfaces included resulting in the appropriate design as displayed in panel c) (black solid line).

I assume the formation of silicide layers of about $0.4 \pm 0.1\ nm$ if Si is deposited on Mo. In the case of Mo being deposited on Si $1.1 \pm 0.1\ nm\ MoSi_2$ can be quantized.

The correctness of the model is finally confirmed by comparing the XUV and the XRR measurement of a standard periodic 25 period Mo/Si stack with the appropriate simulations (figure 3.16). Both the XUV reflectivity and the Bragg peak positions and the

(a) XUV (b) XRR
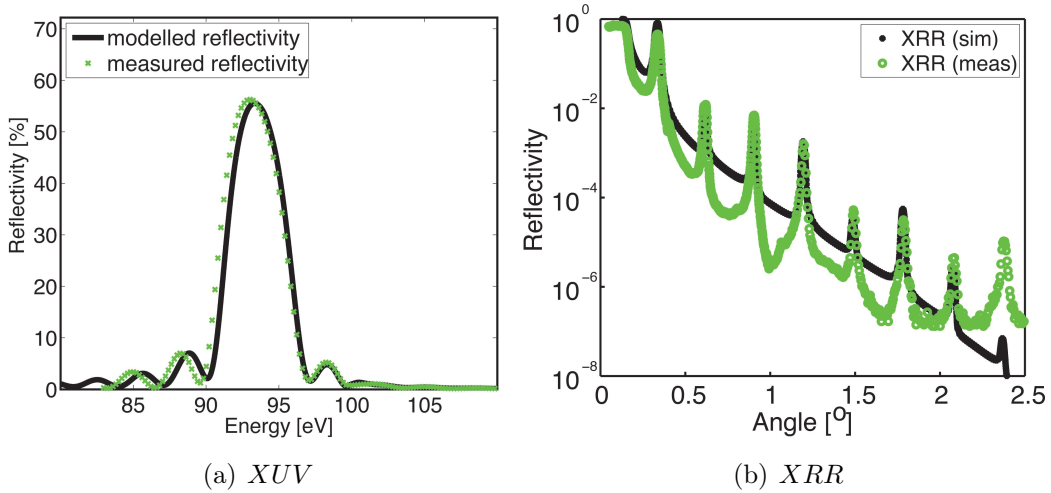
Figure 3.16: Comparison of XUV reflectivity (panel a)) and XRR simulations (black) and measurement (green) for a standard 25 period Mo/Si coating (bandwidth $\approx 4.3\ eV$).

intensity in the XRR measurement reveal good agreement between simulation and measurement when the asymmetric model is used.

We retrieve a Nevot-Croce roughness of about $\sigma = 0.6\ nm$ in XUV reflectivity measurements ($R_{max} = 55\ \%$ at $93\ eV$) and about $0.35\ nm$ in the XRR data. As discussed earlier, there are several possible reasons for this deviation, as the different "average measurement depth", impurities or a small bending of the measured sample.

From other XUV measurements and the TEM cross sections, the critical amorphous to polycrystalline Mo transition thickness could be estimated to about 1.7-1.9 nm. If the underlying Mo layer is smaller than that value $MoSi_2$ interlayers of also $1.1nm$ has been assumed.

The presented final model enabled the correct implementation of aperiodic "spectral cleaning" multilayer coatings, which contain both very thin ($< 1.5\ nm$) and thick ($> 2\ nm$) Mo layers (section 4.4). A signal to noise ratio of more than 50 could be achieved and was only possible due to a proper compensation of thickness loss at Mo/Si interfaces.

3.6   Conversion of mirror design to deposition time

The high stability of ion beam deposition allows for a temporal control of the layer thicknesses. Thus each design has to be converted into sputter-times. In the previous section the formation of $MoSi_2$ interlayers in Mo/Si stacks has been investigated and confirmed the importance of including even small variations from the designs into the simulation (figure 3.15).

We have performed comparison height measurements on "bulk-like" samples and multilayer coatings to set up models for other material combinations. An interface loss of 0.1 nm was found at each La/B_4C and Mo/La interface and about 0.4 nm at each Mo/B_4C or Si/B_4C interface. In the following simulations, only the $MoSi_2$ interlayers are implemented as extra layers with their appropriate index of refraction. It turned out to be sufficient to compensate the thickness loss of other material combinations by symmetrically increasing the sputter times correspondingly.

In addition to that a sputter time offset of ≈ 0.04 s has been identified, most probably due to shutter closing times and small uncertainties in the switching process of the ion beam. This variation can as well be compensated by adapted deposition times.

All multilayer simulations and designs presented in the following include upper information. The correct calibration of the rates, the validity of the interface model, the benefit from the shaper and the additional factor due to the sample height is confirmed by the good agreement between simulated and measured XUV and XRR measurements in periodic and aperiodic multilayer mirrors as presented in the following chapter.

Chapter 4

Applications of multilayer mirrors for *as* pulse shaping

In this section different concepts of periodic and aperiodic multilayer mirrors for attosecond pulse-shaping are presented and experimentally tested in attosecond experiments. In section 4.1 the question on attosecond optics for the reflection of pulses of minimum length is addressed. The design and the XUV reflectivity measurements of a broadband multilayer mirror for a central energy of 45 eV is shown. This mirror supports the reflection of sub-2-cycle long attosecond pulses (subsection 4.1.1). In subsection 4.1.2 the generation of the shortest ever measured attosecond pulses of no more than 80 as centred at 75 eV is presented, based on nearly single cycle HH driving laser pulses as well as an ultra-broadband (32 eV) multilayer mirror/Zr-filter compressor.

The following sections present the first isolated attosecond XUV pulses above 100 eV. In section 4.2 the novel material combination of La and Mo is introduced which is especially suited for the generation of attosecond pulses between 80 and 130 eV. After analyzing its structural properties in XRR and XUV reflectivity measurements, the multilayer material combination La/Mo is tested for its shelf-lifetime stability in air ambient. The first experimental realization of an attosecond streaking experiment using La/Mo multilayer reflectors at a central energy of 105 eV is presented. Effects of the La $N_{2,3}$ absorption edges around 100 eV on the pulse length are investigated.

Chapter 2 has proven the importance of controlling the phase of an attosecond pulse. Absolute control of the attochirp above 100 eV by means of a set of three multilayer mirrors has been realized in a novel 45° XUV pump IR probe set-up and is presented in section 4.3. To the end of this section, two normal incidence La/Mo mirror designs are presented together with XUV reflectivity measurements and suggested for the generation of chirped attosecond pulses at 105 eV in a normal incidence geometry.

In section 4.4 the concept of spectral cleaning mirrors is introduced and proven as appropriate concept for the generation of attosecond pulses in spectral regions without suitable filter materials and for attosecond experiments which require very high spectral resolution of a few ($\approx$1-5) eV only. After analyzing the benefits of ternary XUV multilayer designs, the concept of spectral cleaning is implemented in ternary aperiodic $Mo/B_4C/Si$ multilayer mirrors and tested in attosecond pump-probe streaking experiments.

Finally, in section 4.5 La/B_4C multilayer mirrors are presented as near future normal incidence high energy attosecond optics between 150 and 200 eV.

4.1   Ultrashort pulse generation

Ever shorter isolated attosecond pulses enable experimental access of absolute or relative timing of electronic processes with never before achieved temporal resolution [165], [95], [2]. As has been analyzed in detail in section 2, the filtering, reflection and shaping of attosecond pulses requires phase-correct broadband optics. Especially in normal incidence set-ups, the question of the shortest possible attosecond pulses is thus directly connected to the availability of appropriate optics, namely XUV multilayer mirrors and filters.

One can estimate the bandwidth ΔE of an N-period multilayer stack with central energy E from equation 2.40: $\Delta E/E = 1/N$. An interference coating consists of at least two periods ($N \geq 2$), thus in principle, the maximum bandwidth of a periodic multilayer

mirror is about half its central energy. Higher central energies relax the constraints on the bandwidth of optics and thus enable shorter reflected pulses but suffer usually from lower reflectivity as has been analyzed in section 3.4.

In the following, two ultrabroadband attosecond multilayer mirrors are presented. The first one is a broadband normal incidence mirror, designed for a central energy of $\approx 45\ eV$ which exhibits a bandwidth, that even exceeds the natural limit given by the upper relation (equation 2.40). Next, experimental results on the optics and the generation of the ever shortest isolated attosecond pulses of $80 \pm 5\ as$ are presented.

4.1.1 A normal incidence broadband 30-60 eV mirror

Many attosecond experiments are performed in the spectral range between 30 and 60 eV, which is easy to access with HH sources [62], [63], [166]. The shortest attosecond pulses in this spectral range could be generated by *polarization gating*. Sansone et al. realized 130 as long pulses around 40 eV [63]. This and other experiments may benefit from broadband normal-incidence XUV optics suitable for attosecond beam guidance and focusing.

An aperiodic broadband mirror reflecting between 35 and 50 eV with a reflectivity up to 20 % has been designed and published by Morlens et al. [56].

The here presented periodic Si/Sc mirror, centred at nearly the same central energy of $\approx 40\ eV$ exceeds the bandwidth of Morlens' mirror by far. Its design is chosen such, that the high single interface reflectivity of Si and Sc is extended by an appropriate quarter-wave design to a bandwidth of more than 20 eV.

Until now, Sc/Si multilayers have mainly been used at energies between 25 and 35 eV [167] just below the $Sc\ M_{2,3}$ (table 3.4). Above this energy, both Sc and Si are highly absorbing, and the number of contributing periods in Si/Sc multilayers is very limited. The normal incidence reflectivity saturates between 35 and 45 eV for only ≈ 5 periods. The relatively high reflectivity between 5-7 % is mostly independent from the mirror design due
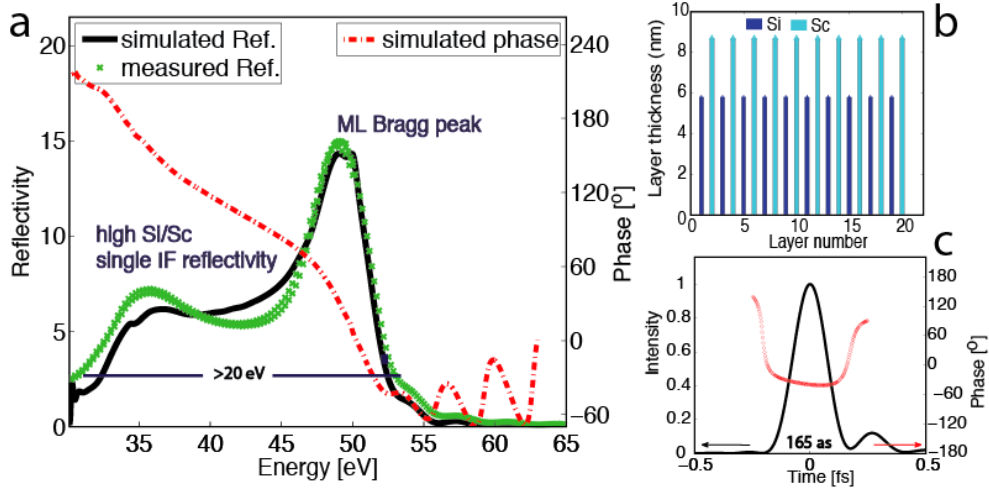
Figure 4.1: Broadband normal incidence XUV multilayer mirror between 30 and 55 eV. Panel a): simulated (black) and measured (green) XUV reflectivity and spectral phase (red dash-dotted line). A $\sigma = 1.3\ nm$ has been used in the simulation. Panel b) shows the appropriate design of the 10 period, $d = 14\ nm$, $\gamma = 0.4$ Si/Sc stack. Panel c): Temporal structure of the mirror calculated as the Fourier transform of its spectral shape: It supports the reflection of 165 as sub-2 cycle XUV pulses.

to a high single interface reflectivity of about 2%. This property has been utilized for the design of the following ultrabroadband mirror. Its design is chosen such, that the already high Si,Sc reflectivity is extended on the high energy side for a larger overall bandwidth. A 10 period Sc/Si coating with a period thickness of 14 nm (for a central energy of $\approx 50\ eV$) has been chosen (figure 4.1 b)). Its designed and measured reflectivity is plotted together with the calculated phase in figure 4.1 a). The measured XUV reflectivity confirms a successful implementation, a bandwidth of more than 20 eV and a reflectivity between 5 and 15 %.

Simulations show, that this mirror is capable to support the reflection of Fourier limited 165 as long pulses what corresponds to only 1.7 XUV field oscillations at 42 eV central energy (figure 4.1 c)). This mirror thus allows for the phase correct reflection of sub-2 cycle XUV pulses and is therefore at the possible duration limit at this energy.

4.1.2 The generation of 80 as XUV pulses

Shorter pulses require even more bandwidth and thus necessarily higher central energies. The development of ultra-broad HH cut-off spectra with sufficiently high photon flux in the spectral range between 60 and 100 eV and the availability of appropriate thin metal filters and broadband high-refectivity multilayer optics suggest this energy range for the generation of ever shorter ultrashort pulses.

The following experiment has been performed at the $AS1$ beam-line of the MPQ. The experimental set-up is plotted in figure 2.19, using the combination of a multilayer "double mirror" at near normal incidence $\theta \approx 5^o$ and a thin metal filter as bandpass and pulse shaping elements for the filtering and compression of isolated attosecond pulses. This resulted in the generation of light flashes of no more than 80 as (section 4.1.2) and has been published by E. Goulielmakis et al. in *Science* [19] ([168], [169]).

4.1.2.1 The Optics

The HH generated XUV cut-off spectrum at about 100 eV matches the high reflectivity spectral band of Mo/Si multilayer mirrors (table 3.6); this material combination has thus been chosen. The generation of 80 as long pulses requires at least 25 eV ($FWHM$) bandwidth[1] and is given by a multiplication of both the spectrum of the optics and the HH spectrum, from which the single pulse is being filtered.

As will be presented in the following paragraph, this requires a HHG spectrum which exceed the chirp-free cut-off region, ranging to the lower energy plateau region which is known to be positively chirped. This phase behavior (positive chirp at low energies, negligible chirp at high energies) exactly opposes that of a thin Zr filter, used in this experimental set-up anyway to filter the laser light from the XUV propagation path. As the filter indispensably compensates most of the HHG chirp, a chirp-less but broadband

---

[1]A Gaussian spectrum has been assumed.
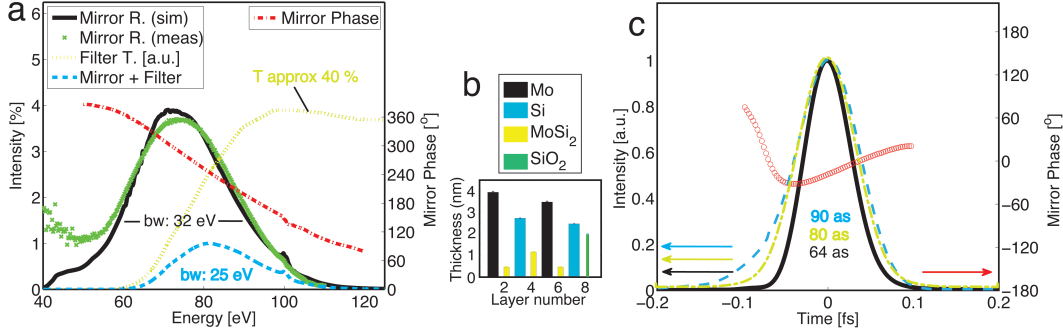
Figure 4.2: Panel a): Simulated (black line) and measured (green crosses) reflectivity of a 32 *eV* (*FWHM*) bandwidth flat phase (red dash dotted line) multilayer mirror (design plotted in panel b)), revealing a measured 3.6% reflectivity centred at 70 *eV*. Together with a 300 *nm* thick *Zr* filter (yellow dotted line) it functions as a 25 *eV* broad bandpass and compressor (blue dashed line) for the generation of 80 *as* *XUV* pulses. Panel c) shows the simulated 64 *as* long pulse (black line) and the temporal phase (red circles) of a pulse supported by the mirror upon reflection as an outcome of Fourier transforming the mirrors spectrum. The blue dashed line shows the temporal structure of the bandpass (mirror + filter), resulting in an 90 *as* long pulse, compared to its Fourier limit (light green dash dotted line) of 80 *as*.

attosecond mirror is required. The penetration depth and thus the maximum number of usable bi-layers is limited by the attosecond pulse-length (equation 2.41). A four-layer Mo/Si XUV coating centred at 70 *eV*, with a bandwidth of 32 *eV* (*FWHM*) has been designed for the coating of the inner part of the of the double mirror (figure 4.2 b)). Its reflectivity has been measured (green stars in panel a)) and is in good agreement with simulations.

Figure 4.2 concludes the spectral (panel a)) and the temporal (panel c)) characteristics of this bandpass. Simulations reveal, that the mirror alone supports the reflection of nearly Fourier-limited pulses of 64 *as* (Fourier limit of the mirror: 63 *as*) calculated from the simulated spectrum (black line in figure 4.2 c)) and the phase (red dash-dotted line). The effective bandpass bandwidth is experimentally limited by the transmission of the Zr filter which is required for suppression of the IR laser light and to tune the spectral phase. Different filter thicknesses (150, 300 and 450 *nm*)

allow for some tunability of the GDD for the sake of reducing the effective bandwidth (the peak of the multiplied spectrum, plotted by the blue dashed line is shifted towards higher energies). It turned out that the combination of the mirror with a 300 nm Zr filter (yellow line, figure 4.2 a)) compresses the incoming pulse to almost its Fourier limit.

The goodness of the perfect interplay between the spectral phase of the bandpass and that of the HH source becomes more obvious, when one compares the temporal structure of the bandpass (panel c), blue dashed line) with its Fourier limit (light green dash-dotted line). The bandpass has a Fourier limit of 80 as, its temporal structure reveals 90 as including the phase (pulse broadening can be almost completely related to the phase of the filter). The final pulse-length of 80 as thus is at exactly the Fourier-limit of the bandpass. Please note here, that the final pulse is a convolution of the bandpass and the incoming pulse. The HH intensity decreases at higher energies in the cut-off range and yields a slight down shift and a slight broadening of the bandpass spectrum.

4.1.2.2 CEP dependency

Sub- 1.5 cycle (3.3 fs) long phase stabilized laser pulses with a central wavelength of ≈ 0.72 μm could be generated reproducibly and stable and have been used for the generation of XUV HH radiation in Ne. For such short pulses the intensity of the central half field oscillation exceeds by far that of all other laser half cycles.

The generated attosecond pulses and the driving laser pulses could utilize attosecond streaking in Ne, revealing both the generated XUV spectrum (within the spectral window of the bandpass) and the CE phase of the driving laser. Direct and simultaneous access on these two quantities and the fact that photoionization is confined to a single wave cycle, results in observables (such as high-harmonic photons and electrons emitted by above-threshold ionization) that can now be related to several distinguishable sub-cycle ionization events and subsequent trajectories. Their timing with respect to the driving field, the laser field strength and their

temporal evolution is accurately known [17]. These circumstances provide ideal conditions for testing models of strong-field control of electron motion and electron-electron interactions.
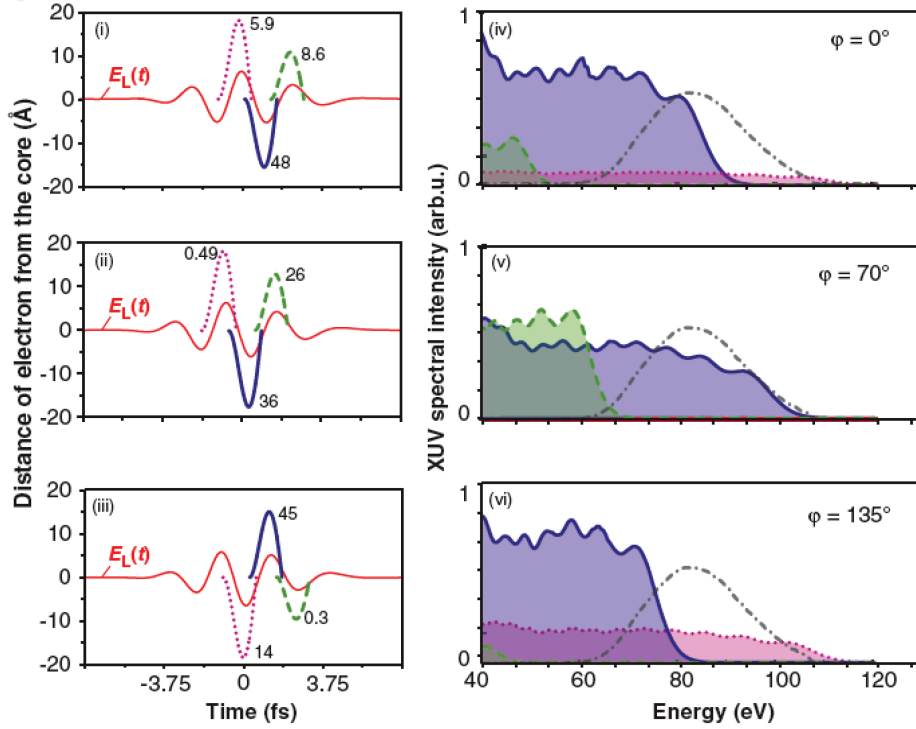
Figure 4.3: Simulated XUV emission spectrum (right panels) from Ne atoms ionized by a linearly polarized, 3.3 fs long laser pulse of a wavelength of 720 nm in dependency on the laser CE phase and the classical electron trajectories of maximum energy (taken from [19]). For a more detailed description see text.

Simulations show, that the generated XUV spectra originating from the individual re-collisions, differ from each other by tens of eV cut-off energy, due to the contrast between the central and the neighboring half cycle field amplitudes of the laser. Beside that, their intensity substantially depends on the ionization probability and hence the squared modulus of the amplitude of the electron wave-packets launched, yielding to orders of magnitude different intensities as a consequence of the single-cycle nature of the driving field.

Figure 4.3 displays the simulated resulting XUV emission spectra (right panels) in dependency of the CEP-dependent laser field

(red lines, left panels) and the classical trajectories of maximum return energy (colored lines, left panels) (correspondence established by colors and line style). The ionization probability is given by the numbers in the left panels, in units of 10^{-4}. The grey dash-dotted line depicts the bandpass spectrum. For a more detailed description on the theory please read [19].

It is common understanding (and true for mediate long driving pulse lengths), that a cosine-like CE phase $\phi \approx 17^o$ is best suited for ultrashort pulse generation, as the high energy XUV spectrum generated by the center laser oscillation exceeds the maximum energy of neighboring oscillations most. For a sub-1.5 cycle laser pulse with a nearly sine-like CE phase of 70°, the intensity of XUV radiation generated by the "pink" oscillation is highly suppressed due to a (by two orders of magnitude) lower ionization probability, yielding an ultra-broad XUV spectrum that stamps from almost one single attosecond pulse. Therefore the "pink dotted line" emission in figure 4.3 panel v) is not visible with respect to that resulting in the purple "solid-line" emission. Tuning the CEP to this particular region, an unmodulated XUV spectrum extending from about 65 to $110eV$ could be generated, extending by far the cutoff range at lower energies. The consecutive optics, namely the attosecond double mirror and a 300 nm Zr filter function as bandpass and pulse compressor in perfect interplay with the source as described above.

4.1.2.3 Attosecond streaking

The appropriate spectrograph (A) together with its $FROG$ retrieval (B) and the reconstructed attosecond pulse in the temporal (C) and the spectral (D) domain is plotted in figure 4.4. The final reconstructed pulse-length of $80 \pm 5as$ could be retrieved with a very little left over chirp of about $1.5 \pm 0.2 \cdot 10^3 \ as^2$. The fringes in the spectral domain result from an accompanying small satellite pulse as shown in figure 4.3, panel v). Theoretical calculations as well as quantitative analyses of the π shifted overlaying additional streaking curve prognoses a satellite pulse contribution to the
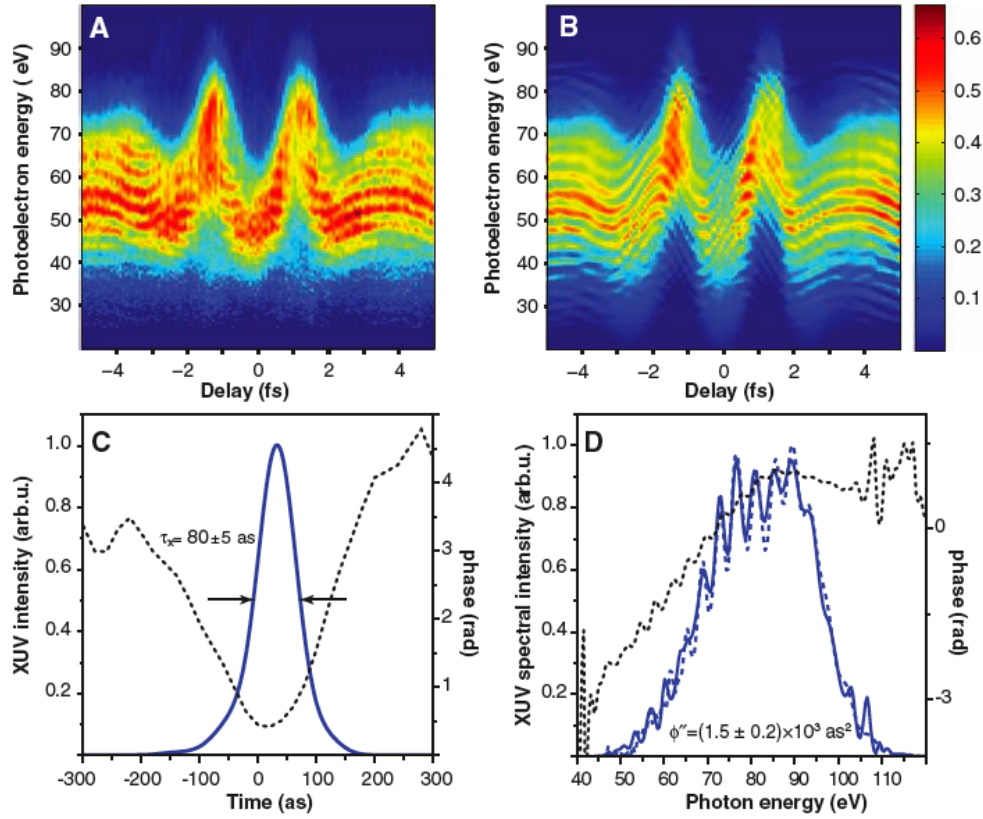
Figure 4.4: Sub-100 *as XUV* pulse retrieval (taken from [19]). A) Measured spectrogram compiled from 126 energy spectra of photoelectrons launched by an *XUV* pulse with a bandwidth of ≈ 28 *eV* (*FWHM*) and recorded at delay settings increased in steps of 80 *as*. The high flux of the *XUV* source allows this spectrogram to be recorded within some 30 minutes. B) *ATR* spectrogram reconstructed by *FROG* algorithm. The lower panels display the retrieved pulse both in the temporal (C) and in the spectral (D) domain. Both the photoelectron spectrum in the absence of the *NIR* streaking field (solid line) and and the *FROG* retrieved spectrum (dashed line) are displayed in D).

spectrum of about 7%. A satellite contribution of only 1% in the spectrum is retrieved by the attosecond *FROG*. This discrepancy results in slightly smaller fringes in the retrieval than expected.

These attosecond pulses could be used in 2010 to track the motion of valence electrons in transient absorption measurements for the first time [106].

4.2 *La/Mo* multilayer mirrors for attosecond pulse generation between 80 and 130 *eV*

Attosecond optics for experiments at central energies above the Si, $L_{2,3}$ edge at 100 eV require different material combinations than Mo and Si.

In this section a novel multilayer material combination based on La and Mo nano-layers for both broadband and highly reflecting multilayer mirrors in an energy range between 80 and 130 eV is presented. Simulation and design of these multilayers is based on the improved set of optical constants, which has been recorded by XUV/soft-X-ray absorption measurements and which has been presented in section 3.4.2.

The ability to precisely simulate and realize (a)periodic La/Mo stacks is demonstrated by X-ray and XUV reflectivity characterization. The combination of La/Mo multilayers with the third material B_4C, adds yet more degrees of freedom for mirror design targets such as high reflectivity, a tailored phase or a special spectral reflectivity shape. La/Mo multilayers exhibit low interface roughness values σ. The mirrors consist of nontoxic materials -what cannot be taken for granted for multilayer materials suitable in that energy range- ensuring an easy experimental usage. Their stability against ambient air conditions is tested. Finally, lanthanum-molybdenum mirrors have been applied for single attosecond pulse generation from high harmonic cut-off spectra above 100 eV. Isolated 200 attosecond long pulses have been measured by XUV-pump/IR-probe streaking experiments and characterized by using $FROG/CRAB$ analysis.

The appropriate attosecond experiments have been performed at the $AS1$ beam-line at the MPQ; the experimental set-up is plotted in figure 2.19.

Most of these results have been published in 2011 in *New Journal of Physics* (Hofstetter et al.) [170].

XUV reflectivity simulations

So far, high reflecting multilayer mirrors between 100 and 120 eV have either been based on the toxic element beryllium (Be) with experimental normal incidence reflectivity up to 70% [128], [36], [171] or on yttrium (Y) [172] and strontium (Sr) [129] for which reflectivity of about 45% was achieved. The latter was measured for a 100 bi-layer stack, where the reflectivity measurement was performed under vacuum condition due to the high reactivity of Sr to air or water vapor. Standard Mo/Si multilayer mirrors [173], [127] that are used above the $Si\ L_{2,3}$- absorption edge, suffer both from abrupt changes in the optical constants between 100 and 115 eV and from the increased absorption of Si, excluding Mo/Si multilayers as a candidate in this energy range.

Figure 4.5 compares the simulated maximum achievable normal incidence peak reflectivity of periodic multilayer stacks built from several material combinations that have been used in the energy range between 80 and 150 eV. Each point in these curves corresponds to a specific multilayer stack, where the thickness of each layer is equal to a quarter of a wavelength ($\gamma = 0.5$). For the La/Mo stack simulation, an average roughness of $\sigma = 0.4\ nm$ has been assumed as estimated from experimental data shown in the following. All other simulations have been performed with realistic average roughness values between 0.55 nm and 0.8 nm as retrieved from the literature. Information on the used roughness measures and assignment to the publications can be found in the figure caption.

Figure 4.5 a) depicts the result from reflectivity simulations for broadband multilayer coatings with 8 periods ($\Delta E/E \approx 1/8$). The maximum achievable reflectivity of the few bilayer La/Mo multilayer mirrors exceeds that of Mo/Be, Mo/Sr, Mo/Y or Mo/Si, what marks them as most favorable for attosecond optics in this spectral range. This changes in the case of high-periodic multilayer mirrors in figure 4.5 b). The chosen period number of $N = 100$ ensures saturated maximum reflectivity R_∞ of all material combi-
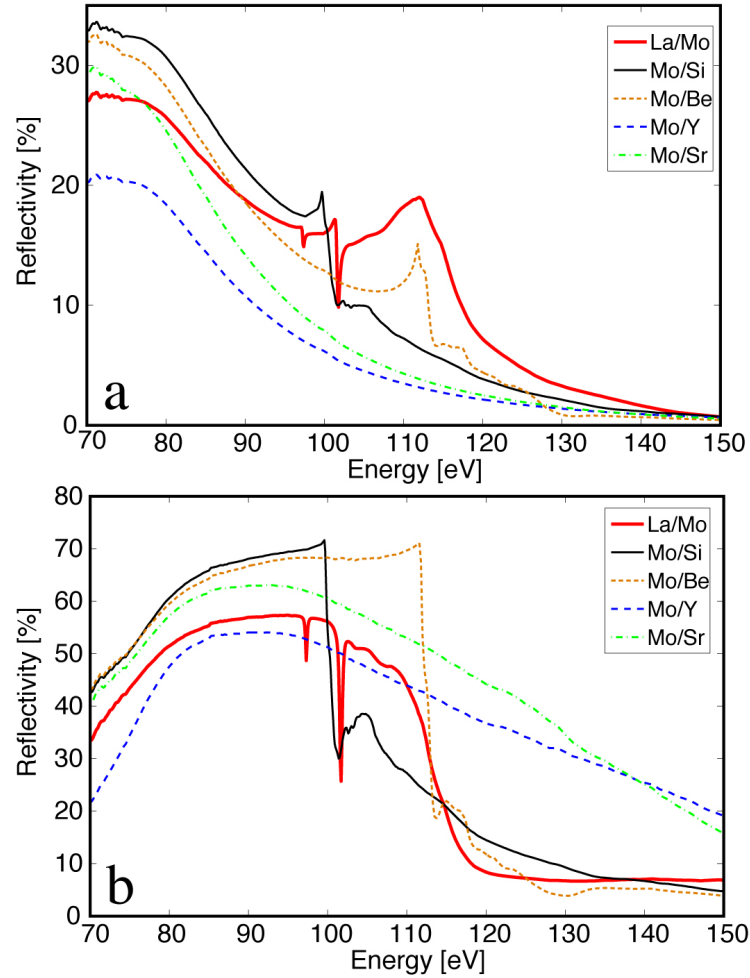
Figure 4.5: Simulated maximum reflectivity of quarter-wave multilayer stacks from different materials versus photon energy between 70 and 150 *eV*. Both broadband (panel a): *N*=8) and high reflective (panel b): *N*=100) bi-layer stack coating have been calculated. All simulations have been performed with realistic average Nevot-Croce roughness values as retrieved from existing high period multilayer mirrors. We use $\sigma(Mo/Si) = 0.6$ *nm* [173] (solid thin black line), $\sigma(Mo/Be) = 0.55$ *nm* [128] (dotted orange line), $\sigma(Mo/Y) = 0.6$ *nm* [172] (dash-dotted blue line) and $\sigma(Mo/Sr) = 0.8$ *nm* [171] (dashed green line). The roughness for our *La/Mo* stacks (solid thick red) is assumed to be 0.4 *nm*.

nations. Around 110 *eV* the maximum achievable reflectivity of a *La/Mo* multilayer is about 25 % lower than that of a *Mo/Be* stack in the large period case.

One reason for that is the larger Fresnel reflectivity and the

lower roughness of La and Mo compared to e.g. Mo and Be. On the other hand also the XUV absorption in La is larger yielding a lower XUV penetration depth. At 110 eV La/Mo multilayers reveal reflectivity saturation (95% of R_∞) for only 25 periods, while many more bilayers may contribute to the simulated maximum reflectivity for other material combinations (e.g. more than 43 periods for Mo/Be). This is why the La/Mo 8-bilayer stack outperforms the other material combinations while it is not exhibiting the highest reflectivity for the 100-bilayer stack.

Experimental development and characterization of La/Mo multilayer mirrors

In this section experimental results on high-period La/Mo stacks are presented. XRR measurements with an $Mo\ K_\alpha$ X-ray source have been performed for a 36 period Mo/La stack capped with 3nm B_4C to suppress oxidation. Figure 4.6 shows the result of
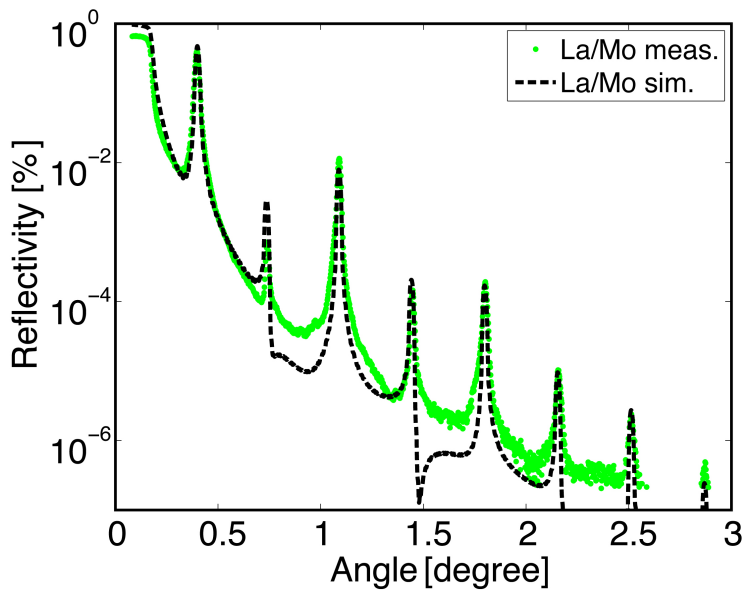
Figure 4.6: Comparison of a $Mo - K_\alpha$ ($\lambda = 0.07\ nm$) XRR measurement (green line) and its corresponding fit (black dashed line) for a high reflectivity 36 bilayer Mo/La mirror ($d = 5.72\ nm$, $\gamma = 0.47$, $\sigma = 0.3\ nm$, 3 nm B_4C capping layer). This mirror is referred to as mirror "A" in the following.

this measurement (green curve) together with a simulation (black

dashed line). The measurement fit reveals a bilayer thickness d of 5.72 *nm* and $\gamma = 0.47$ in a good agreement with the designed $d = 5.72$ *nm* and $\gamma = 0.45$. The Nevot-Croce roughness could be estimated to be 0.3 *nm*. Both the finite source angle and the detector acceptance angle have been taken into account in the simulation. This mirror is assigned as mirror "A" in the following.
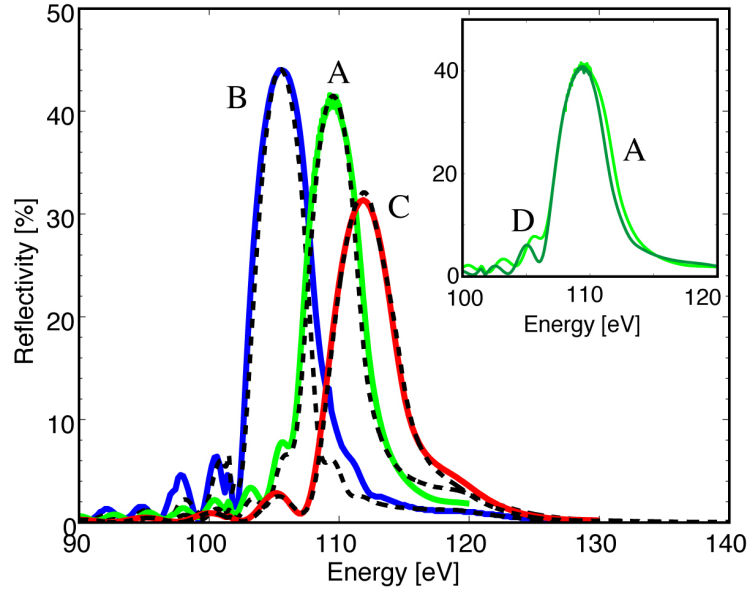
Figure 4.7: *XUV* measurements (solid colored lines) of different high-periodic *La/Mo* mirrors, together with their simulated reflectivity (black dotted lines). For more information, see text.

Figure 4.7 shows the result of *XUV* measurements for four different high reflectivity *La/Mo* mirrors (colored curves) centered at different central photon energies between 100 and 115 *eV* together with corresponding reflectivity simulations (black dashed lines). Mirror "A" (light green) is the 36 period ($R_{sim} > 99\% R_\infty$) stack characterized by XRR in figure 4.6 (see caption figure 4.6 for design details), mirror "B" (blue) is a 30 period ($R_{sim} > 99\% R_\infty$) *Mo/La* mirror stack with $\gamma = 0.55$ centered at 105 *eV* (capping 5 *nm*). Mirror "C" (red) has 20 bilayers ($R_{sim} \approx 90\% R_\infty$), a period of 5.61 *nm* and $\gamma = 0.55$ and contains 0.6 nm B_4C inter-diffusion layers as well as a 3 *nm* B_4C capping layer. We find a maximum reflectivity of 41.5% at 109 *eV* for mirror "A" and 31.5% at 112

eV for mirror "C". For stacks centered at slightly lower photon energies, even higher reflectivity of more than 44 % (mirror "B") has been measured and supported by corresponding simulations.

La/Mo multilayer stacks have been produced with and without passivating B_4C interface layers between the reactive materials La and Mo. The small inset in figure 4.7 compares mirror "A" with an identical multilayer stack "D" (same d, same γ, same N) that contains thin 1 nm B_4C interlayers. We could not find a significant effect of these B_4C interlayers on the experimental reflectivity curves, however thin (1 nm or less) passivating B_4C interlayers are used in the following stacks for possibly higher thermal and long term stability.

Nearly perfect agreement between the measurement and the simulations is revealed using the new optical constants of La. The XUV measurements further confirm the very low average roughness. We deduce an XUV roughness of only 0.4 nm in the case of pure La/Mo multilayer stacks and about 0.6 nm, when the mirrors contain B_4C barrier-layers. This value appears slightly higher than the 0.3 nm, which was extracted from XRR simulations (figure 4.6). This deviation could originate from the different penetration depth in both measurements.

The remarkable agreement between the XUV measurement of mirror "A" and the simulation performed with parameters extracted from the XRR simulation (figure 4.7) indicates a correct characterization of the system.

Shelf lifetime test of an aperiodic, chirped La/Mo mirror

La is a highly reactive material and tends to oxidize within a short amount of time. To examine the degradation of the multilayer reflectivity over time especially when stored at ambient air conditions, we have measured the long-term reflectivity stability of an aperiodic La/Mo mirror. This mirror is out of a set of normal incidence aperiodic chirped La/Mo multilayer mirrors which will be presented at the end of section 4.3.

Aperiodic mirrors are very suitable for testing the stability of a

specific material combination, as they are more sensitive to layer compression, layer expansion, and inner layer phase-transitions [52] due to the very different layer thicknesses and therefore less-stable designs. The aperiodic mirror chosen here contains *La* layer thicknesses between 1.6 and 16 *nm*, *Mo* layers between 2.1 and 4.8 *nm*, and B_4C layer thicknesses between 1 and 10 *nm* (figure 4.2 b)).
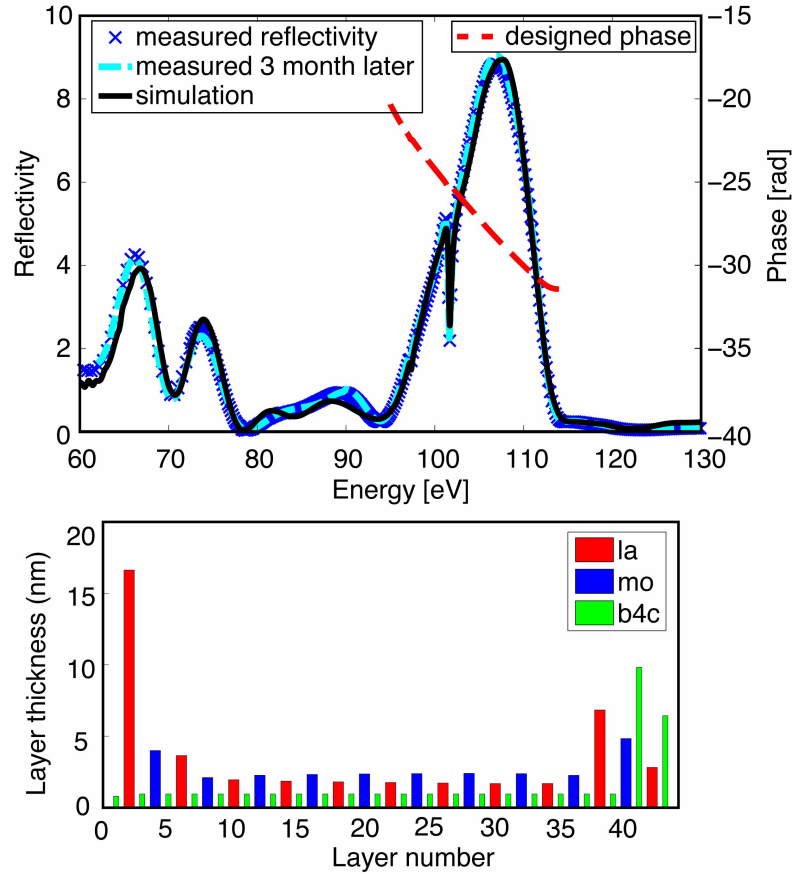
Figure 4.8: Shelf lifetime test of an aperiodic chirped mirror. Simulated reflectivity (black solid line) and phase (red dashed line) together with the measured XUV reflectivity (blue/ cyan plots) for an aperiodic $La/Mo/B_4C$ stack. The blue crosses depict the result of the *XUV* measurement right after sealing in nitrogen environment, while the dashed cyan line shows the outcome of a measurement of the same sample after air exposure over three months. The lower panel shows the appropriate aperiodic design.

After deposition, the sample has been sealed under nitrogen water-free environment and then brought into the reflectivity measurement chamber keeping transition times as short as possible.

A second measurement was performed three months later after storage under ambient humidity, pressures, and room temperature between the measurements. The mirror has not been irradiated by XUV/X-ray light, except for the two reflectivity measurements.

Figure 4.2 shows an excellent agreement of both measurements with the designed reflectivity. The average Nevot-Croce roughness could be estimated to about 0.5 nm in good agreement with the earlier performed high period sample fits from figure 4.6 and 4.7. No noticeable change in the XUV reflectivity could be observed. In conclusion, it is found, that this material combination allows for a broad tunability in the design of mirrors above 100 eV and enables the production of also long-term stable aperiodic mirrors.

Broadband La/Mo mirrors for attosecond pulse generation across an absorption edge

One can see from figure 3.9 that the effect of an absorption edge on the optical constants decreases with the sub-shell order. While K and L edges (as in the case of Si at $100eV$ or B at $188eV$) lead to jumps in both the real an the imaginary part of the index of refraction, (M), N and O edges as in La, Mo or Sc either result in very tiny peaks or slowly -varying optical constants. In attosecond optics, one has to avoid inner shell (K, L) absorption edges in the spectral region of interest as these can destroy the phase of an attosecond pulse and thus its temporal structure. Here the effect of the La $N_{4,5}$ absorption edges around 100 eV visible also in the simulations of figure 4.5 on the temporal shape of an attosecond pulse is investigated. A La/Mo coated "double mirror" has been designed and fabricated for the generation of isolated attosecond pulses and their follow-up characterization via electron streaking in neon. The aim of this particular experiment was to generate nearly Fourier limited 200 as pulses with a central energy around 109 eV in the cut-off part of the HH generation spectrum in neon gas. This mirror has been used to probe the dynamics of photo-ionization of the s and the p sub-shell in Ne [3].

A periodic La/Mo design with $N = 8$, $\gamma = 0.47$, $d = 6.05$
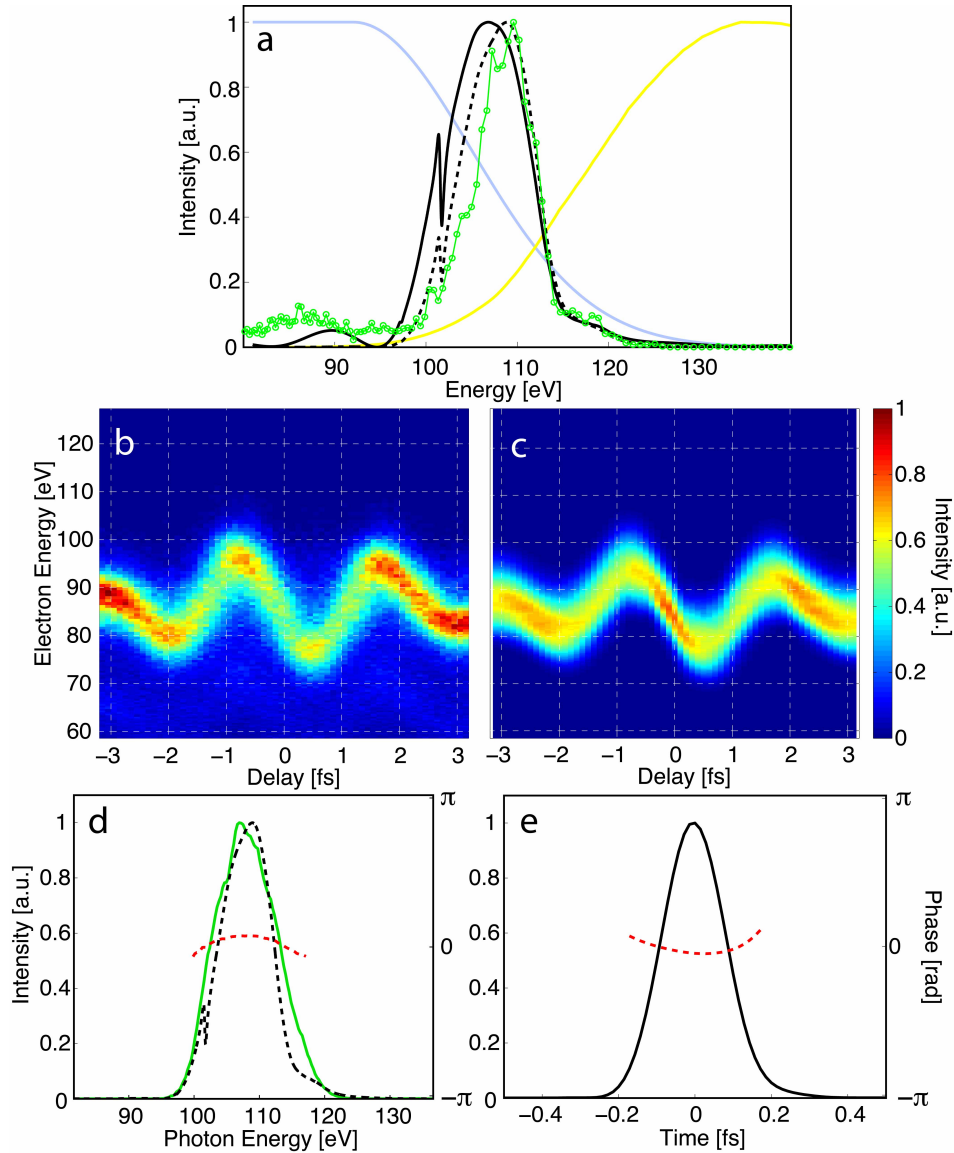
Figure 4.9: Broadband *La/Mo* mirror for attosecond pulse generation. Panel a): Comparison of the photoelectron spectrum in the absence of the laser *IR* streaking field (green line) and the calculated *XUV* spectrum (black dashed line) as a multiplication of the mirror reflectivity (solid black line), the filter transmission (yellow curve) and an analytical *HH* spectrum (light blue curve). The measured b) and the *FROG* retrieved c) spectrograms are shown. The lower panels show the retrieved XUV pulse (green and black solid lines) and the retrieved phase (red dashed line) in the spectral d) and the temporal e) domain. The expected overall spectrum (black dashed line, panel a)) is additionally plotted in d).

nm has been chosen as appropriate design. B_4C interlayers ($\approx$ 1 nm) as well as a B_4C capping layer $\approx 3\ nm$ have been included. The mirror was designed (black solid line) for a combined usage with a 150 $nm\ Pd$ filter, which suppresses the low-energy spectral components (as depicted by the yellow curve in figure 4.9 a). Additional high-energy suppression above 130 eV via the intrinsic drop in photon flux from the HH cut-off of our source was taken into account in the design (figure 4.9 a) gray line). The final design exhibits a maximum reflectivity of about 15% centred at 107 eV and reflects over bandwidth of about 11 eV, as depicted by the solid black line in figure 4.9 a). The dashed black line depicts the expected XUV spectrum as a convolution with an analytical Gaussian HH spectrum and the transmission of the Pd filter and exhibits maximum intensity at 108.8 eV.

We observe reasonable agreement when comparing this simulation with the measured photoelectron spectrum (green dotted line in figure 4.9 a)) in the absence of the laser field (shifted by the binding energy in neon of 21.6 eV).

Depending on the shape of the HH cut-off, we expect Fourier limited pulses with durations between 190 and 210 as, and a bandwidth of about 10 eV. Moreover, bottom-up simulations reveal that the mirror's spectral phase extends the pulse duration by not more than 10 as beyond its Fourier limit. This includes effects on the pulse due to phase discontinuities around 100 eV and the Pd filter. The reason why this broadening appears to be so little is the sharpness of $N_{4,5}$ absorption lines; each of them is confined to a spectral range of sub-1 eV only. Thus, the total amount of power spread out to large time values is actually small.

The attosecond pulses have been characterized experimentally, by means of XUV pump/IR probe streaking technique (section 2.3.3.1) in Ne and analyzed by $FROG$ analyses [174], [120]. The measured (panel b)) and the retrieved (panel c)) spectrogram is plotted in figure 4.9. The absence of interference fringes and the presence of only one streaking curve in our spectrogram reveals clearly that there is only a single, isolated attosecond pulse exiting the mirror, which further confirms our expectations of only minor

phase effects.

Figure 4.9 c) shows the result of the appropriate $FROG$ retrieval. Signal from low energy secondary electron scattering has been subtracted by a cubic function in analogy to figure 2.24 in section 2.3.3.2 before the retrieval. Panels 4.9 d) and e) display the retrieved intensity (green line) and phase (red dashed line) of the XUV pulse, once in the spectral, once in the temporal domain. The expected XUV spectrum (black dashed lined in figure 4.9 a)) is additionally plotted in figure 4.9 d) for comparison. Due to the low energy resolution of our time-of-flight spectrometer dips in the photoelectron spectra due to the small dips in the mirror reflectivity are not visible. An attosecond pulse of 195 as could be retrieved, in very good agreement with the previous estimations.

4.3   Attosecond dispersion control by extreme ultraviolet multilayer mirrors

In this section specially designed aperiodic multilayer XUV mirrors are presented to furnish attosecond technology with the ability to control the spectral phase of attosecond pulses in addition to their spectral intensity. This offers a great degree of freedom in influencing the XUV pulse characteristics, such as the pulse shape, duration, frequency sweep and central wavelength by means of XUV mirrors. The presented experiment has been performed at the novel 45 degree beam-line $AS2$ [35] at the MPQ (appendix F, figure F.1). Most results of this work have been published in *Optics Express* (Hofstetter et al.) [57].

Principle idea

Chirped multilayer mirrors in the visible/infrared range, are inevitable components for the generation of few cycle laser pulses [59]. These pulses are the necessary driving pulses for single attosecond pulse generation by HHG (e.g. for the 80 as pulse presented in section 4.1.2). In contrast to the development of chirped dielectric mirrors in the visible, the realization of chirped XUV multilayer mirrors requires new approaches in computational design, manufacturing and characterization, which have not been available and combined until now.

So far, XUV dispersion control over multi-electron volt bandwidths could only be accomplished for photon energies below 100 eV [61], [62], [63], [19], [111]. Further, adherence control of the spectral distribution and chirp of an attosecond XUV pulse have been realized only by means of ultra-thin metal filters (typical thickness $\approx 100nm$) [61], [62], [63], [85] and XUV multilayer mirrors [19], [111] with chirp control mainly relying on the metal filter components. Now the applicability of thin metal filters is limited both by their strong XUV attenuation and by the availability of only a few filter materials (figure 2.15). Thereby dispersion control by metal filters is confined to specific spectral ranges, where

the real part of the complex index of refraction of a filter material provides sufficient (usually only negative) dispersion.

As shown in the following, specially designed non-periodic binary or ternary multilayer-coated XUV mirrors allow for a large degree of freedom in influencing the XUV pulse characteristics, including control over the attochirp by reflection off those mirrors [175].

Figure 4.10 displays a computational example for group-delay dispersion (GDD) management by non-periodic multilayer coatings optimized to introduce positive (left panel) or negative (right panel) GDD to an initially unchirped XUV pulse. Higher order dispersion control (as TOD) by non-periodic multilayer is also feasible, although not demonstrated here. The square of the electric field amplitude of the standing wave resulting from the superposition of the incident and reflected radiation depicted by the false-color plots reveals a penetration depth varying nearly linearly with photon energy in the centre of the high-reflectivity (HR) range of the multilayer Bragg peak ($\approx 100 - 130~eV$). The penetration depth increasing and decreasing with photon energy imposes a positive and negative chirp, respectively, on an originally bandwidth-limited attosecond pulse reflected by the mirror. The multilayer structure assumed here resembles the experimentally realized aperiodic multilayer mirrors as displayed in figure 4.11 (a) and (c).

Multilayer mirror design

To prove the validity of the concept for precision chirp control of attosecond XUV pulses, we have developed a set of three multilayer mirrors exhibiting distinctly different GDD but similar reflectivity characteristics. The multilayer designs have been calculated and optimized by a Fresnel equation thin film code coupled to a needle optimization algorithm [23]. Optimized for an incident angle of 45° they exhibit high reflectivity within the range of 100-130 eV with comparable bandwidth: $\Delta E = 11\text{-}13~eV~FWHM$. The mirrors have been designed for the combined usage with a 150 $nm~Pd$ fil-
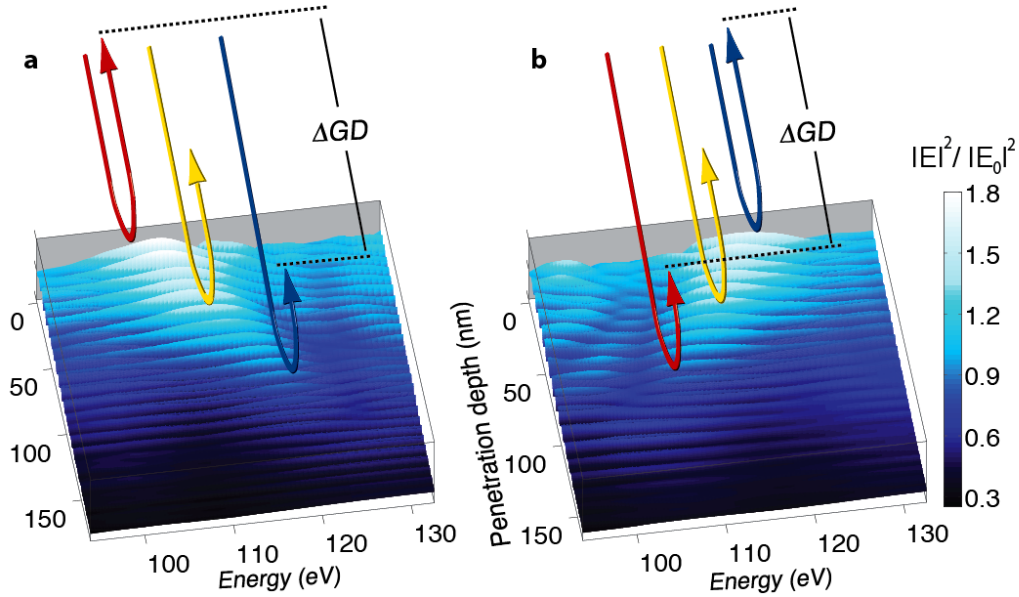
Figure 4.10: Operational principle of XUV chirped multilayers: Calculated square of the electric field amplitude of the standing wave formed in the multilayer structure upon reflection in the 94-133 eV photon energy range, normalized to that of the incident wave.

ter. Since isolated attosecond pulses can be extracted by spectral filtering from the cut-off part of the generated HH spectrum [2], the high energy extend of the spectrum has to coincide with the high reflectivity range of the mirror. The HH cut- off shape and the filter form a broad energy window outside which reflectivity does not affect the attosecond pulse generation. The calculated mirror designs have been optimized for additional suppressed reflectivity contributions in the near vicinity of the main Bragg peak and different central energies of the mirrors between 107-122 eV have been chosen to prove the tunability of this approach.

Starting from periodic Mo/B_4C start-designs chosen according to their bandwidth and central energy, many optimization iterations, including the cleaning of designs to decrease the number of layers to less than 40, the elimination of too thin layers, always interrupted by various stability tests against small layer thickness deviations have been performed. In the final design all layer thicknesses lie between 2 and 25 nm (lower panels, figure 4.11). The
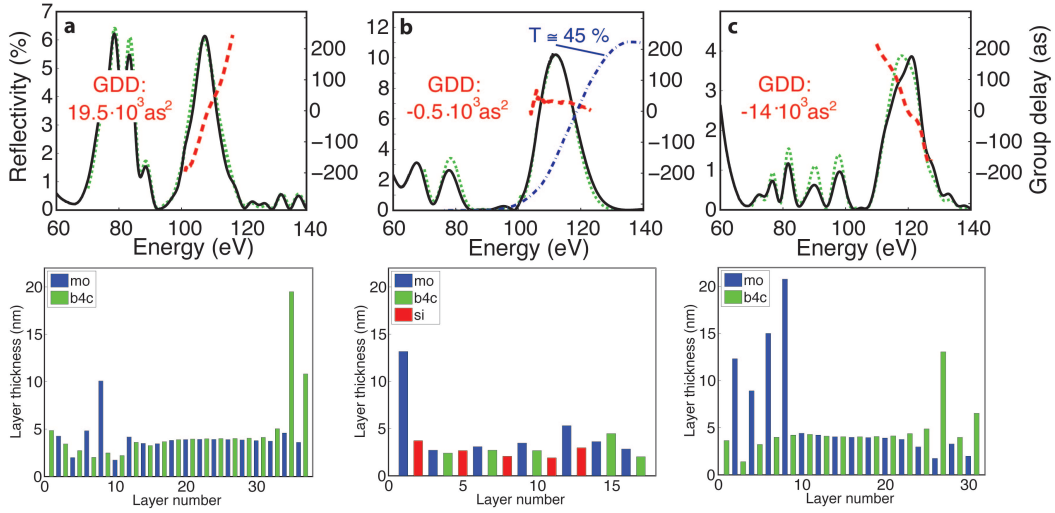
Figure 4.11: Set of XUV multilayers with positive (a), near zero (b) and negative (c) group delay dispersion. The upper panels compare the measured (solid black) with the designed (dotted green) XUV reflectivity curves. The calculated group delays ($d\phi/d\omega$) are also displayed (dashed red curve). The transmittance of a 150-nm Pd foil is additionally qualitatively plotted in panel (b), depicted by the blue dash-dotted line. The lower panels show the appropriate designs.

negative GDD mirror was the most difficult one to design and also showed most affect to variations in layer thicknesses and it was difficult to suppress GDD oscillations.

Figure 4.11 shows the calculated reflectivity and group delay of the three multilayer mirrors versus photon energy, compared with the measured XUV reflectivity using synchrotron radiation. The three mirrors are designed to introduce substantial positive GDD, negligible GDD, and substantial negative GDD, with computed values of $19.5 \cdot 10^3 as^2$, $-0.5 \cdot 10^3 as^2$, and $-14 \cdot 10^3 as^2$, respectively.

The measured and computed XUV reflectivity is in excellent agreement, revealing maximum peak reflectivity between 4 and 10 %. Notable deviations in the peak shape appear only in figure 4.11 near 120 eV, possibly due to minor uncertainties in the deposition layer thicknesses. Fitting our designed reflectivity curves to the measured XUV spectra reveals roughness of about 0.8 nm. This relatively high value, which exceeds the roughness values we mea-

sured in periodic Mo/B_4C stacks, can be attributed to thick Mo layers (10-20 nm) at the bottom of each stack.

Attosecond streaking

In contrast to the reflectivity, there is no standard frequency-domain technique available for measuring GDD in the extreme ultraviolet spectral range. Aquila et al. have characterized the GDD of a multilayer mirror by measuring the photoelectron yield from its surface [58]. Here we have resorted to attosecond metrology for measuring the attosecond pulse dispersion directly and assessing the mirrors' capability of controlling the chirp of isolated attosecond XUV pulses [176], [61].

The experiment has been performed at the $AS2$ (appendix F) of the MPQ, which allows for an easy and rapid exchange and alignment of the flat 45° XUV mirrors, which is inevitable for future XUV phase sensitive attosecond experiments. We have implemented attosecond streaking (section 2.3.3.1) by liberating photoelectrons from the $2p$ sub-shell of an ensemble of Ne atoms with sub-300-as XUV pulses filtered by the combination of a Pd foil and one of the bandpass multilayer mirrors described above.

Calibrating the recorded spectrograms: The electron kinetic energies were taken with a time of flight spectrometer (*Kaesdorf* [177]) with a sample rate of 250 ps. The electric lens increases the electron count rate in a particular, about 30 eV broad, energy range. Minor modifications of the flight time spectrum due to the action of the electrostatic lens are observed outside its energy acceptance window and therefore exert no influence on the retrieved pulse characteristics.

The TOF recorded electron flight time is converted into photoelectron energy by using the fact the electron kinetic energy is indirectly proportional to the squared flight time of the electrons (figure 4.12); further fine-tuning is performed by comparing both the XUV spectra and the photoelectron spectra before and after the mirror, which have been recorded with different filter materi-
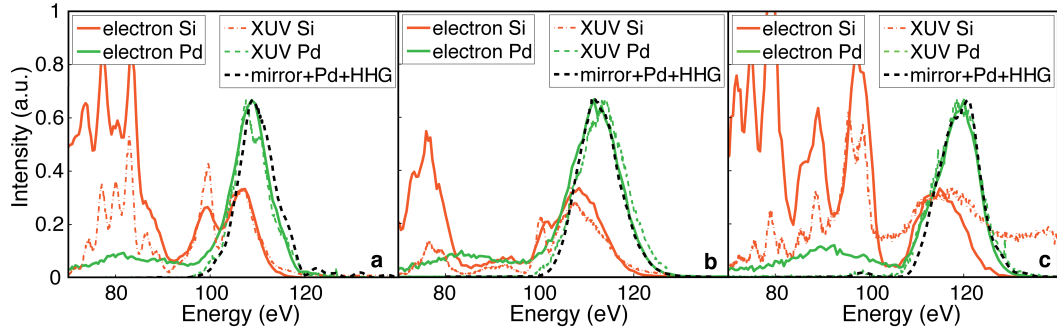
Figure 4.12: Comparison of calibrated electron spectra and calibrated photon spectra together and the mirror reflectivity measurement. The photo-electron spectra (continuous, colored lined) have been shifted by the ionization potential of Ne (21.6 eV) to match the spectra of the calibrated XUV photons (dashed lines). The dashed black line depicts the XUV mirror reflectivity multiplied with an artificial HHG spectrum and the transmission of a 150 nm thick Pd filter.
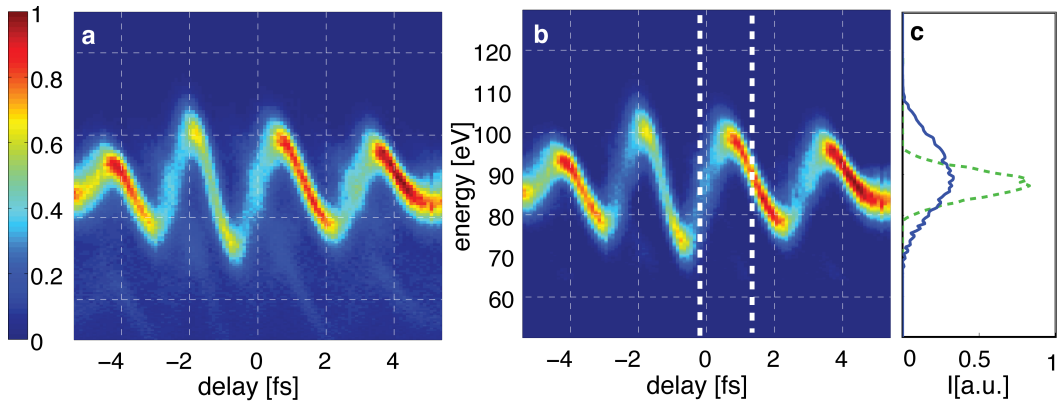
Figure 4.13: Effect of the background subtraction. Comparison of the raw-data spectrogram (left panel) and the background subtracted version (middle panel). The right panel shows two line-outs of the photoelectron spectra near the zero crossings of the vector potential taken at delays highlighted by the vertical white dashed line in panel b). The "blue" broadened photo-electron spectrum corresponds at a delay of -0.1 fs while the compressed (dashed green) spectrum is taken at a delay time of 1.4 fs.

als Al, Si and Pd. Both the TOF length (nominally 380 mm) and an energy shift due to the electric lens have been used as fit

parameters in a reasonable margin.

We use the $FROG/CRAB$ [122] algorithm $ATTOGRAM$ described in [120], [121], [178] to retrieve the vector potential of the laser pulse and the spectrum as well as higher order phase terms of the XUV pulse from the spectrograms.
Beside the main trace of the $2p$ electrons, there is a roughly 10 % contribution originating from a satellite pulse trailing the main attosecond pulse by half a laser period π/ω_L (where ω_L is the laser frequency) which originates from an attosecond burst from an adjacent half cycle, which is ideally spectrally filtered out to preserve the HHG components of only the single most intense attosecond burst. We eliminated those contributions by subtracting a properly time-shifted and normalized version of the spectrogram from itself. Aside from the satellite pulse, the $2p$ spectrogram is sitting on top of a low-energy background composed of electrons from the $2s$ sub-shell, inelastically scattered $2p$ electrons, as well as contributions from several shakeup channels, which was subtracted analytically by a cubic function as described in section 2.3.3.2, figure 2.24. Figure 4.13 compares exemplarily the directly measured photoelectron spectrogram in the case of the positive GDD mirror with its noise-subtracted version. Please note that all main features are fully visible directly from the raw-measurement (left panel) and remain unperturbed by this action.

Analyses

The resultant streaking spectrograms recorded with the three mirrors of figure 4.11 a)-c) are displayed in figure 4.14 a)-c) along with their corresponding $FROG$ retrievals in figure 4.14 d)-f), respectively. The calculated spectrograms appear to be in excellent agreement with the measured ones. Narrowing and broadening in the streaked electron spectra at the zero crossings is displayed by enhanced and diminished electron count rates, respectively.

The spectrograms clearly reveal signatures of the chirp imposed to the XUV pulse after being reflected by the chirped XUV multilayer mirrors. As has been explained in section 2.3.3.1 (figure 2.22)
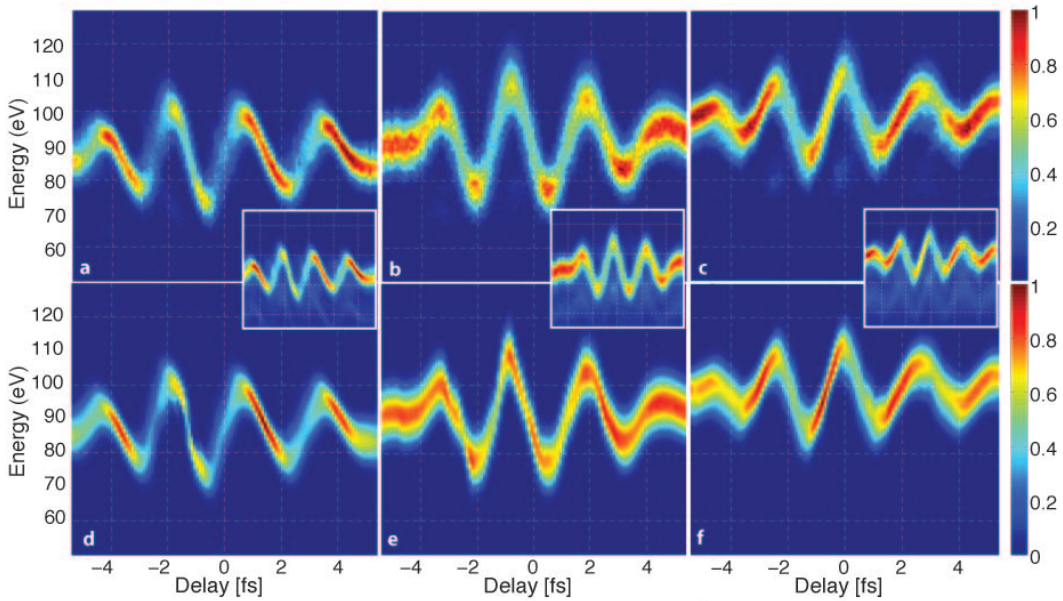
Figure 4.14: Measured and retrieved attosecond electron streaking spectrograms, upper and lower row, respectively. The insets show the recorded raw-spectra. Panels a)-c) and d)-f) display spectrograms recorded with attosecond pulses reflected off mirrors described in figure 4.11 a)- c), respectively.

due to the chirp, a positively-chirped pulse (as plotted in the left picture of figure 2.22) results in a streaking spectrogram exhibiting narrower/broader streaked spectra at the negative/positive slope of $\Delta p(t)$, exactly as revealed by figure 4.14 c) and 4.14 f). Conversely, a negatively-chirped pulse is predicted to produce a streaking spectrogram with narrower/broader streaked spectra at the negative/positive slope of $\Delta p(t)$, as displayed by figure 4.14 a) and d).

We can now turn our attention to a quantitative evaluation of the chirp carried by the attosecond XUV pulse in the three experiments performed with the three different mirrors. Figure 4.15 shows the retrieved spectral and temporal XUV pulse characteristics. Comparing the retrieved XUV spectra (green dotted lines) with the ones (passed through the Pd filter and XUV mirror) directly measured with an XUV spectrometer (solid black lines) shows a remarkable agreement of the bandwidth, spectral profile
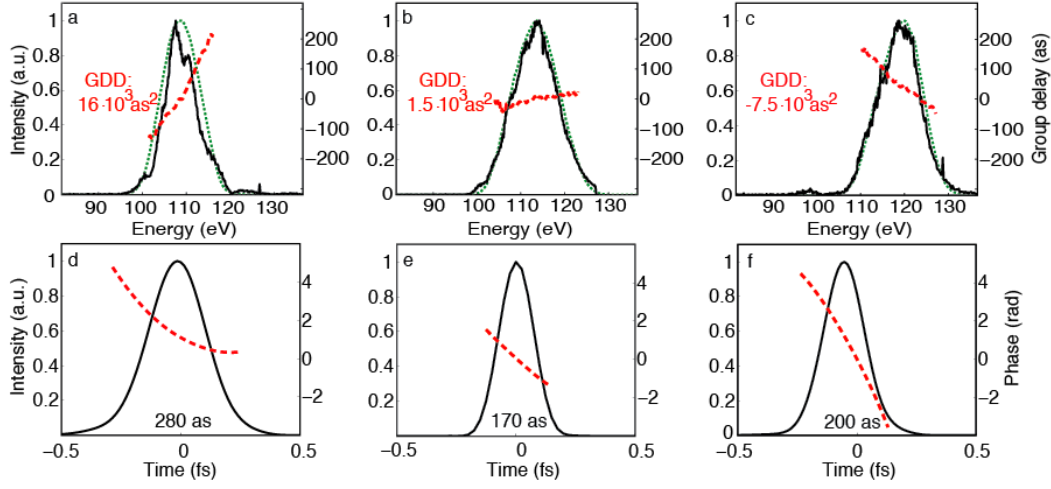
Figure 4.15: Retrieved spectral and temporal characteristics of the attosecond *XUV* pulse, upper row and lower row, respectively. Panels a), b) and c) display the intensity spectrum (green dotted line) and group delay (red dashed line) of the attosecond *XUV* pulse reflected off the mirror described in figure 4.11 a), b) and c), respectively, as retrieved from the measured streaking spectrograms shown in figure 4.14 a), b) and c) respectively. The black full lines depict the corresponding *XUV* spectra measured directly with an *XUV* spectrometer. The evaluated effective group-delay dispersions weighted by the final spectral *XUV* intensity are also shown. Panels d), e) and f) show the temporal intensity profile (black line) and temporal phase (red dashed line) retrieved from the streaking spectrograms of figure 4.14 a), b) and c) respectively. The *XUV* pulse duration (full width at intensity half maximum) has been evaluated and is displayed at the bottom of each panel.

and central energy position.

Table 4.1 summarizes the evaluated pulse durations and the *GDD* carried by the reflected pulses, in comparison with the designed *GDD* of the mirrors. Comparing the retrieved averaged *GDD* values (averaged over the spectral profile) with the design goals shows an excellent quantitative agreement for two of the mirrors a): positive *GDD* (to within 20%), and b): near zero *GDD* (to within $\approx 2 \cdot 10^3 as^2$, causing negligible pulse broadening in the 100 *as* domain), while the quantitative agreement is compromised by the same layer thickness errors in mirror (c) giving rise to the deviations in figure 4.11 c). Note that even thickness deviations on

Table 4.1: Comparison of XUV mirror designed and $FROG$ retrieved pulse parameters. The average GDD value and the appropriate standard deviation are calculated by weighting the calculated and the retrieved discrete GDD values with the intensity of the retrieved XUV spectrum over the whole spectrum. We find: (+) design: $16 \cdot 10^3 \pm 4 \cdot 10^3 as^2$; (+) retrieved: $19.5 \cdot 10^3 \pm 4 \cdot 10^3 as^2$; (0) design: $-0.5 \cdot 10^3 \pm 3 \cdot 10^3 as^2$; (0) retrieved: $1.5 \cdot 10^3 \pm 2 \cdot 10^3 as^2$; (−) design: $-14 \cdot 10^3 \pm 7.5 \cdot 10^3 as^2$; (−) retrieved: $-7.5 \cdot 10^3 \pm 2 \cdot 10^3 as^2$. The lower panels shows the retrieved pulse-length in comparison to their Fourier limit.

	(+) GDD M.	(0) GDD M.	(-) GDD M.
GDD design in $[10^3 \ as^2]$	$\phi''_{(+)} = 19.5$	$\phi''_{(0)} = -0.5$	$\phi''_{(-)} = -14$
GDD retrieval in $[10^3 \ as^2]$	$\phi''_{(+)} = 16$	$\phi''_{(0)} = 1.5$	$\phi''_{(-)} = -7.5$
Retrieved duration	$\tau_{(+)} = 280as$	$\tau_{(0)} = 170as$	$\tau_{(-)} = 200as$
Fourier limit	$200as$	$165as$	$175as$

an atomic scale result in significant changes of the mirrors spectral phase response though the reflectance suffers only minor modifications.

Uncertainties in the XUV optical constants of the multilayer materials Mo, B_4C and Si in the 100-130 eV energy range may also contribute to the residual discrepancies between design and measurement. The dispersion of the Pd filter appears to be less than $1.5 \cdot 10^3 \ as^2$ in the 100-130 eV photon energy range. The near-vanishing chirp of the attosecond pulse filtered from the cut-off range of the high-harmonic spectrum and reflected by the near-zero-GDD mirror b) at the same time validates theoretical considerations that predict the attochirp to vanish in the cut-off range.

Development of chirped normal incidence chirped La/Mo mirrors for 105 eV

Above, 45° multilayer mirrors based on a combination of either Mo/B_4C or $Mo/B_4C/Si$ have been proven to quantitatively control the chirp of a single attosecond pulse. In section 4.2, a novel material combination based on La and Mo has been introduced and tested in an attosecond streak camera experiment. Here now, two normal incidence chirped La/Mo mirrors are presented.

Aperiodic normal incidence La/Mo stacks at $\approx 105 \ eV$ which introduce/compensate a GDD of more than $\pm 10000 \ as^2$ upon a single reflection.have been designed and fabricated.
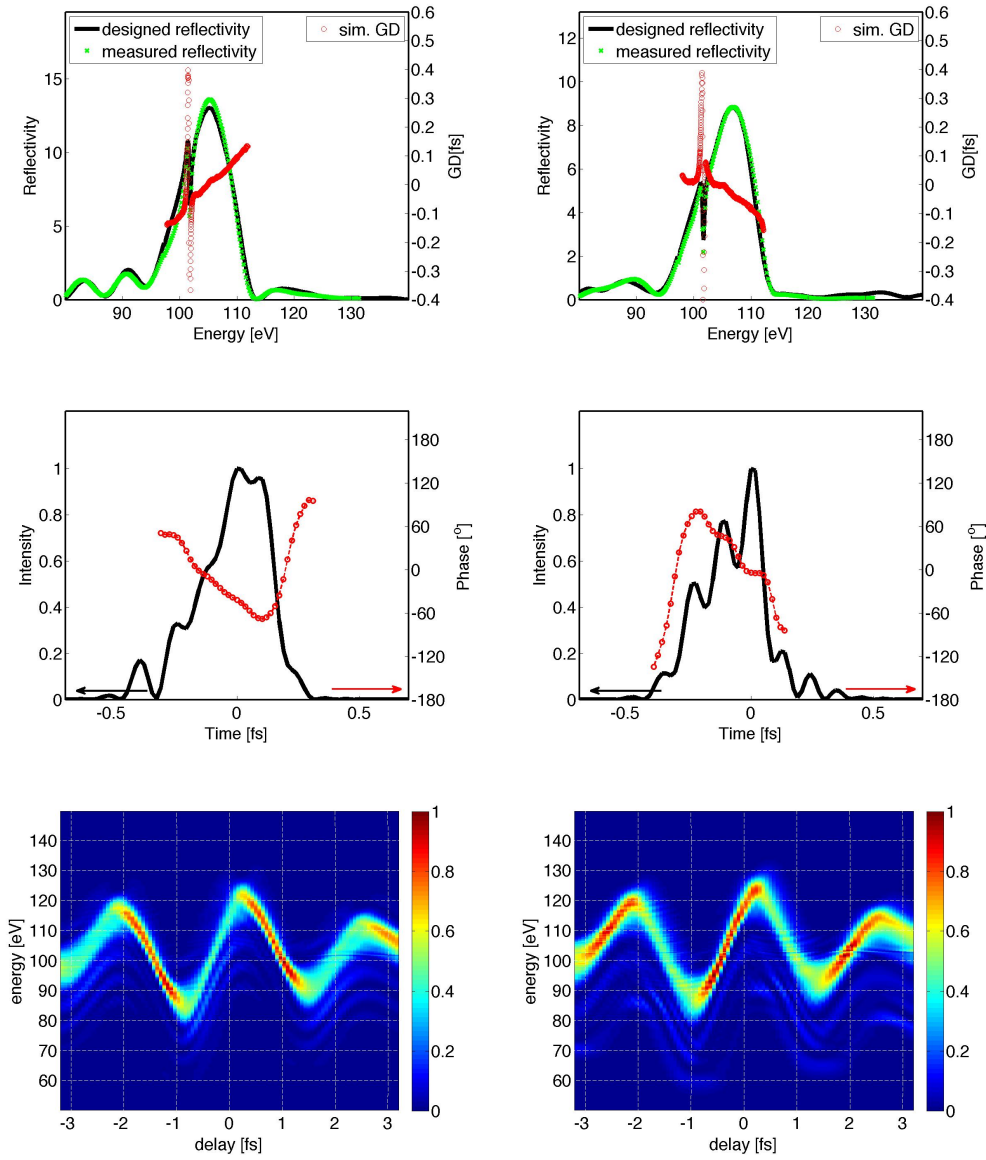
Figure 4.16: Set of normal incidence La/Mo mirrors for chirped pulse generation. The left/right panel displays the results for a positively/negatively chirped multilayer mirror, respectively. 1st row: XUV reflectivity simulations and measurements. 2nd row: Calculated pulse length by Fourier transforming the spectral reflectivity if the mirror. The 3rd row displays a simulated spectrogram. For more details please read the text.

The useful bandwidth of those mirrors was chosen to support the reflection of a 200 as Fourier-limited pulse. These aperiodic stacks have been designed using evolutionary algorithms [23] and exhibits an extreme case of almost maximum possible chirp for a given bandwidth of $\approx 12\ eV$. Designs with less GDD (of both signs) or less bandwidth would be easy to implement.

B_4C is included as an additional material in these designs yielding a larger parameter space to explore in the multiple design goals, namely, broad bandwidth, essential amount of GDD, large peak reflectivity and a low reflectivity outside the useful spectral range of the main reflectivity peak. Beside that, B_4C is used as a passivating interlayer between Mo and La and as a capping layer on top of the stack.

The XUV reflectivity of these mirrors has been measured [143] and is displayed in the upper row of figure 4.16, together with the appropriate simulation of the reflectivity and phase. One finds rather perfect agreement between the measured and the designed XUV reflectivity based on the novel measured optical constants of La. Reflectivity of 9 % (positive GDD mirror) and 14 % (negative GDD mirror) could be measured for nearly identical bandwidths of 12 eV. The fitted Nevot-Croce-roughness $\sigma \approx 0.55\ nm$ agrees very well with the σ value of 0.6 nm found in the case of periodic stacks $La/B_4C/Mo/B_4C$ stacks (section 4.2). Row 2 in figure 4.16 displays the temporal structure as calculated by Fourier transform of the spectral mirror characteristics. Row 3 shows the appropriate *simulated* spectrograms. Depending on the sign of the GDD, their zero transition electron peaks, appear either broadened or compressed as explained in figure 2.22.

The temporal substructures of the pulses are a consequence of second order reflectivity peaks in the spectral domain as visible in the reflectivity spectrum of the mirror (row 1) of the spectrograms. Using these mirrors on HHG cutoff radiation in combination with a Pd filter, would yield spectrally and temporally clean attosecond pulses without further spectral ringing.

Both the negative GDD and the positive GDD mirror are expected to lengthen a 200 as pulse to about 300 as. For a theo-

retical prove, a constant GDD term of converse sign was added to the mirror phase in the simulation and enabled the theoretical compression to less than 215 as. This finally proves the validity of La/Mo mirrors for chirped attosecond pulse generation at 105 eV normal incidence with only minor effects from the $La\ N_{4,5}$ absorption edges.

4.4 Spectrally cleaned attosecond pulses by ternary multilayer mirror coatings above 115 eV

Until recently, attosecond experiments were limited to photon energies below 100 eV due to the available HH intensities and appropriate XUV optics. While La based multilayer mirrors work especially well up to 130 eV (section 4.2 and [125]) and again above 150 eV (as will be presented in section 4.5), different material combinations are required in the intermediate spectral region.

As found from table 3.6, Mo/B_4C multilayer mirrors [179], [180] reveal highest reflectivity between 120 eV and 150 eV in high period stacks. High reflecting Mo/B_4C mirrors make use of the very low absorption of both materials and the consecutive large number of contributing periods due to the large penetration depth; but their small bandwidth makes these mirrors unfeasible for attosecond pulse reflection. La based and Mo/Si multilayers on the other hand exhibit much higher single interface reflectivity but here the XUV penetration depth is very limited.

Ternary $Mo/B_4C/Si$ mirrors are suggested in this section as reflecting optics in the energy range between 120 and 160 eV. After analyses of the benefit of a third material in multilayer XUV coatings and the more detailed investigation of the properties of this material combination, experimental results on both high reflecting and broadband $Mo/B_4C/Si$ mirrors are presented (section 4.4.1).

In the previous sections, the combination of a multilayer mirror with a thin metal filter has been to filter and shape an isolated pulse from the HH spectrum. Here the combination of the mirror and the filter worked as spectral cleaner at the low energy XUV radiation, while the shape of the HHG cut-off itself ensured clean spectra at the high energy side.

The spectral range above 100 eV lacks appropriate filter materials as indicated by figure 2.15. Suppression of low energy components must thus be implemented in the mirror's reflectivity shape. Beside their applications in spectral ranges without appropriate filter materials, also experiments which require a high spectral resolution (of $\approx$1-5 eV) benefit from such spectral cleaning mirrors

as both the filter 'opening' and the HH 'cut-off decrease' may not happen *fast enough* to sufficiently suppress all out-of band spectral contributions.

Finally in section 4.4.2 ternary aperiodic $Mo/B_4C/Si$ spectral cleaning mirrors are introduced and tested in attosecond streak camera set-ups, allowing for the first characterization of single isolated attosecond pulses at 120 eV.

Part of this work has been published in the peer-reviewed conference proceedings of the *Ultrafast Phenomena* 2010 (Hofstetter et al.) [112]. Attosecond streaking experiments took place at the $AS3$ beam-line at the MPQ.

4.4.1   Three material multilayer mirrors

Multilayer mirrors in the visible spectral range can be built from nearly absorption-free materials. This allows for nearly perfect interference coatings with octave spanning reflectivity up to almost 100 % [181] and nearly arbitrary spectral phases [182], [183]. As already stated in the beginning, there are no nearly absorption-free materials in the XUV range.

In contrast to the visible, where the absorption part in the refractive index can be neglected, here, the optical constants are truly two-dimensional as exemplarily depicted in figure 4.17 for the case of Mo, Si and B_4C at 130 eV. As will be analyzed in detail in the following, this two-dimensionality is the reason why one can benefit from a third material per period in an XUV multilayer.

Periodic ternary-material stacks are denoted as follows: Each period of thickness d consists of three different materials a, b and c in defined order and with layer thicknesses d_a, d_b and d_c. Three different γ_j with $j \in [a, b, c]$ depict the ratio of a distinct layer thickness to the period: $\gamma_j = \frac{d_j}{period}$, with $\Sigma_i \gamma_i = 1$.

There are three ways on how an XUV coating can benefit from a third or even fourth material:

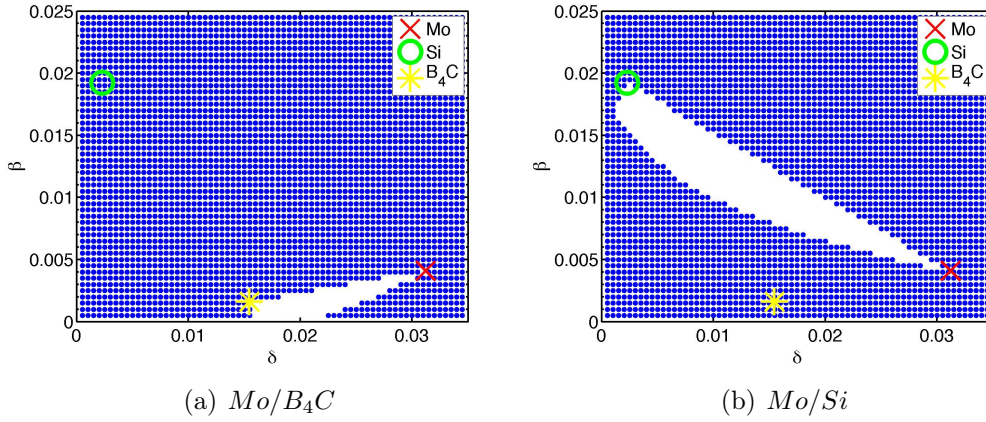1. The **single period reflectivity may be increased** as al-

(a) Mo/B_4C (b) Mo/Si

Figure 4.17: Two period reflectivity gain in a Mo/B_4C (panel a)) and a Mo/Si stack (panel b)) at 130 eV by the third material Si (panel a)) and B_4C (panel b)), respectively. The blue crosses depict optical constants of a possible third material for which the single period reflectivity may be increased. Calculations are based on equation D.10 in appendix D, which compares the reflectivity of 2 periods of a bi-material stack with that of two periods of a ternary material stack analytically. All possible γ and $\tilde{n}$ values have been scanned numerically and a blue cross was painted on each refractive index position where possible gain was found.

ready indicated by equation 2.28:

$$r^2_{singleIF,\theta=0} \propto \Delta\delta^2 + \Delta\beta^2$$

This equation identifies the normal incidence single interface reflectivity amplitude $r_{singleIF,\theta=0}$ between two materials 1 and 2 as the distance of the refractive indices ($\Delta\delta = \delta_2 - \delta_a$; $\Delta\beta = \beta_2 - \beta_1$) in the two-dimensional refractive index plane (Pythagorean theorem). As the optical constants of three materials span a triangle, three interfaces ($1\rightarrow2$, $2\rightarrow3$, $3\rightarrow1$) per period instead of two ($1\rightarrow2$, $2\rightarrow1$) can increase the reflectivity, for the sake of non-optimum interface positions. Figure 4.17 shows the period reflectivity gain exemplarily for the case of a Mo/B_4C (left panel) and a Mo/Si (right panel) multilayer centred at 130 eV. As the optical constants of Si in panel a) and of B_4C in panel b) lie inside the "blue crossed area", both two-material multilayer periods may benefit from the third material.

2. Bi-layer XUV stacks are not always based on two low-absorption materials, as one high absorbing material may increase the single interface reflectivity (equation 2.28). An additional third and low absorptive material in such a two-material stack, can **increase the penetration depth** without changing the position of the original interfaces. Therefore more periods may contribute, resulting in a possibly higher overall reflectivity.

3. When designing aperiodic multilayer mirrors, the third material per period allows for a **larger variety of possible designs**. Multilayer mirrors are interference coatings. So a higher number of interfaces per period increase the parameter space of possible designs. Also the possibly larger penetration depth increase the number of layers and thus the tunability of aperiodic mirror designs.

Ternary periodic stack optimization: Figure 4.18 a), b) displays the realistic simulation of the maximum reflectivity and the appropriate bandwidth of a 19 period $Mo/B_4C/Si$ stack with a central energy of 130 eV in dependency of the fractions of the materials $\gamma(Mo)$, $\gamma(Si)$ and $\gamma(B_4C)$ per period in false color representation. Figure 4.18 c), d) displays the result of the same material combination, calculated in a stack with 100 periods centred at 126 eV, respectively.

One finds, that the optimum fraction of the individual materials in a ternary stack depends on the period number N. One reason is the higher single interface reflectivity of Mo/Si compared to Mo/B_4C, which itself is less absorptive. Comparing the two-material stack simulations (x and y axis and diagonal in figure 4.18), Mo/Si is the more favorable choice in the broadband (19 period) multilayer and B_4C as third material increases the reflectivity by more than 25 % mainly by an increased single period reflectivity. The bandwidth stays comparable (figure 4.18 b)).

Mo/B_4C on the other hand is the better high periodic stack bilayer combination, and a third more absorbing material (here Si) decreases the penetration depth and thus the number of contribut-

(a) R_{max}: N=19, 130 eV

(b) bandwidth: N=19, 130 eV

(c) R_{max}: N=100, 126 eV

(d) bandwidth: N=100, 126 eV
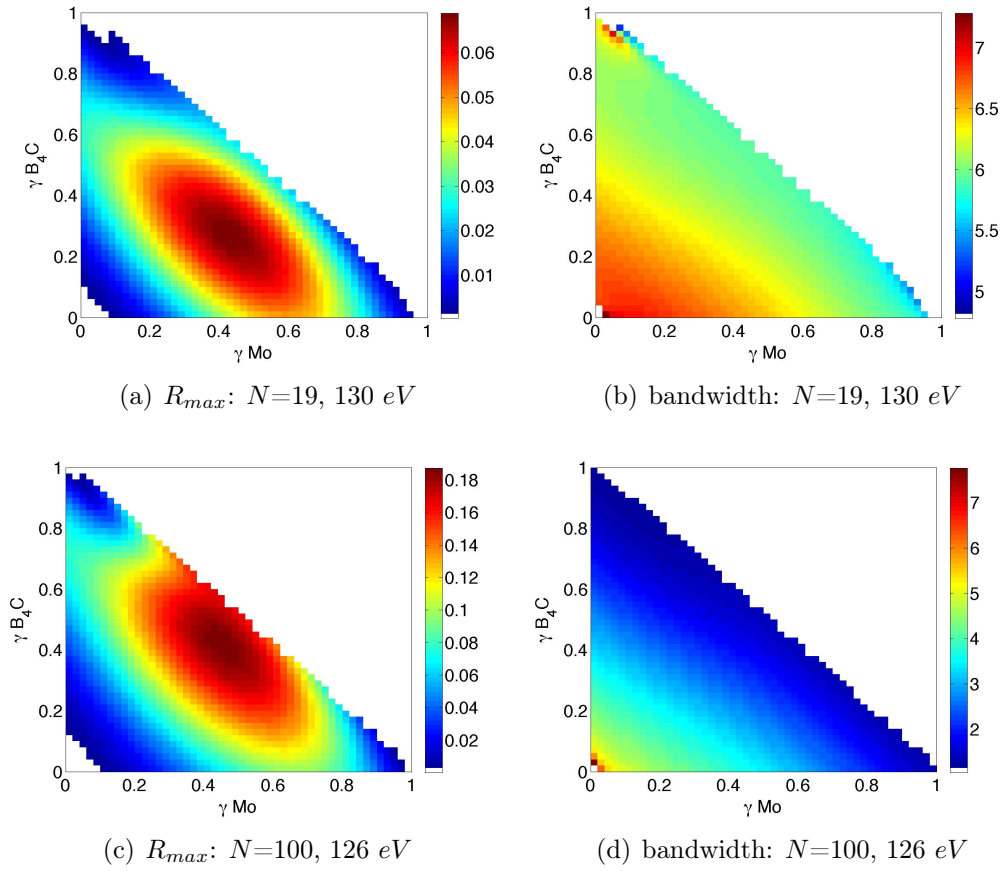
Figure 4.18: Simulated maximum reflectivity (left column) and bandwidth (right column) of $Mo/B_4C/Si$ stacks, in dependency of the individual fractions of $\gamma(Mo)$ and $\gamma(B_4C)$ within the stack ($\gamma(Si) = 1 - \gamma(B_4C) - \gamma(Mo)$). Upper panels show the result of a 19 period multilayer centred at 130 eV. The lower panels correspond to a 100 period stack centred at 126 eV. Realistic roughness σ of 0.75 nm has been assumed. $MoSi_2$ interlayer formation is not included. Highest reflectivity is found in the first case for mixing coefficients of about $\gamma(Mo) = 0.4$, $\gamma(B_4C) = 0.25$ and $\gamma(Si) = 0.35$. In the case of the high period mirror (panel c) and d)) $\gamma(Mo) = 0.4$, $\gamma(B_4C) = 0.5$ and $\gamma(Si) = 0.1$ yields maximum reflectivity.

ing periods. But even in this high period case, there is an optimum non-zero γ_{Si} fraction of about 10 % for which a 10% reflectivity increase can be expected. Due to the additional larger bandwidth as a consequence of the limited penetration depth (figure 4.18 d)), the integrated reflectivity increase is even larger.

Measurement and analyses of a ternary $Mo/B_4C/Si$ **stack:** The broadband ($N = 19$) mirror has been fabricated according to the optimized design plotted in figure 4.18 (see figure caption for details). Figure 4.19 compares the measured reflectivity of this peri-
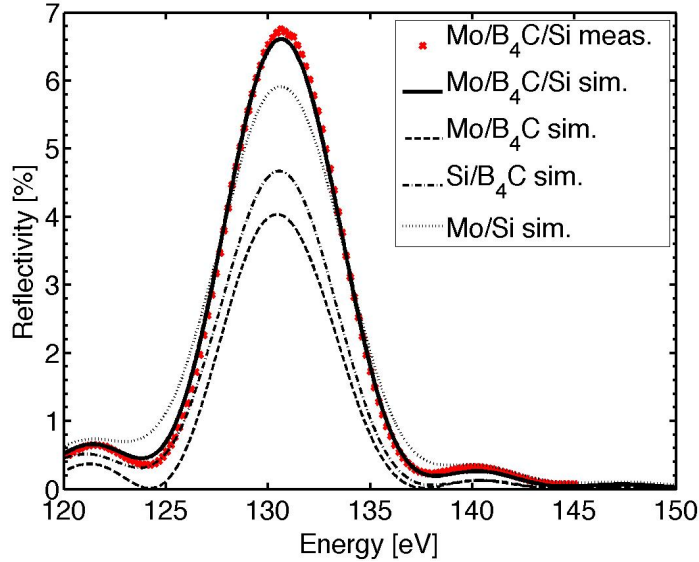
Figure 4.19: Comparison of XUV simulations of three $N = 19$ periodic two-material stacks Mo/B_4C (black dashed line), Si/B_4C (black dashed-dotted line) and Mo/Si (black dotted line) with the simulated (solid black line) and the measured (red dots) XUV reflectivity of an appropriate $N = 19$ $Mo/Si/B_4C$ coating. The three-material stack design is a result from simulations depicted in the upper panels of figure 4.18 and exhibits a maximum reflectivity of almost 7 %. The two-material multilayer designs have been chosen for the same central energy and the appropriate γ values have been optimized to exhibit highest possible reflectivity: $\gamma(Mo/B_4C) = 0.5$, $\gamma(Si/B_4C) = 0.5$, $\gamma(Mo/Si) = 0.6$. Realistic $MoSi_2$ interlayer formation has been included in the simulations. The design of the $Mo/Si/B_4C$ stack assumes a roughness value of 0.75 nm. For the simulation of all two-material stacks a Nevot-Croce roughness of $\sigma = 0.4$ nm has been used which is significantly lower than expected and observed from other two -material reflectivity measurements.

odic $Mo/B_4C/Si$ stack with the simulated XUV reflectivity of the appropriate Mo/Si, Mo/B_4C and Si/B_4C two-material stacks. The measured reflectivity exceeds that of comparable two-material analogs, especially as the simulations of all two-material multilayers have even been performed with a Nevot-Croce roughness value

of 0.4 nm which is lower than expected in reality. More detailed information is given in the caption of figure 4.19.

Figure 4.20 summarizes the measured XUV reflectivity [143] of two high reflecting ($N = 100$) and two broadband ($N = 19$) ternary material $Mo/B_4C/Si$ stacks. Their design compositions have been chosen again according to appropriate maximum reflectivity simulations as presented in figure 4.18. Slightly lower maximum reflectivity than in these simulations can be accounted to the here included $MoSi_2$ interlayer formation which has been neglected previously. The "red mirror" has been presented in figure 4.19. The "black mirror" has been designed and fabricated with an equivalent fraction of the individual materials, but a period thickness of about 5 nm instead of 4.85 nm. The two high period (N=100) stacks are almost pure Mo/B_4C stacks with only small fractions of Si ($\gamma = 0.1/0.15$). The "blue" mirror corresponds to simulations in panel c) and d) of figure 4.18. A maximum reflectivity of 15.3 % could measured in reasonable agreement with the simulations. The "green" mirror optimization at 147 eV is not explicitly shown here and yielded an optimum reflectivity design for $\gamma(Mo) = 0.35$, $\gamma(B_4C) = 0.5$ and $\gamma(Si) = 0.15$ and a maximum reflectivity of 10.7% could be achieved.

The measurements of our mirrors consistently reveal an estimated XUV Nevot-Croce roughness between $0.7 - 0.75$ nm, independently of the design and layer number. Note that three-material multilayer designs set even higher constraints on the deposition and the roughness due to the thinner layers.

Here, all mirrors have been designed for near normal incidence and a period thickness of not more than 5 nm. For comparison, Zwicker et al [179] could show about 10 % reflectivity around 120 eV under 60 degree normal incidence ($d > 7$ nm). The explicit design values are not given in the publication, but one can roughly estimate the interface roughness to be well above 1 nm.

The high period $Mo/B_4C/Si$ multilayer of figure 4.20 centred at 147 eV contains amorphous Mo layers with thicknesses smaller than 1.5 nm. The TEM image of this mirror has been shown in figure 3.14 b). An almost identical deduced Nevot-Croce roughness
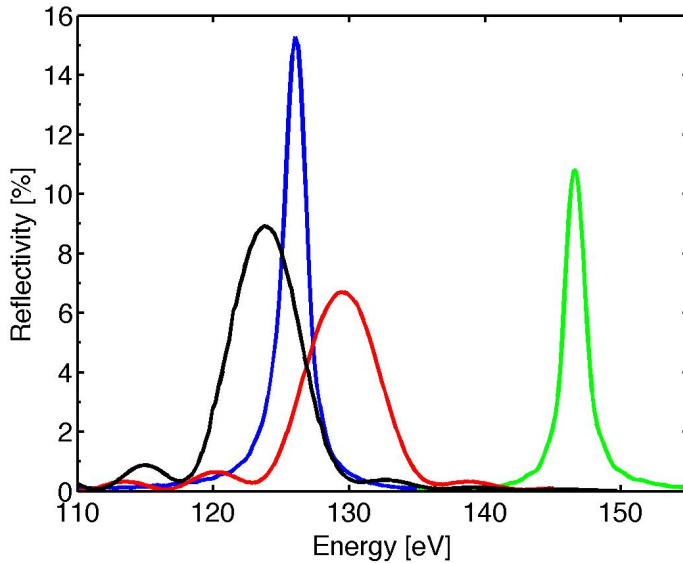
Figure 4.20: *XUV* reflectivity measurements of two broadband ($N = 19$) (red and black curves) and two high period ($N = 100$) (blue and green curves) periodic $Mo/B_4C/Si$ tri-material multilayer mirrors. For details please see text.

of $\sigma = 0.73$ compared to polycrystalline Mo mirrors could be fitted. This confirms the validity of ternary $Mo/B_4C/Si$ multilayer coatings, even in the thickness regime of amorphous Mo.

Aperiodic designs, optimized for the highest reflectivity gain per period, could even increase the overall reflectivity. The resultant design would look very similar to that of spectral cleaning mirrors presented in figure 4.21 b). We will make use of this in the following section and further deploy the larger parameter space originating from the larger number of interfaces per period in ternary stacks to design spectral cleaning mirrors for the energy range between 120 and 140 eV.

4.4.2   Spectral cleaning

The spectral cleanness of a pulse is a key issue in isolated attosecond pump-probe experiments. One benefits in different ways from a suppression of spectral contributions from regions beside the main Bragg peak:

First of all, some experiments as the investigation of the absolute dynamics of two adjacent electronic states require a certain spectral resolution. Here the importance of spectral cleanness is most obvious as the out of band signal may overlap the second electronic state and wash out or even cover the signal of interest.

Secondly, more than one peak in the spectral domain yields additional pulses in the temporal domain, as predicted from Fourier analyses. Beside that, especially in aperiodic multilayer mirrors, the spectral phase outside the central peak is usually not "in phase" with the main peak so the mirror itself may generate pedestals or secondary pulses delayed in time. Thus, an unclean spectrum results in an unclean temporal intensity and thwarts single attosecond pulse experiments.

Thirdly, single attosecond pulse generation by spectral gating utilizes a spectral high-pass to filter isolated pulses from attosecond pulse trains. Low energy XUV radiation is likely to stamp from more than one attosecond pulse. So low energy spectral "dirt" in a mirror transmits spectral components from more than one *isolated* attosecond pulse separated from each other by half a laser cycle.

In streak camera experiments, latter two points generate secondary pulses (delayed in time) in the same spectral region as the main pulse. As each pulse generates its own streaked electron traces, these will overlay in the final spectrogram and are difficult to separate from the signal of interest.

4.4.2.1 Design

Beside their optimization for spectral cleaning and the flattest possible phase, the following $Mo/B_4C/Si$ mirrors have been optimized for the highest possible reflectivity. *Optilayer* has been used for the final design [23].

Highest possible reflectivity increase per period within constraints on the minimum layer thicknesses, factually results in three different multilayer stacks on top of each other. Maximum single period reflectivity is required at the bottom of the stack. Approaching

(a) design mirror "A"

(b) design mirror "B"

(c) *XUV* reflectivity mirror "A"

(d) *XUV* reflectivity mirror "B"
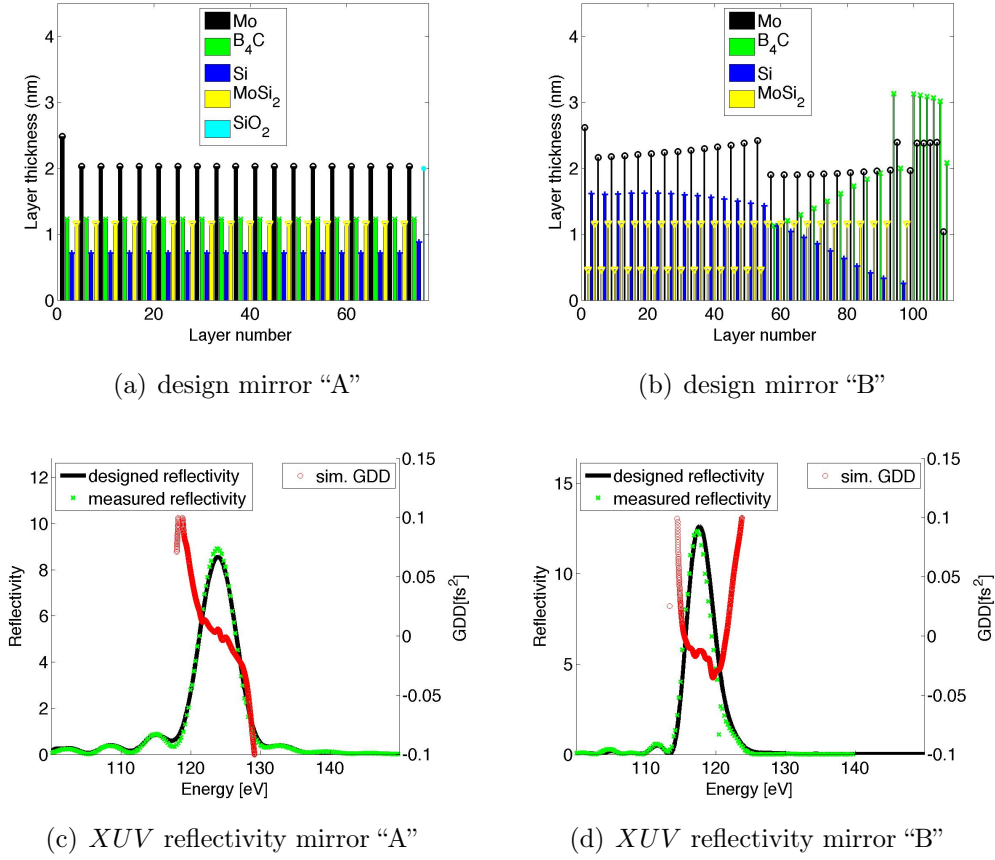
Figure 4.21: Comparison of the design (upper panels) and the simulated and measured *XUV* reflectivity (lower panels) of a periodic $Mo/B_4C/Si$ multilayer mirror (left column) and an aperiodic spectral cleaning mirror (right column).

its top, an increasing fraction of *spacer* materials ensures a large fraction of radiation penetrating the stack deeply [33]. Due to their large Fresnel coefficients (figure 2.9) Mo/Si is picked here as the bottom material combination, starting at $n = 1$ from nearly $\gamma = 0.5$, [2] with an increasing fraction $\gamma(Mo)$ with the period number, as Mo is the *spacer* in this spectral range. The low absorption material combination Mo/B_4C is chosen as "stack top" material combination. In the intermediate area ternary $Mo/B_4C/Si$ periods compromise both high interface reflectivity and low absorption.

---

[2]As retrieved in appendix D, equation D.8 highest single period reflectivity is found for $\gamma = 0.5$.

The appropriate design is displayed in figure 4.21 b).

Figure 4.21 compares the design (a) and the reflectivity (c) of a periodic ternary $Mo/B_4C/Si$ stack (introduced as black curve in figure 4.20) with that of an aperiodic spectral cleaning mirror (panels b) and d)). XUV reflectivity measurements (green circles) reveal a maximum reflectivity of 12 % and a bandwidth of 4.4 eV centred around 118 eV in the latter case. Correct modeling of the $MoSi_2$ interlayers results in very good agreement between the calculated and the measured XUV reflectivity in both cases.

As described in section 3.5 the aperiodic spectral cleaning mirror design has not been perfectly implemented here, as the asymmetry of the Mo/Si_2 interfaces has first not been taken into account. The resulting XUV mirror reflectivity is slightly shifted in energy and reveals a reduced signal to noise ratio of 27 (figure 3.15 in section 3.5) compared to originally designed s/n >70. This anyway exceeds the ratio of the comparable periodic mirror in the left column by a factor 3 and can be utilized in the following for a much cleaner signal.

Spectrally cleaned attosecond pulse generation   The following experiments have been performed at the beam-line $AS3$ at the MPQ [108]. It uses the typical $\approx 5^o$ normal incidence double mirror- delay stage set-up, very similar to the $AS1$ plotted in figure 2.19. This beam-line is capable to vacuum conditions of about $10^{-11} mbar$ and thus especially suited for solid state experiments.

The two mirrors introduced in figure 4.21 have been applied to Xe gas and photo-electron spectra have been recorded (figure 4.22 a) and b)). Although the out-of band reflectivity suppression has not been perfectly implemented, a much cleaner electron signal could be recorded in the case of the aperiodic mirror allowing for a spectral separation of the Xe 5s peak from the electron background, which is not possible in the periodic case. This could pave the way towards delay measurements between the 5s and the 5p state in Xe in close similarity to the experiment just recently published by M. Schultze et al. [3] in Ne, where we could resolve a delay of 21 as in the photo-ionization process from the 2s and the

$2p$ state.

(a) photo-electron spectrum mirror "A"   (b) photo-electron spectrum mirror "B"
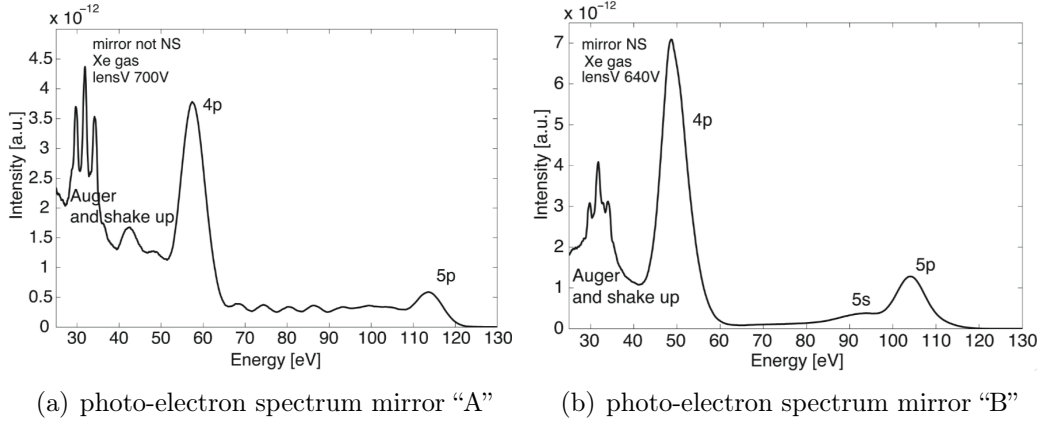
Figure 4.22: *Xe* photo-electron spectra [184] recorded with the mirrors presented in figure 4.21. Panel a) corresponds to the "left column" periodic mirror of figure 4.21, while panel b) is the appropriate spectrum to the "right column" spectral cleaning mirror in figure 4.21 b), d). Please note, that the photo-electron spectra have only been calibrated in energy, but not in intensity.
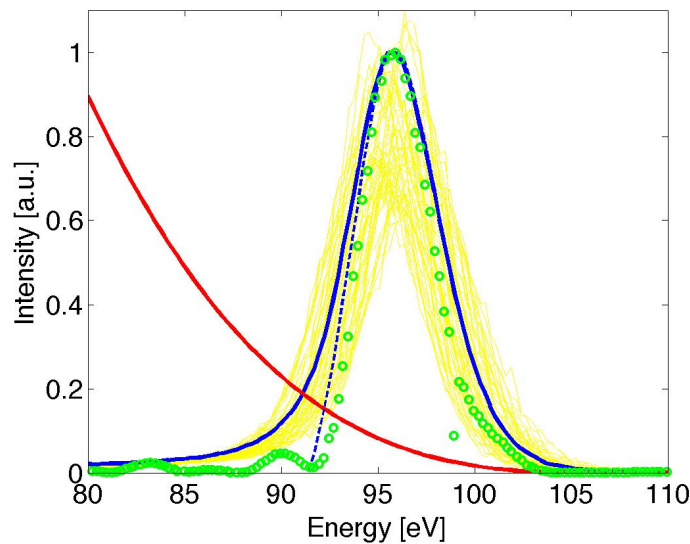
Figure 4.23: Analytical noise subtraction from the photo-electron spectrogram recorded with the spectral cleaning mirror introduced in the right column of figure 4.21. For details please read text.

For the temporal pulse characterization, the spectral cleaning

mirror of figure 4.21 has been applied to attosecond streaking in Ne (figure 4.24). The small secondary reflectivity peak at the low energy side of the mirror's XUV reflectivity (figure 4.21 d)) is buried under secondary electron signal. For a more realistic analyses, I have subtracted the secondary electron signal by a cubic function as displayed in figure 4.23, before feeding the spectrogram into the algorithm. Here, the solid blue line shows the average of all delay-dependent electron spectra (thin yellow lines) from the measured spectrogram in figure 4.24 a), shifted in energy by their center of mass to coincides with the reflectivity of the mirror (shifted by the binding energy of 21.6 eV in Ne) depicted by the green circles. A cubic function (red line) has been used to model the secondary electrons in analogy to the discussion in section 2.3.3.2 yielding the blue dashed spectrum.

Figure 4.24 displays the results from the measurement (a) together with its appropriate $FROG/CRAB$ retrieval (b). Due to the spectral cleaning, one finds an isolated and very clean measured streaking trace (a) and very good agreement between the $FROG/CRAB$ retrieved spectrum and the mirror reflectivity (c). A retrieved GDD of about $-20 \cdot 10^3 \ as^2$ exceeds about twice the calculated average mirror GDD of $-8 \cdot 10^3 as^2$. The GDD of the Pd filter is negligible at that central energy. It is up to date not clear where this deviation comes from, but corresponding analyses indicate, that the effect of an electric lens at the TOF entrance has not been fully eliminated, yielding the exaggeration of chirp. Fourier transform of the calculated spectral characteristics of the mirror results in a pulse length of about 410 as exceeding the Fourier limited pulse length by not more than 8 as. In excellent agreement to this estimation the $FROG/CRAB$ analyses returns as well a pulse-length of 410 $as \ FWHM$ (panel d).

Finally, a second set of spectral cleaning mirrors has been prepared, including the asymmetry of the Mo/Si_2 interfaces in the design to deposition-time conversion. Two mirrors centred at 125.5 and 134.5 eV as displayed in figure 4.25 have been designed, developed and measured. Excellent agreement between the design goals and the XUV reflectivity measurements is observed and both mir-

(a)   (b)

(c)   (d)
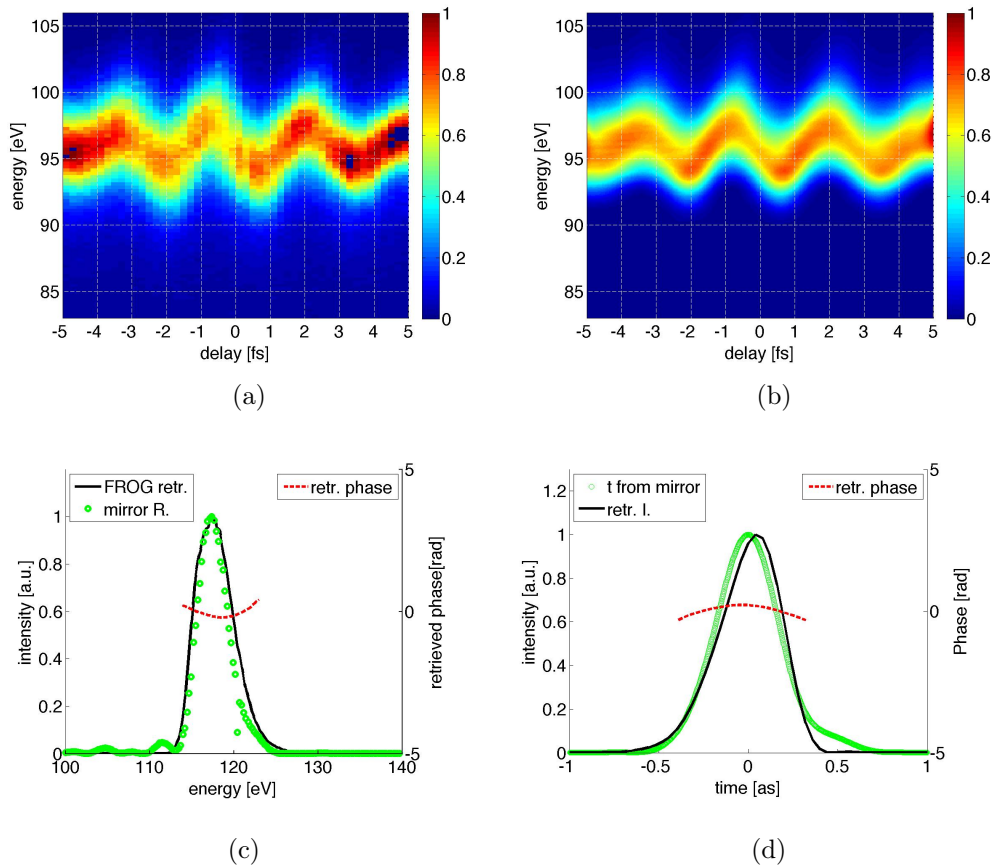
Figure 4.24: *FROG/CRAB* analyses (panel b)) of a measured spectrogram (panel a)) recorded with the spectral cleaning mirror introduced in figure 4.21. Panel c) and d) show the retrieved pulse, once in the spectral, once in the temporal domain. Both the spectral and the temporal structure retrieved from *FROG* analyses (black lines) and from the mirror (green circles) agree very well.

rors reveal a normal incidence signal to noise ratio greater than 50.

Maximum reflectivity of $R_{max} = 8.6\%$ and a a bandwidth of 4.5 eV was measured for the "left column mirror" centred at 125.5 eV. The "right column noise suppressor" reveals $R_{max} = 7\ \%$ at 134.4 eV and a measured bandwidth of 5.2 eV. The design of the latter mirror is even more complicated, as thin Mo layers between 1.6 and 2 nm have been avoided, what is not trivial at this high central energy as exactly these layer thicknesses would yield an
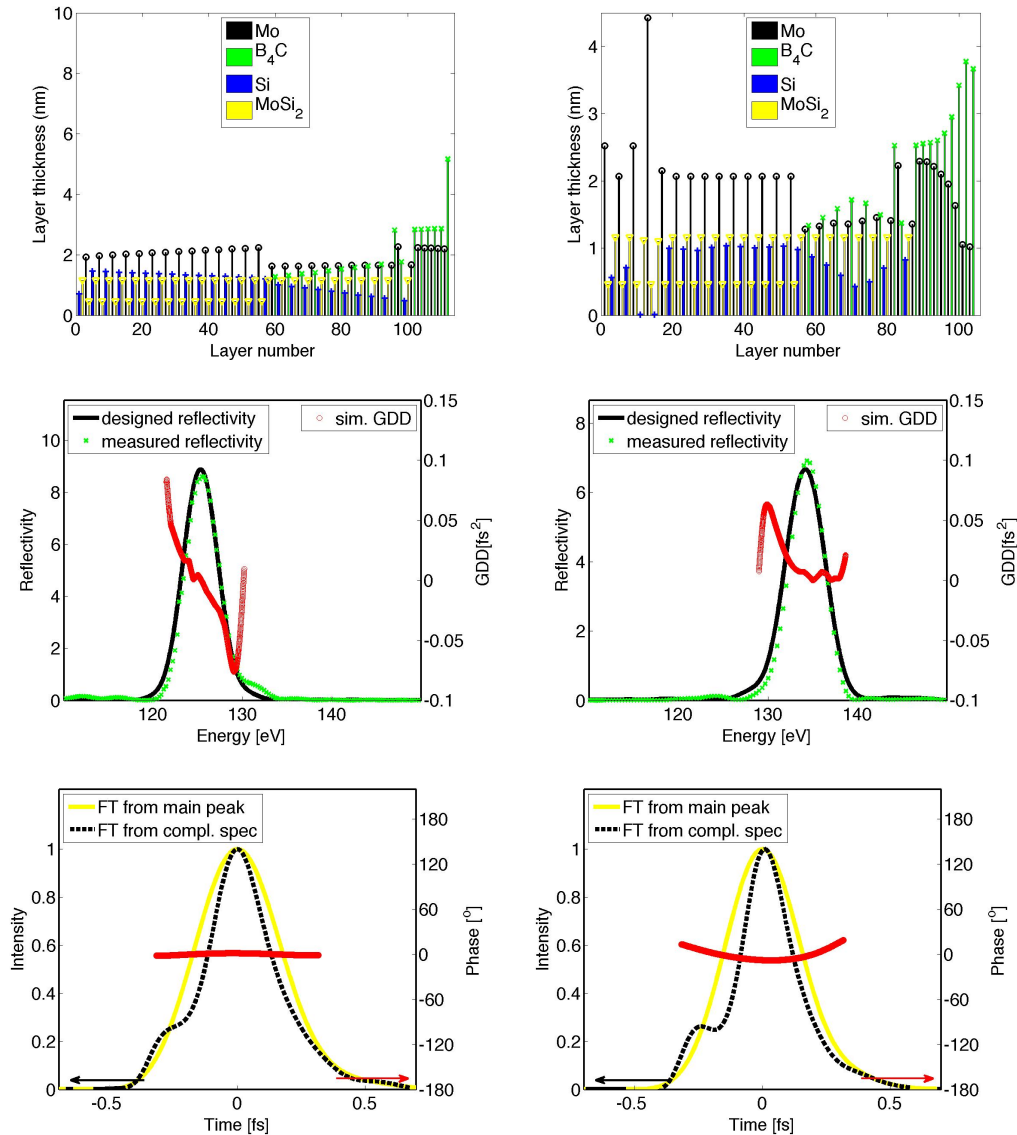
Figure 4.25: High signal to noise ($s/n > 50$) mirrors. Each column depicts the design (first row), the simulated and measured reflectivity and the simulated GDD (second row) of novel spectral cleaning mirrors. The third row shows the expected temporal structure of a pulse calculated as the Fourier transform of the mirror's spectrum and phase once only from the main peak spectrum (solid yellow line), once from the complete energy range plotted in the second row (dashed black line).

even better performance.

The third row of figure 4.25 shows the expected temporal struc-

ture by Fourier transforming the mirror's spectral reflectivity and its spectral phase. For an estimation of the effect of the "rest" signal from outside the main peak, Fourier transform of the complete spectrum (dashed black line) is compared with a Fourier transform of the spectrum, where outer spectral components have been numerically eliminated (solid yellow lines). The effects of those outer-band spectral contributions on the temporal intensity are not negligible, but small and isolated attosecond pulses are expected.

Spectral phase effects on the other hand are rather small. The main peak pulse length is close to its Fourier limit and we reveal 380 *as* (Fourier limit: 370 *as*) in the case of the left column mirror and 345 *as* (Fourier limit: 330 *as*) for the right column mirror.

These mirrors may enable attosecond spectroscopy experiments at these *XUV* photon energies in the nearest future.

4.5 High energy La/B_4C coatings above 150 eV

Attosecond experiments with pulses of even higher photon energies benefit again from the even shorter wavelength of light. A larger number of materials may be investigated as deeper bound electronic states can be probed; the generation of ever shorter pulses may become possible as the oscillation period shrinks; the spatial resolution could be higher; one possibly gets a cleaner photoelectron signal as one works spectrally further separated from the low energy background.

Up to date no single attosecond pulses above 140 eV could be generated due to the low photon flux of appropriate sources. But ongoing research in the HHG in gases and solids and the ongoing developments in FEL physics, will enable higher energy single attosecond pulse sources in the near future. HHG XUV energies up to the "water window" regime could be shown already [89], [90].

Here now, first La/B_4C multilayer mirrors fabricated with our IBD tool are presented and give a promising outlook on near future attosecond optics above 150 eV. The combination of La and B_4C exhibits high reflectivity when being applied to multilayer optics either between 90 and 120 eV or between 150 and 188 eV as depicted in the simulation of figure 3.13. Promising results from Häussler et al. indicate by TEM images from La/B_4C cross-sections [180] that La/B_4C multilayer stacks can be deposited stable and with low interface roughness. In the thesis of S. Hendl [125] La/B_4C multilayer coatings for both spectral ranges have been intensively analyzed.

In the energy spectral range below 120 eV, La/Mo multilayer mirrors exhibit a higher reflectivity both in broadband and high period designs (section 4.2). Thus, in this section the focus lies on the applicability of La/B_4C coatings for energies above 150 eV.

XUV **reflectivity measurements:** Four different La/B_4C stacks have been designed, fabricated and measured. Figure 4.26 compares the XUV reflectivity measurements of these four different La/B_4C mirrors centred at 160, 172, 184 and 191 eV. The mir-
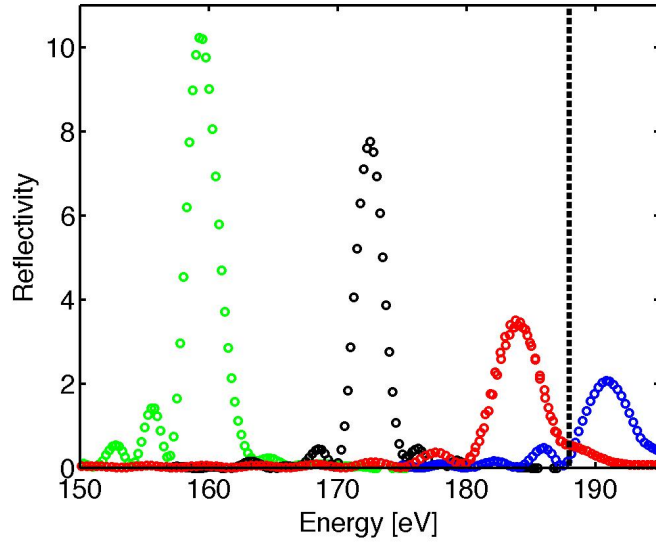
Figure 4.26: Measured XUV reflectivity of four La/B_4C stacks. All mirrors have been capped with 3 nm B_4C to suppress oxidation. The green curve depicts the XUV reflectivity of a 60 period $\gamma \approx 0.4$ stack centred at 159.5 eV; a reflectivity of 10 % and a bandwidth of 2.8 eV could be measured and its Nevot-Croce roughness can be estimated to 0.6 nm. The black curve corresponds to a $N = 60$ period stack with $\gamma \approx 0.4$. $R_{max}=$ 7.7 % at 172.5 eV and $\Delta E = 2.7$ eV was measured, yielding a roughness value of $\sigma \approx 0.7$ nm. The red curve shows is the reflectivity of a $N = 40$ stack measured under an angle of 10.2 degrees for a maximum reflectivity close to the B edge. 3.4 % reflectivity at 184 eV and a bandwidth of 4 eV could be measured. The "blue" $N = 50$ mirror reveals a maximum reflectivity of 2.05 % centred at 191 eV (above the 188 eV $B-K$ edge) and a bandwidth of more than 4 eV yielding an estimated $\sigma \approx 0.7$ nm.

rors have not been designed for highest possible reflectivity but tested for their applicability of La/B_4C for attosecond normal incidence optics. With period numbers between $N = 40 - 60$, the mirrors exhibit bandwidths between 2.5 and 4 eV and thus support the reflection of attosecond pulses between 400 and 700 as.

Design and measurement details can be found in the figure caption of figure 4.26. Due to the relatively high roughness of ≈ 0.7 nm the reflectivity drops with increasing central energy. This nearly linear decrease starting with a reflectivity of 10 % at 160 eV is even extendable over the $B-K$ absorption edge at 188 eV

and more than 2 % maximum reflectivity could be identified for a 4 eV bandwidth mirror with a central energy of 191 eV.

From these measurements the appropriate average Nevot-Croce roughness can be estimated between 0.6 and 0.75 nm. This value is slightly lower than estimations from S. Hendl [125] who found a Nevot-Croce roughness of his La/B_4C mirrors between $0.78 - 0.8nm$[3].

Long-term stability of La/B_4C mirrors in air ambient: The stability of our La/B_4C material combination against air exposure has been tested as this is important for an easy experimental handling. The La/B_4C stack with the lowest bilayer thickness has been chosen as test sample -thus the 191 eV central energy mirror displayed in figure 4.26- as thinner layers are more sensitive to small variations.
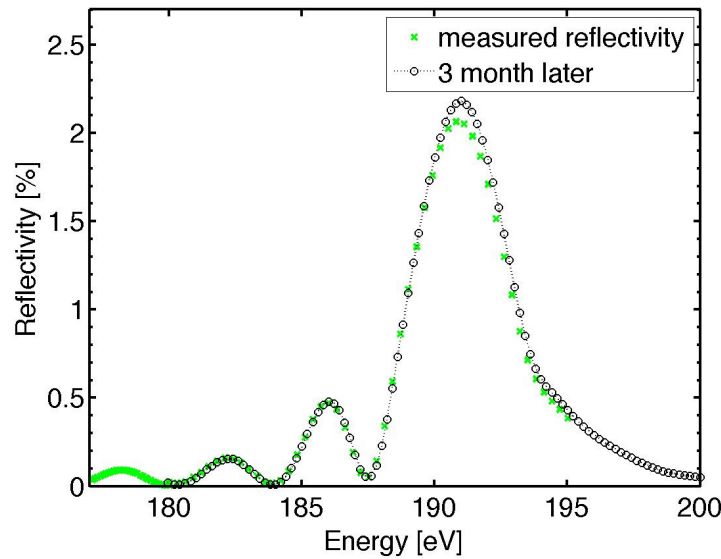
Figure 4.27: Long-term stability check of a 50 period, $d = 3$ nm, La/B_4C multilayer mirrors. Please read the text for more design details.

In analogy to the measurement presented in section 4.2, a witness sample has been sealed under nitrogen, water free environment

---

[3] In contrast to the presented results here, his mirrors have been produced by electron beam evaporation [125].

and the time between unpacking and XUV measurement was tried to be kept short. A second reflectivity measurement has been performed 3 month later after storing the mirror in room temperature air ambient. Figure 4.5 compares the two XUV measurements. Again, only minor variations can be observed in the XUV reflectivity measurements, what ensured the applicability of La/B_4C mirrors as near future normal incidence high energy attosecond optics.

Conclusions: The presented mirrors could enable normal incidence attosecond pulse reflection at these high energies in the near future. This holds especially, as simulations predict a reflectivity increase by introducing a third material(e.g. Si) in analogy to the presented $Mo/B_4C/Si$ stacks of the last section. Further S. Hendl has proven the possibility of lowering the interface roughness by means of ion polishing [125]. Applying this to our already lower roughness La/B_4C mirrors could yield even higher reflectivity.

Chapter 5

Conclusions and outlook

Conclusions: The optimization, development and characterization of (a)periodic XUV multilayer optics for attosecond pulse shaping and their application in attosecond experiments has been presented.

A combination of the materials Mo, Si, B_4C, La and Sc has been proven to be able to cover the spectral range between 30 and 200 eV with high reflecting normal incidence multilayer optics. Detailed knowledge on the material properties and the mirror structure resulted in excellent agreement between mirror designs and measurements. Simulations of La-based multilayer mirrors has been based on an improved set of La optical constants measured in the XUV/soft-X-ray range between 30 eV and 1.3 keV presented in this thesis.

Normal incidence ultrabroadband XUV mirror-coatings which support the normal-incidence reflection of sub-2 cycle attosecond pulses both at 40 eV and at 70 eV central energy have been designed, fabricated and characterized. Latter mirror enabled the generation of the shortest ever measured isolated pulses of 80 as, based on the recent development of phase stabilized nearly single-cycle IR/VIS driving laser pulses and an optimized XUV mirror/filter bandpass.

First isolated attosecond pulses above 100 eV have been presented based on the ability to fabricate appropriate optics in a stable and reproducible manner and recent developments of XUV gas HHG sources.

The novel material combination of La and Mo, especially suited for the generation of attosecond pulses in the energy range between 80 and 130 eV has been introduced, analyzed and finally tested in attosecond streaking measurements.

Quantitative control of the attochirp and thus the temporal structure of a pulse additionally to its spectral characteristics has been implemented by means of aperiodic multilayer mirrors and characterized in attosecond streaking experiments above 100 eV photon energy. Precision control of the phase characteristics of attosecond pulses adds an important technical capability to the toolbox of attosecond technology, affording promise for pushing its frontiers to higher temporal resolution.

The benefit of ternary multilayer XUV coatings compared to binary stacks has been proven exemplarily for $Mo/B_4C/Si$ coatings between 120 and 150 eV. Aperiodic ternary multilayer mirror designs allowed for the development and realization of the novel concept of spectral cleaning mirrors, especially useful for the generation of attosecond pulses in energy regimes, where no appropriate filter materials are available.

Nowadays single attosecond gas HHG sources give hope to extend the cut-off range limit to even higher energies in the nearest future. Normal incidence 2-5 eV broad multilayer mirrors based on La and B_4C with reasonable reflectivity at central energies between 160 and 200 eV have been fabricated and characterized, supporting the reflection of attosecond pulses up to nearly 200 eV.

Outlook: There are different directions where current developments may evolve in the near future. All of the here presented concepts of XUV attosecond pulse shaping by means of XUV multilayer mirrors, as the generation of Fourier limited pulses, phase control and spectral cleaning are not restricted to the presented spectral regions and material combinations, but are adoptable to different energy ranges and different multilayer material combinations.

The extension of attosecond physics towards higher energies could enable higher spectral, spatial and temporal resolution and

the probing of electronic and even nucleonic dynamics in a larger number of materials, as deeper bound states may be addressed. Especially when entering the "water window" spectral range above 282 eV once with isolated attosecond pulse technology a completely new spectrum of e.g. attosecond *in vivo* experiments may become possible.

The technique of spectral phase control can be extended to third and higher order phase term treatment as well and is applicable to any spectral range, where high reflecting multilayer mirrors are producible. HH radiation contains, due to its generation process, intrinsically an essential amount of chirp in a spectral range outside the cut-off region. Precise dispersion control of attosecond pulses could allow to push the limits to even shorter pulse-lengths by including spectrum from the chirped HH plateau region to the pulse and compressing it down to the Fourier-limit. Moreover, control over electronic motion in photoionization by chirped few-cycle attosecond pulses was recently predicted in a theoretical work by Peng et al. [185].

Absolute control of the chirp becomes even more interesting when we reach the regime of nonlinear processes in the XUV range, where for example coherent control by chirped pulses could be achieved. Future seeding FELs by coherent XUV radiation allows for controlling the spectral and temporal FEL pulse output [186] and thus requires precise control over the spectral seed chirp as could be provided by the multilayer mirrors described in this thesis.

Spectral cleaning is as well not restricted presented spectral range or the usage of three material multilayer coatings, although the higher degree of freedom in the mirror design supports a better performance. This technique may become a key tool for future high energy experiments where the spectral resolution due to the lack of filter materials relies only on the XUV multilayer.

Different pulse-shaping concepts by means of multilayer mirrors are as well thinkable. Fabry Perot stacks [33] consisting of two XUV multilayer coatings on top of each other, separated by a spacer layer of arbitrary thickness, could enable the generation of

two temporally delayed XUV pulses; this could be extended to two-color pulse generation "delay mirrors", with a graded spacer layer, where the position on the mirror defines the delay, finally enabling XUV-pump/XUV-probe experiments.

The question arises, if there was a limit of the bandwidth of optics and therefore a limit for the shortest possibly reflected attosecond pulse. As at least $N = 2$ periods are required, for an interference coating, the 32 eV ($FWHM$) broad mirror presented in this thesis is probably the broadest possible normal incidence flat-phase mirror design at 70 eV. Equation 2.40 suggests that moving to higher central energies E relaxes the constraints on the relative bandwidth. E.g. Mo and B_4C exhibit the required smoothness of optical constant in the broad range between 60 and 188 eV. But also the Fresnel reflectivity drops dramatically with increasing energy as depicted in figure 3.13 and the currently available photon numbers cannot compensate for that. Simulations on a two-period Mo/B_4C coating at 100 eV central energy propose a bandwidth of more than 50 eV and thus could support the reflection of 40 as long pulses, but the maximum reflectivity is predicted to be smaller than 1‰. Same holds for aperiodic normal incidence flat-phase optics. Two alternative approaches are suggested by the author:

- In alternative attosecond beam-line set-ups, in which the focusing and delay is de-coupled from the multilayer mirror, as e.g. in the $AS2$ set-up depicted in appendix F, one could substitute the mirror by more than one grazing (even total reflection) incidence XUV (multilayer) optics for flat phase reflection. The compensation of chirp has here to be implemented either with filters or with additional chirped multilayer optics.

- The interaction length and thus the stack height of a multilayer mirror depends on the pulse length. Therefore chirped mirrors consist of more contributing periods and reflect larger bandwidths than comparable periodic designs. Two-mirror stretcher-compressor set-ups as commonly known from the

visible (e.g. chirped pulse amplification) may additionally add degrees of freedom to the pulse- shaping at higher energies actually sacrificed by the need of two XUV reflections.

Summarizing, aperiodic XUV multilayer mirror optics have served and will serve the generation of single attosecond pulses and the shaping of these pulses, due to the large tunability of both spectral and temporal characteristics.

Appendix A

Gaussian pulse analyses

Here Gaussian pulse analyses is performed analytically. Beside the retrieval of the Gaussian $FHWM$ representation in the time-domain (section A), its corresponding occurence in the spectral domain and the time-bandwidth product is retrieved (section A). In section A an analytic expression for the length of a Gaussian in dependence of its Fourier-limited length and its GDD is retrieved.

$FWHM$ form of a Gaussian

The general form of a Gaussian pulse in the time domain t is given by:

$$E(t) = E_t e^{\frac{t^2}{2\sigma^2}} e^{-i\omega_0 t} e^{-i\phi(t)} \tag{A.1}$$

Here E_t is the amplitude, σ defines its width and ω_0 is the central frequency. The $FWHM$ pulse length is defined in terms of intensity:

$$\tau_0 = FWHM(|E(t)|^2) = FWHM(E_t e^{\frac{t^2}{\sigma^2}}) = 2\sigma\sqrt{ln2} \tag{A.2}$$

Using this relation in the general form of a Gaussian (eq. A.1) directly yields the Gaussian $FWHM$ form (eq. 2.4):

$$E(t) = E_t e^{-2ln(2)\frac{t^2}{\tau_0^2}} e^{-i\omega_0 t} e^{-i\phi(t)} \tag{A.3}$$

Retrieval of the time-bandwidth product

Using the relation

$$\int e^{-Ax^2 - Bx} = \sqrt{\frac{\pi}{A}} e^{B^2/4A} \tag{A.4}$$

one can calculate the Fourier transform of equation 2.4 (in analogy to eq. A.3):

$$\frac{1}{\sqrt{2\pi}} \int E(t)e^{i\omega t}dt = \frac{1}{\sqrt{2\pi}} \int E_t e^{\frac{t^2}{2\sigma^2}} e^{-i(\omega-\omega_0)t} = \sqrt{\frac{\tau_0^2}{4ln2}} E_t e^{\frac{-(\omega-\omega_0)^2}{8ln2}\tau^2} \quad (A.5)$$

Comparing the exponent of equation A.5 with the $FWHM$ presentation (eq. A.3) directly leads to:

$$\frac{2ln2}{\Delta\omega^2} \overset{!}{=} \frac{\tau^2}{8ln2} \quad (A.6)$$

Reordering this equation yields the time-bandwidth product for a Gaussian pulse (equation 2.6).

$$\Delta\omega\tau_0 = 4ln(2) \quad (A.7)$$

Retrieval of the GDD dependent pulse-length

One can deduce an analytical expression for the length of a Gaussian pulse τ in dependence on its Fourier limited pulse-length τ_0 and its GDD. Let us assume a Fourier limited Gaussian pulse in the spectral domain $G(\omega)$ as given in equation 2.5. This pulse has a bandwidth $\Delta\omega$ and thus a corresponding pulse length $\tau_0 = 4ln(2)\Delta\omega$.

In the following this pulse is compared to one with a constant $GDD = \phi''$. Its spectral field can be written as:

$$E(\omega) = G_\omega exp[(-\frac{2ln2}{\Delta\omega_0^2} + i\frac{\phi''}{2})(\omega - \omega_0)^2] \quad (A.8)$$

A Fourier transformation into the time domain using again the integral relation A.4 one finds for the temporal field amplitude:

$$\tilde{E}(t) = G_t exp(\frac{4(ln2)t^2}{2(\Delta t^2 + 4i(ln2)\phi'')}) \quad (A.9)$$

The pulse duration is defined as the $FWHM$ of the intensity. Thus one has to square this equation. Doing that and comparing the result with the definition of a Gaussian (equation A.1), one ends up with the equation 2.12

$$\tilde{\tau} = \tau_0\sqrt{1 + \frac{16(ln2)^2\phi''^2}{\tau_0^4}}$$

Appendix B

Pulse-length in dependence on noisy GDD

In this section an analytical expression for the pulse-length of a Gaussian with normally distributed $GDD = \phi''$ around zero with a standard deviation σ is retrieved.

The expectation value of the pulse-length $\mathscr{E}(\tau)$ can be calculated in dependence on σ and its Fourier-limited pulse-length τ_0 using equation 2.15:

$$\mathscr{E}(\tau) = \tau_0 \mathscr{E}\left(\sqrt{1 + \frac{\alpha \phi''^2}{\tau_0^4}}\right) = \frac{\tau_0}{\sigma\sqrt{2\pi}} \int_{-\infty}^{\infty} dx \sqrt{1 + \frac{\alpha x^2}{\tau_0^4}}\, e^{-\frac{-x^2}{2\sigma^2}} \tag{B.1}$$

with $\alpha = 16(ln2)^2$ and $x = \phi''$.

The square root can developed into a series of summands if the standard deviation is small, namely if the following conditions are fulfilled:

$$if \quad \frac{\alpha x^2}{\tau_0^4} < 1 \quad \leftrightarrow \quad x < \frac{\tau_0^2}{4ln2} \simeq 2.8^1$$

The expectation value can then be written as:

$$\mathscr{E}(\tau) = \frac{\tau_0}{\sigma\sqrt{2\pi}} \int_{-\infty}^{\infty} dx (1 + \sum_{n=1}^{\infty} \underbrace{\frac{1/2(1/2-1)...(1/2-n+1)}{n!})(\frac{\alpha}{\tau_0^4})^n}_{b_n} x^{2n} e^{-\frac{-x^2}{2\sigma^2}}$$

$$\tag{B.2}$$

$$\mathscr{E}(\tau) = \frac{\tau_0}{\sigma\sqrt{2\pi}} \left(\sqrt{2\pi}\sigma + \sum_{n=1}^{\infty} 2\frac{1 \cdot 3 \cdot ... \cdot (2n-1)(\sigma\sqrt{2})^{2n+1}\sqrt{\pi}}{2^{n+1}} b_n\right) \tag{B.3}$$

---

[1] Exemplarily for a pulse with pulse-length $\tau_0 = 100\ as$ (200 as, 300 as or 1 fs resp.) this relation holds true for $x < 3600\ as^2$ ($< 14400\ as^2$, 32400 as^2 and 350000 as^2)

$$\mathscr{E}(\tau) = \tau_0 \left(1 + \sum_{n=1}^{\infty} 1{\cdot}3{\cdot}...{\cdot}(2n-1){\cdot}\sigma^{2n} b_n\right) \tag{B.4}$$

$$\mathscr{E}(\tau) = \tau_0 \left(1 + \sum_{n=1}^{\infty} 1{\cdot}3{\cdot}...{\cdot}(2n-1){\cdot}\sigma^{2n} \left(\frac{1/2(1/2-1)...(1/2-n+1)}{n!}\right)\left(\frac{\alpha}{\tau_0^4}\right)^n\right) \tag{B.5}$$

$$\mathscr{E}(\tau) = \tau_0 \left(\sum_{n=0}^{\infty} c_n \frac{\alpha^n}{\tau_0^4 n}\right) \tag{B.6}$$

with the coefficients:

$$c_0 = 1; \quad c_1 = 8(ln2)^2 \frac{\sigma^2}{\tau_0^4}; \quad c_2 = -6{\cdot}16(ln2)^4 \frac{\sigma^4}{\tau_0^8}; \quad c_3 = ...; \tag{B.7}$$

or

$$\tau = \tau_0 + 3.88 \frac{\sigma^2}{\tau_0^3} - 22.16 \frac{\sigma^4}{\tau_0^8} + ... \tag{B.8}$$

Example: Assuming a 300 as long Gaussian and a phase noise of $\sigma = 10000$ as^2. Then τ can be written as:

$$\tau = \tau_0 + \underbrace{3.88 \frac{\sigma^2}{\tau_0^3}}_{14as} - \underbrace{22.16 \frac{\sigma^4}{\tau_0^8}}_{<10^{-6}} + ... = 314as \tag{B.9}$$

This is in perfect agreement with numerical simulations as performed in section 2.1.3.

Appendix C

Snell's and Fresnel law; R and T of a multilayer stack

There are different approaches on how to derive both Snell's law and the Fresnel coefficients. In the following the approach via the powerful Maxwell's equations [34] is chosen. It is based on simple continuity considerations of electromagnetic waves at interfaces. Those formulas will be necessary bases for both the reflectivity R and the transmission T of a multilayer stack in section C.

The Model: Here I refer to the notation of figure C.1. Basis of the following deduction is a two layer stack. Different from the usual approach, the
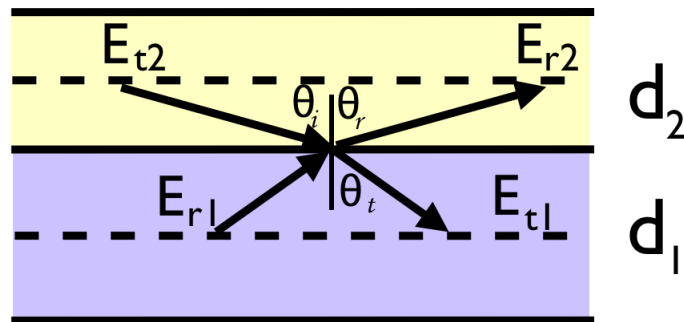
Figure C.1: Schematic model of two layers forming an interface.

individual electric field amplitudes E_{t1}, E_{t2}, E_{r1} and E_{r2} are here defined at the center of each layer. The resultant Fresnel equations are identical to the commonly used ones, but this way simplifies the later deduction of the recursive formula for R and T of a multilayer stack of arbitrary design.

The following calculations are based on the separation of the parallel and

the perpendicular wave vector parts:

$$k_{a\parallel} = \frac{2\pi}{\lambda}\tilde{n}_a sin\theta_a \qquad \text{and} \qquad k_{a\perp} = \frac{2\pi}{\lambda}\tilde{n}_a cos\theta_a \qquad (C.1)$$

Snell's law

From the fact that the incident i, the transmitted t and the reflected r light at an interface propagate within the same plane, one can write down the following relation for the modulus of the parallel field component $k_{a\parallel}$ with $a \in [i, t, r]$:

$$k_{i\parallel} = k_{r\parallel} = k_{t\parallel} \qquad (C.2)$$

Utilizing further, that the reflected beam propagates in the same material as the incidence beam ($\tilde{n}_r = \tilde{n}_i$) we can can rewrite upper equation in terms of the refractive index $\tilde{n}$ leading to *Snell's law*:

$$\theta_r = \theta_i \qquad \text{and} \qquad \tilde{n}_t sin\theta_t = \tilde{n}_i sin\theta_i \qquad (C.3)$$

Fresnel coefficients

The Fresnel coefficients can be retrieved by claiming continuity of the perpendicular field components and are take a different form for s and p polarisation. In the following only the retrieval for s polarized light is being shown. An analogue retrieval for p polarization is straight forward.

In figure C.1 two layers with the appropriate optical constants $\tilde{n}_1$ $\tilde{n}_2$ and appropriate thicknesses d_1 and d_2 form a common interface. Here we assume a monochromatic s-polarized plane waves (equation 2.19) propagating under an angle θ towards the surface. The propagating beams are fully characterized by their amplitudes E_a at the center of each layer and by the appropriate wave-vector k_a ($a \in [1, 2]$). Propagation from the center of each layer to the interface is summarized by the coefficients C_a:

$$C_a = exp(ik_{a\perp}\frac{d_a}{2}) \qquad (C.4)$$

$k_{a\perp}$ (eq. C.1) is the perpendicular component of the absolute value of light propagating under an angle θ_a.

Claiming continuity of the parallel field components [1] as well as continuity of the magnetic fields [2] one finds the equations for the electric fields which

---

[1]

$$E_{t_2}C_2 + E_{r_2}C_2^{-1} = E_{t_1}C_1^{-1} + E_{r_1}C_1 \qquad (C.5)$$

[2]

$$k_2(E_{t_2}C_2 - E_{r_2}C_2^{-1}) = k_1(E_{t_1}C_1^{-1} - E_{r_1}C_1) \qquad (C.6)$$

contains the Fresnel coefficients $r_{a,b}$ and $t_{a,b}$ with $a, b \in \{1, 2\}$:

$$E_{r_1} = r_{1,2}E_{t_1} + t_{2,1}C_2^{-1}C_1^{-1}E_{r_2} \quad \text{and} \quad E_{t_2} = t_{1,2}C_1C_2E_{t_1} + r_{2,1}E_{r_2} \quad \text{(C.7)}$$

The Fresnel coefficients occur as follows:

$$r_{1,2} = \frac{q_1 - q_2}{q_1 + q_2} = -r_{2,1} \quad \text{(C.8)}$$

$$t_{1,2} = \frac{2q_1}{q_1 + q_2} \quad \text{(C.9)}$$

One finds the same form of the Fresnel equation for both s and p polarisation, but with different coefficients q_a: In the case of s-polarisation q_a is identical to the perpendicular component of the wave vector $q_a^s = k_{a\perp}$. Equivalent continuity considerations for p-polarisation lead to the identical expressions to equations 2.27 but with slightly different coefficients: $q_a^p = cos\theta_a/\tilde{n}_a$. The Fresnel coefficients generally describe the transmitted and the reflected field amplitude for any linear homogeneous and non-magnetic medium.

R and T of an arbitrary multilayer stack

In this section a recursive formula for the reflectivity of a multilayer mirror is deduced. This retrieval is based on the Fresnel coefficients retrieved above. Again the notation of the previous section (figure C.1) is used and the transmitted and the reflected field amplitudes are defined at the center of each layer. The Fresnel equations C.7 describe the field amplitudes of the transmitted E_{t_2} and the reflected E_{r_1} waves in dependency on the amplitudes of the incoming radiation penetrating an interface from both sides.

Just by rewriting the equation C.7 one finds:

$$\tilde{r}_2 = r_{2,1} + t_{2,1}t_{1,2}\frac{\tilde{r}_1}{1 - \tilde{r}_1 r_{1,2}} \quad \text{(C.10)}$$

with Fresnel coefficients (e.g. $r_{1,2}$ or $t_{1,2}$) and amplitude reflectivity

$$\tilde{r}_a = C_a^2 E_{r_a}/E_{t_a} \quad \text{(C.11)}$$

and the (propagation) coefficients C_a as defined in equation C.4.

This is recursive formula allows one to calculate the reflectivity of a single thin film $\tilde{r}_2$ from the reflectivity defined by its bottom interface $\tilde{r}_1$ and the appropriate Fresnel coefficients: $r_{2,1}$, $r_{1,2}$, $t_{2,1}$, $t_{1,2}$.

To even simplify this relation using the following relation which can be verified from the Fresnel equations:

$$t_{1,2}t_{2,1} = 1 - r_{1,2}^2 \tag{C.12}$$

Rewriting equation C.10 one finds:

$$\tilde{r}_2 = \frac{r_{2,1} + \tilde{r}_1}{1 + r_{2,1}\tilde{r}_1} \tag{C.13}$$

This formula holds not only for a single interface, but can be rewritten for a the nth layer in a multilayer stack. Thereby the reflectivity amplitude in the nth layer (equation C.11) can be written in dependence on the reflectivity in the $(n-1)$th layer (equation C.13):

$$\tilde{r}_n = \frac{r_{n,n-1} + \tilde{r}_{n-1}}{1 + r_{n,n-1}\tilde{r}_{n-1}} \tag{C.14}$$

Here variables $r_{n,n-1}$ and $t_{n,n-1}$ are the Fresnel coefficients (eq. 2.27) of the interface between the nth and the $n-1$th layer. This equation allows us to recursively calculate the reflectivity amplitude $\tilde{r}_n$ of the nth layer in a multilayer stack from the single interface reflectivity $r_{n-1,n}$ on its top and the reflectivity on its bottom $\tilde{r}_{n-1}$. In the first layer, the reflectivity of the underlying stack is just given by the Fresnel coefficient formed by the substrate and the first layer.

Please note that the reflectivity of a mirror is defined by the reflected intensity, thereby the propagation coefficients C_a are eliminated and one finds the same result as if the electric field where not defined in the center of a layer, but just above the interface: $R_n = |\tilde{r}_n|^2 = |r_n|^2$. In the calculation of a multilayer stack, an infinitesimal small air layer can be assumed on top to also retrieve the spectral phase of a multilayer, which is defined just above the top layer, correctly.

An analogue expression can be formulated for the transmitted field amplitude:

$$E_{t_n} = \frac{1 - \tilde{r}_{n-1}r_{n-1,n}}{t_{n-1,n}} E_{t_n-1}. \tag{C.15}$$

Appendix D

Double period reflectivity of a 3(2)-material stack

In this section the reflectivity of two periods of a periodic two material stack is compared to that of a periodic three material stack. The goal is to analytically prove that a third material within one period can enlarge the reflectivity. As will be proven the two-dimensionality of XUV optical constants enables an improvement.

Definitions

Assuming the Bragg condition (equation 2.29) is fulfilled in a normal incidence periodic multilayer stack, then the optical length of two periods fit the wavelength of the incoming light, similar to the two-material case, where $d_3 = 0$:

$$\lambda/2 = d_1 n_1 + d_2 n_2 + d_3 n_3 \qquad (D.1)$$

We define three different γ_j with $j \in [1, 2, 3]$ in the case of a three material stack as the ration of a distinct layer thickness to the period: $\gamma_j = \frac{d_j}{period}$.
The phase-shift ϕ_i between the top and the bottom interface of layer i can be expressed in terms of γ_i, its thickness d_i, its refractive index n_i, the propagation angle θ_i and the diffraction order m:

$$\phi_i = \frac{2\pi}{\lambda} cos(\theta_i) d_i n_i = \pi m \gamma_i \qquad (D.2)$$

Fresnel relations

The reflectivity of a single interface between two arbitrary materials a and b is given by the simplified Fresnel formulas (equations 2.27).

$$r_{ab} = \frac{\tilde{n}_a - \tilde{n}_b}{\tilde{n}_a + \tilde{n}_b} = -r_{ba} \qquad (D.3)$$

For a periodic three material stack it is easy to proove again from the Fesnel fomulas 2.27 that

$$r_{cb} = -\frac{r_{ca} + r_{ab}}{1 + r_{ca}r_{ab}} \qquad (D.4)$$

In good approximation one can rewrite this equation, as the XUV single layer reflectivities r_{ca}, r_{ab} and r_{bc} are much smaller than 1.

$$r_{cb} \approx -(r_{ca} + r_{ab}) \qquad (D.5)$$

3 material 2-period reflectivity

Recursive usage of the single interface Fresnel relations together with upper equations D.3 and D.5 and assuming that the Bragg condition is fulfilled (thus per period: $\frac{2\pi}{\lambda}\Sigma_{i=1}^{3}n_id_icos(\theta_i) = \pi$), one can write the 2-period reflectivity of a three material stack as:

$$R_{period^3} = r_{period^3}r_{period^3}^* = 16r_{32}^2 sin^2\phi_2 + 16r_{13}^2 sin^2\phi_1 +$$

$$+16[sin\phi_1 sin\phi_2 - 2Re(r_{32}r_{13}^*)cos(\phi_1 + \phi_2) - 2Im(r_{32}r_{13}^*)sin(\phi_1 + \phi_2)] \quad (D.6)$$

2 material 2-period reflectivity

In analogy to equation D.2 the phase shift in a 2 material stack that consists of the material 1' and 2' is $\phi_1' = \phi_1'(\gamma_1' = d_1'/period)$. The reflectivity of two periods can thus be written as:

$$R_{period^2} = 16r_{21'}^2 sin^2\phi_1' = 16r_{21'}^2 sin^2(\pi m\gamma_1') \qquad (D.7)$$

This value is maximum for $\gamma_1' = 0.5$, leading to:

$$R_{period^2} = 16r_{21'}^2 \qquad (D.8)$$

Reflectivity increase due to a third material

Comparing the upper results, equation D.5 can be reformulated for a relation between the 2 material and the 3 material 2-period reflectivity:

$$R_{period^2} = 16r_{21}^2 =_{eq.[D.5]} 16(-(r_{32} + r_{13}))^2 \qquad (D.9)$$

Rewriting equation D.6 and subtracting the two layer reflectivity reduces our problem to the question if the three material reflectivity can be larger than the two material reflectivity: $R_{period^3} - R_{period^2} \geq 0$. The left hand side of this equation can be written as:

$$R_{period^3} - R_{period^2} = 16\underbrace{r_{32}^2(sin^2\phi_2 - 1)}_{A} + 16\underbrace{r_{13}^2(sin^2\phi_1 - 1)}_{B} +$$

$$+32[\underbrace{-Re(r_{32}r_{13}^*)(sin\phi_1 sin\phi_2 cos(\phi_1 + \phi_2) + 1)}_{C} -$$

$$\underbrace{-Im(r_{32}r_{13}^*)sin\phi_1 sin\phi_2 sin(\phi_1 + \phi_2)}_{D}] \qquad (D.10)$$

A net positive sum of all four terms on the right hand side of equation eq. D.10 would thus mean an increased reflectivity in the three materials case per period.

Interpretation

As expected one finds that the gain is dependent on the index of refraction of the individual materials: A and B are negative for any possible r_{32} and r_{13}, thus there is no gain possible from those coefficients. The sign of C and D depends on the refractice indices.
Both $\tilde{n}_1$, $\tilde{n}_2$, $\tilde{n}_3$ and r_{32} and r_{13} are complex in the XUV and soft x-ray region. Therefore both C and D can be positive and also exceed the negative summands A and B. Thus the reflectivity of a three material periodic stack *can be larger* than that of a two material periodic stack!

No gain by a third material for 1-D optical constants

Equation D.10 also proves, that there is no possible gain in reflectivity from a third material in visible spectral range multilayers. Here, coating materials can be chosen such that they are not absorbing., Therefore the index of refraction is pure real. If n_1, n_2 and n_3 are real, then also all Fresnel coefficients $r_{i,j}$ are real (equation 2.27). There are only two constellations of interest. All other constellations repeat themselves in one of those:
1.$n_1 < n_3 < n_2$
2.$n_1 > n_3 > n_2$
r_{32} and r_{13} have always the same sign, due to their definition (equation 2.27), so $r_{32}r_{13}^*$ is positive and real in any case, thus C is negative as well and D vanishes as $Im(r_{32}r_{13}^*) = 0$. We have already seen that the coefficients A and B in relation D.10 are negative as well for any constellation. Thus in the visible and infrared case, a third material in the stack stack will never yield a higher refectivity compared to its appropriate two material stack.

Appendix E

Fitting reflectivity data by simulated annealing

For a final retrieval of the structure of the produced mirrors, meaning a retrieval of the deposition rates or the investigation of the formed interlayers or thickness loss due to period contraction, a fit of the measured XRR and XUV reflectivity curves is required. Beside that, also the transfer of mirror design to deposition times, including all losses requires an appropriate computer program.

A self-written Fresnel code has been developed for the multilayer reflectivity simulation, based on the recursive code presented in section C. This code allows to calculate the reflectivity and the transmission as well as the phase, the GD and the GDD for any arbitrary stack design and any material combination and wavelength (assuming that the material optical constants are known) both in dependency of the wavelength and the measurement angle.

A subroutine has been developed which accounts for realistic interfaces. Here the original design is converted into a realistic model and thickness loss per period as well as the formation of $MoSi_2$ interlayers and the subsequential structural changes are included in this transform. Starting with a new material combination requires as well inverse engineering. Thus also the sputter-times can be converted into an expected reflectivity curve, in dependency of the deposition rates.

For a periodic stack those parameters are the period d, the ration of (bottom later thickness)/period γ and the Nevot-Croce roughness σ. Also the thickness of the interlayers can be used as fit parameter in the random walk Fresnel fit routine. Beside that averaging/acceptance angle $\Delta\Phi$ can be of interest when fitting an XRR measurement. All fit parameters can be chosen by the user at the beginning of a fit process.

A Simulated annealing random walk algorithm is used for the fit. Each fit consists of N iterations. Per step, one or more of the wanted mirror parameters

are changed and the figure of merit is calculated as the (logarithmic) difference between the simulated and the measured data points. Per iteration k the following steps are performed:

- The temperature of the system is decreased linearily: $T(k) = 1 - k/N$

- With a certain probability P the wanted parameters X are varied according to the system temperature $T(k)$ and a user defined step size ΔX within certain user defined boundaries using two quasi random generated numbers $rand1$ and $rand2$:

$$if(rand1 < P)X = X \pm \Delta X {\cdot} T(k) {\cdot} rand2;$$

- The design and the reflectivity of the mirror is calculated using the new parameters.

- The figure of merit is calculated for the simulated S and the measured M data, according to:

$$merit = (log(S) - log(M))^2$$

- Accept the changed parameters

  1. always, if the figure of merit is smaller than the current figure.

  2. with a certain propability $T(k) * \tilde{P}$ if the figure of merit is larger. This step is important to avoid being captured in local minima.

Finally after N iterations the parameter set with the lowest figure of merit is returned.

Appendix F

45 degree beam line setup- AS2

Here now the $AS2$ beamline set-up is introduced. This beamline stands out by the spatial separation of the XUV and the laser beam in contrast to the usual collinear set-up. As will be explained in the following, one key component here is the flat 45 degree XUV mirror in this set-up. The chirped attosecond pulse generation campaign has been measured in particular at the $AS2$ (section 4.3). Figure F.1 has been taken from [35].
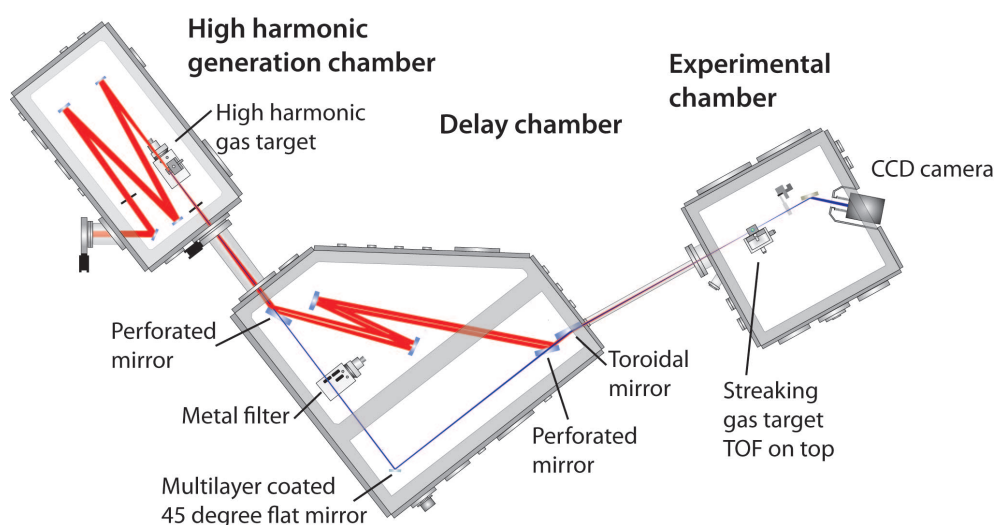
Figure F.1: Experimental set-up of a 45 degree attosecond beamline setup.

After the HHG, the XUV beam is spatially separated from the laser by means of a perforated mirror utilizing its lower divergence. While the XUV beam is guided through the mirror hole, part of the laser beam is reflected at the mirror. After several reflections, the two beam paths are merged at the end of the delay chamber again by a second perforated mirror. Both beams are focused just after they are brought together by a focusing parabola into a gas target for streaking.

Following the *XUV* beam inside the delay chamber, a thin metal filter functions in addition to the 45 degree *XUV* mirror as pulse shaping element and filters the laser beam from the *XUV* radiation.

In this set-up, the laser pulse is delayed on its way in respect to the attosecond pulse. Thus, focusing of the *XUV* radiation (by means of a grazing incidence parabola) and time delay introduction between the *XUV* and the laser pulse (by means of a delay stage in the optical beam path) is decoupled from the plane *XUV* multilayer mirror in this setup.

The delay between the two beams is a crucial value. An interferometric beam stabilization had to be implemented to ensure constant traveling paths. But once this is implemented, this beam-line enables a complete new sort of measurements due to te spatial separation and thus the possibility of independent shaping of the laser and the *XUV* beam.

Bibliography

[1] A. Scrinzi, M. Y. Ivanov, R. Kienberger, and D. M. Villeneuve, "Attosecond physics," J. Phys. B-At. Mol. Opt. **39,** R1–R37 (2006).

[2] F. Krausz and M. Ivanov, "Attosecond physics," Rev. Mod. Phys. **81,** 163–234 (2009).

[3] M. Schultze, M. Fieß, N. Karpowicz, J. Gagnon, M. Korbman, M. Hofstetter, S. Neppl, A. L. Cavalieri, Y. Komninos, T. Mercouris, C. A. Nicolaides, R. Pazourek, S. Nagele, J. Feist, J. Burgdörfer, A. M. Azzeer, R. Ernstorfer, R. Kienberger, U. Kleineberg, E. Goulielmakis, F. Krausz, and V. S. Yakovlev, "Delay in Photoemission," Science **328,** 1658–1662 (2010).

[4] M. Uiberacker, T. Uphues, M. Schultze, A. J. Verhoef, V. Yakovlev, M. F. Kling, J. Rauschenberger, N. M. Kabachnik, H. Schroder, M. Lezius, K. L. Kompa, H. G. Muller, M. J. J. Vrakking, S. Hendel, U. Kleineberg, U. Heinzmann, M. Drescher, and F. Krausz, "Attosecond real-time observation of electron tunnelling in atoms," Nature **446,** 627–632 (2007).

[5] A. L. Cavalieri, N. Müller, T. Uphues, V. S. Yakovlev, A. Baltuška, B. Horvath, B. Schmidt, L. Blümel, R. Holzwarth, S. Hendel, M. Drescher, U. Kleineberg, P. M. Echenique, R. Kienberger, F. Krausz, and U. Heinzmann, "Attosecond spectroscopy in condensed matter," Nature **449,** 1029–1032 (2007).

[6] T. Uphues, M. Schultze, M. F. Kling, M. Uiberacker, S. Hendel, U. Heinzmann, N. M. Kabachnik, and M. Drescher, "Ion-charge-state chronoscopy of cascaded atomic Auger decay," New J. Phys. **10,** 025009 (2008).

[7] M. I. Stockman, M. F. Kling, U. Kleineberg, and F. Krausz, "Attosecond nanoplasmonic-field microscope," Nat. Photon. **1,** 539–544 (2007).

[8] P. A. M. Dirac, "The Quantum Theory of the Emission and Absorption of Radiation," P. R. Soc. Lond. A-Conta. **114,** 243–265 (1927).

[9] E. Fermi, *Nuclear Physics* (University of Chicago Press, 1950).

[10] D. Attwood, *Soft X-Rays and Extreme Ultraviolet Radiation: Principles and Applications* (Cambridge University Press, 2007).

[11] A. Wonisch, U. Neuhäusler, N. M. Kabachnik, T. Uphues, M. Uiberacker, V. Yakovlev, F. Krausz, M. Drescher, U. Kleineberg, and U. Heinzmann, "Design, fabrication, and analysis of chirped multilayer mirrors for reflection of extreme-ultraviolet attosecond pulses," Appl. Opt. **45,** 4147–4156 (2006).

[12] A.-S. Morlens, P. Balcou, P. Zeitoun, C. Valentin, V. Laude, and S. Kazamias, "Compression of attosecond harmonic pulses by extreme-ultraviolet chirped mirrors," Opt. Lett. **30,** 1554–1556 (2005).

[13] M. Suman, G. Monaco, M.-G. Pelizzo, D. L. Windt, and P. Nicolosi, "Realization and characterization of an XUVmultilayer coating for attosecond pulses," Opt. Express **17,** 7922–7932 (2009).

[14] I. P. Christov, M. M. Murnane, and H. C. Kapteyn, "High-Harmonic Generation of Attosecond Pulses in the "Single-Cycle" Regime," Phys. Rev. Lett. **78,** 1251 (1997).

[15] M. Hentschel, R. Kienberger, C. Spielmann, G. A. Reider, N. Milosevic, T. Brabec, P. Corkum, U. Heinzmann, M. Drescher, and F. Krausz, "Attosecond metrology," Nature **414,** 509–513 (2001).

[16] R. Kienberger, E. Goulielmakis, M. Uiberacker, A. Baltuska, V. Yakovlev, F. Bammer, A. Scrinzi, T. Westerwalbesloh, U. Kleineberg, U. Heinzmann, M. Drescher, and F. Krausz, "Atomic transient recorder," Nature **427,** 817–821 (2004).

[17] E. Goulielmakis, M. Uiberacker, R. Kienberger, A. Baltuska, V. Yakovlev, A. Scrinzi, T. Westerwalbesloh, U. Kleineberg, U. Heinzmann, M. Drescher, and F. Krausz, "Direct Measurement of Light Waves," Science **305,** 1267–1269 (2004).

[18] R. Kienberger, M. Hentschel, M. Uiberacker, C. Spielmann, M. Kitzler, A. Scrinzi, M. Wieland, T. Westerwalbesloh, U. Kleineberg, U. Heinzmann, M. Drescher, and F. Krausz, "Steering Attosecond Electron Wave Packets with Light," Science **297,** 1144–1148 (2002).

[19] E. Goulielmakis, M. Schultze, M. Hofstetter, V. S. Yakovlev, J. Gagnon, M. Uiberacker, A. L. Aquila, E. M. Gullikson, D. T. Attwood, R. Kienberger, F. Krausz, and U. Kleineberg, "Single-Cycle Nonlinear Optics," Science **320,** 1614–1617 (2008).

[20] F. Krausz, "Photonics I,", http://www.attoworld.de/Home/academics/ EducationAndTraining/PhotonicsI/index.html (2011).

[21] W. Heisenberg, "Über den anschaulichen Inhalt der quantentheoretischen Kinematik und Mechanik," Z. Phys. A-Hadron Nucl. **43,** 172–198 (1927), 10.1007/BF01397280.

[22] J.-C. Diels and W. Rudolph, *Ultrashort Laser Pulse Phenomena: Fundamentals, Techniques, and Applications on a Femtosecond Time Scale, Optics and Photonics* (Academic Press Inc, 2006).

[23] A. V. Tikhonravov, M. K. Trubetskov, and G. W. DeBell, "Optical coating design approaches based on the needle optimization technique," Appl. Opt. **46,** 704–710 (2007).

[24] V. S. Yakovlev, J. Gagnon, N. Karpowicz, and F. Krausz, "Attosecond Streaking Enables the Measurement of Quantum Phase," Phys. Rev. Lett. **105,** 073001 (2010).

[25] W. Chao, J. Kim, S. Rekawa, P. Fischer, and E. H. Anderson, "Demonstration of 12 nm Resolution Fresnel Zone Plate Lens based Soft X-ray Microscopy," Opt. Express **17,** 17669–17677 (2009).

[26] A. C. Thompson, D. T. Attwood, E. M.Gullikson, M. R. Howells, J. B. Kortright, A. L. Robinson, J. H. Underwood, K.-J. Kim, J. Kirz, I. Lindau, P. Pianetta, H. Winick, G. P. Williams, and J. H. Scofield, *X-Ray Data Booklet*, 3 ed. (Lawrence Berkeley National Laboratory University of California Berkeley, California 94720, 2009).

[27] G. Vaschenko, C. Brewer, F. Brizuela, Y. Wang, M. A. Larotonda, B. M. Luther, M. C. Marconi, J. J. Rocca, C. S. Menoni, E. H. Anderson, W. Chao, B. D. Harteneck, J. A. Liddle, Y. Liu, and D. T. Attwood, "Sub-38 nm resolution tabletop microscopy with 13 nm wavelength laser light," Opt. Lett. **31,** 1214–1216 (2006).

[28] T. Haga, H. Kinoshita, K. Hamamoto, S. Takada, N. Kazui, S. Kakunai, H. Tsubakino, and T. Watanabe, "Evaluation of Finished Extreme Ultraviolet Lithography (EUVL) Masks Using a EUV Microscope," Jpn. J. Appl. Phys. **42,** 3771–3775 (2003).

[29] C. Wagner and N. Harned, "EUV lithography: Lithography gets extreme," Nat. Photon. **4,** 24–26 (2010).

[30] P. Emma *et al.*, "First lasing and operation of an ångstrom-wavelength free-electron laser," Nat. Photon. **4,** 641–647 (2010).

[31] W. Helml, A. Maier, and R. Kienberger, 2011, private communication.

[32] P. Tzallas, D. Charalambidis, N. A. Papadogiannis, K. Witte, and G. D. Tsakiris, "Direct observation of attosecond light bunching," Nature **426,** 267–271 (2003).

[33] E. Spiller, *Soft X-ray optics* (SPIE Optical Engineering Press, Bellingham, Wash., USA, 1994), .

[34] J. C. Maxwell, "A Dynamical Theory of the Electromagnetic Field," Royal Society Transactions **CLV,** 459 (1865).

[35] M. Fieß, M. Schultze, E. Goulielmakis, B. Dennhardt, J. Gagnon, M. Hofstetter, R. Kienberger, and F. Krausz, "Versatile apparatus for attosecond metrology and spectroscopy," Rev. Sci. Instrum. **81,** 093103 (2010).

[36] C. Montcalm, S. Bajt, P. B. Mirkarimi, E. A. Spiller, F. J. Weber, and J. A. Folta, "Multilayer reflective coatings for extreme-ultraviolet lithography," P. Soc. Photo-Opt. Ins. **3331,** 42–51 (1998).

[37] E. Spiller, "Reflective multilayer coatings for the far uv region," Appl. Opt. **15,** 2333–2338 (1976).

[38] V. Yakovlev and G. Tempea, "Optimization of Chirped Mirrors," Appl. Opt. **41,** 6514–6520 (2002).

[39] M. Trubetskov, A. Tikhonravov, and V. Pervak, "Time-domain approach for designing dispersive mirrors based on the needle optimization technique. Theory.," Opt. Express **16,** 20637–20647 (2008).

[40] F. Eriksson, N. Ghafoor, F. Schäfers, E. M. Gullikson, S. Aouadi, S. Rohde, L. Hultman, and J. Birch, "Atomic scale interface engineering by modulated ion-assisted deposition applied to soft x-ray multilayer optics," Appl. Opt. **47,** 4196–4204 (2008).

[41] C. W. Gwyn, R. Stulen, D. Sweeney, and D. Attwood, "Extreme ultraviolet lithography," Papers from the 42nd international conference on electron, ion, and photon beam technology and nanofabrication **16,** 3142–3149 (1998).

[42] D. S. Martinez-Galarce, A. B. C. WalkerII, D. B. Gore, C. C. Kankelborg, R. B. Hoover, J. T. W. Barbee, and P. F. X. Boerner, "High resolution imaging with multilayer telescopes: resolution performance of the MSSTA II telescopes," Opt. Eng. **39,** 1063–1079 (2000).

[43] T. Yamazaki, Y. Takizawa, H. Kunieda, K. Yamashita, K. Ikeda, K. Misaki, M. Nakamura, I. Yoshikawa, and A. Yamaguchi, "Normal incidence multilayer telescope for galactic EUV observation," J. Electron Spectrosc. Relat. Phenom. **80,** 299 – 302 (1996), proceedings of the 11th International Conference on Vacuum Ultraviolet Radiation Physics.

[44] F. Schäfers, H.-C. Mertins, A. Gaupp, W. Gudat, M. Mertin, I. Packe, F. Schmolla, S. D. Fonzo, G. Soullié, W. Jark, R. Walker, X. L. Cann, R. Nyholm, and M. Eriksson, "Soft-X-Ray Polarimeter with Multilayer Optics: Complete Analysis of the Polarization State of Light," Appl. Opt. **38,** 4074–4088 (1999).

[45] J. M. André, R. Benbalagh, R. Barchewitz, M. F. Ravet, A. Raynal, F. Delmotte, F. Bridou, G. Julié, A. Bosseboeuf, R. Laval, G. Soullié, C. Rémond, and M. Fialin, "X-ray Multilayer Monochromator with Enhanced Performance," Appl. Opt. **41,** 239–244 (2002).

[46] A. Wonisch, T. Westerwalbesloh, W. Hachmann, N. Kabachnik, U. Kleineberg, and U. Heinzmann, "Aperiodic nanometer multilayer systems as optical key components for attosecond electron spectroscopy," Thin Solid Films **464-465,** 473 – 477 (2004), proceedings of the 7th International Symposium on Atomically Controlled Surfaces, Interfaces and Nanostructures.

[47] M. Schultze, E. Goulielmakis, M. Uiberacker, M. Hofstetter, J. Kim, D. Kim, F. Krausz, and U. Kleineberg, "Powerful 170-attosecond XUV pulses generated with few-cycle laser pulses and broadband multilayer optics," New J. Phys. **9,** 243 (2007).

[48] J. H. Underwood and J. T. W. Barbee, "Layered synthetic microstructures as Bragg diffractors for X rays and extreme ultraviolet: theory and predicted performance," Appl. Opt. **20,** 3027–3034 (1981).

[49] P. Lee, "X-ray diffraction in multilayers," Opt. Commun. **37,** 159 – 164 (1981).

[50] F. Erikson, Ph.D. thesis, Linköping University, 581 83 Linköping, Sweden, 2004.

[51] U. Kleineberg, H.-J. Stock, A. Kloidt, Schmiedeskamp, B., U. Heinzmann, S. Hopfe, and R. Scholz, "Interface Stability and Silicide Formation in High Temperature Stable MoxSi1 - x/Si Multilayer Soft X - Ray Mirrors Studied by Means of X-Ray Diffraction and HRTEM," physica status solidi **145,** 539–550 (1994).

[52] A. L. Aquila, F. Salmassi, F. Dollar, Y. Liu, and E. Gullikson, "Developments in realistic design for aperiodic Mo/Si multilayer mirrors," Opt. Express **14,** 10073–10078 (2006).

[53] P. Debye, "Interferenz von Röntgenstrahlen und Wärmebewegung," Ankündigung. d. Phys. 348 (1913).

[54] I. Waller, "Zur Frage der Einwirkung der Wärmebewegung auf die Interferenz von Röntgenstrahlen," Z. Phys. A-Hadron Nucl. **17,** 398–408 (1923), 10.1007/BF01328696.

[55] A. Aquila, F. Salmassi, Y. Liu, and E. Gullikson, "Tri-material multilayer coatings with high reflectivity and wide bandwidth for 25 to 50 nm extreme ultraviolet light," Opt. Express **17,** 22102–22107 (2009).

[56] A.-S. Morlens, R. López-Martens, O. Boyko, P. Zeitoun, P. Balcou, K. Varjú, E. Gustafsson, T. Remetter, A. L'Huillier, S. Kazamias, J. Gautier, F. Delmotte, and M.-F. Ravet, "Design and characterization of extreme-ultraviolet broadband mirrors for attosecond science," Opt. Lett. **31,** 1558–1560 (2006).

[57] M. Hofstetter, M. Schultze, M. Fieß, B. Dennhardt, A. Guggenmos, J. Gagnon, V. S. Yakovlev, E. Goulielmakis, R. Kienberger, E. M. Gullikson, F. Krausz, and U. Kleineberg, "Attosecond dispersion control by extreme ultraviolet multilayer mirrors," Opt. Express **19,** 1767–1776 (2011).

[58] A. Aquila, F. Salmassi, and E. Gullikson, "Metrologies for the phase characterization of attosecond extreme ultraviolet optics," Opt. Lett. **33,** 455–457 (2008).

[59] V. Pervak, A. Tikhonravov, M. Trubetskov, S. Naumov, F. Krausz, and A. Apolonski, "1.5-octave chirped mirror for pulse compression down to sub-3 fs," Appl. Phys. B-Lasers O. **87,** 5–12 (2007).

[60] A. Aquila, Ph.D. thesis, University of California Berkeley, 2009.

[61] E. Gustafsson, T. Ruchon, M. Swoboda, T. Remetter, E. Pourtal, R. López-Martens, P. Balcou, and A. L'Huillier, "Broadband attosecond pulse shaping," Opt. Lett. **32,** 1353–1355 (2007).

[62] R. López-Martens, K. Varjú, P. Johnsson, J. Mauritsson, Y. Mairesse, P. Salières, M. B. Gaarde, K. J. Schafer, A. Persson, S. Svanberg, C.-G. Wahlström, and A. L'Huillier, "Amplitude and Phase Control of Attosecond Light Pulses," Phys. Rev. Lett. **94,** 033001 (2005).

[63] G. Sansone, E. Benedetti, F. Calegari, C. Vozzi, L. Avaldi, R. Flammini, L. Poletto, P. Villoresi, C. Altucci, R. Velotta, S. Stagira, S. De Silvestri, and M. Nisoli, "Isolated Single-Cycle Attosecond Pulses," Science **314,** 443–446 (2006).

[64] E. M. Gullikson, "CXRO-webpage: http://www.cxro.lbl.gov/,".

[65] T. H. Maiman, "Stimulated Optical Radiation in Ruby," Nature **187,** 493–494 (1960).

[66] R. W. Hellwarth, "Theory of the Pulsation of Fluorescent Light From Ruby," Phys. Rev. Lett. **6,** 9 (1961).

[67] D. E. Spence, P. N. Kean, and W. Sibbett, "60-fsec pulse generation from a self-mode-locked Ti:sapphire laser," Opt. Lett. **16,** 42–44 (1991).

[68] T. Brabec, C. Spielmann, P. F. Curley, and F. Krausz, "Kerr lens mode locking," Opt. Lett. **17,** 1292–1294 (1992).

[69] D. Strickland and G. Mourou, "Compression of amplified chirped optical pulses," Opt. Commun. **56,** 219 – 221 (1985).

[70] J. K. Ranka, R. S. Windeler, and A. J. Stentz, "Visible continuum generation in air-silica microstructure optical fibers with anomalous dispersion at 800 nm," Opt. Lett. **25,** 25–27 (2000).

[71] N. Karasawa, R. Morita, H. Shigekawa, and M. Yamashita, "Generation of intense ultrabroadband optical pulses by induced phase modulation in an argon-filled single-mode hollow waveguide," Opt. Lett. **25,** 183–185 (2000).

[72] B. Schenkel, J. Biegert, U. Keller, C. Vozzi, M. Nisoli, G. Sansone, S. Stagira, S. D. Silvestri, and O. Svelto, "Generation of 3.8-fs pulses from adaptive compression of a cascaded hollow fiber supercontinuum," Opt. Lett. **28,** 1987–1989 (2003).

[73] K. Yamane, T. Kito, R. Morita, and M. Yamashita, "2.8-fs clean single transform-limited optical-pulse generation and characterization," Ultrafast Phenomena XIV **79,** 13–15 (2005).

[74] A. L. Cavalieri, E. Goulielmakis, B. Horvath, W. Helml, M. Schultze, M. Fieß, V. Pervak, L. Veisz, V. S. Yakovlev, M. Uiberacker, A. Apolonski, F. Krausz, and R. Kienberger, "Intense 1.5-cycle near infrared laser waveforms and their use for the generation of ultra-broadband soft-x-ray harmonic continua," New J. Phys. **9,** 242,243 (2007).

[75] S. Koke, C. Grebing, H. Frei, A. Anderson, A. Assion, and G. Steinmeyer, "Direct frequency comb synthesis with arbitrary offset and shot-noise-limited phase noise," Nat. Photon 4 (2010).

[76] A. Baltuska, M. Uiberacker, E. Goulielmakis, R. Kienberger, V. Yakovlev, T. Udem, T. Hansch, and F. Krausz, "Phase-controlled amplification of few-cycle laser pulses," IEEE. J. Sel. Top. Quant **9,** 972 – 989 (2003).

[77] A. Einstein, "Zur Quantentheorie der Strahlung," Physikalische Zeitschrift 18 (1916).

[78] S. Khan, "FEMTOSLICING IN STORAGE RINGS," In *Proceedings of 2005 Particle Accelerator Conference, Knoxville, Tennessee*, (2005).

[79] F. Grüner, S. Becker, U. Schramm, T. Eichner, M. Fuchs, R. Weingartner, D. Habs, J. Meyer-ter Vehn, M. Geissler, M. Ferrario, L. Serafini, B. van der Geer, H. Backe, W. Lauth, and S. Reiche, "Design considerations for table-top, laser-based VUV and X-ray free electron lasers," Appl. Phys. B-Lasers O. **86,** 431–435 (2007), 10.1007/s00340-006-2565-7.

[80] M. Fuchs, R. Weingartner, A. Popp, Z. Major, S. Becker, J. Osterhoff, I. Cortrie, B. Zeitler, R. Horlein, G. D. Tsakiris, U. Schramm, T. P. Rowlands-Rees, S. M. Hooker, D. Habs, F. Krausz, S. Karsch, and F. Gruner, "Laser-driven soft-X-ray undulator source," Nat. Phys. **5,** 826–829 (2009).

[81] C. Rischel, A. Rousse, I. Uschmann, P.-A. Albouy, J.-P. Geindre, P. Audebert, J.-C. Gauthier, E. Froster, J.-L. Martin, and A. Antonetti, "Femtosecond time-resolved X-ray diffraction from laser-heated organic films," Nature **390,** 490–492 (1997).

[82] R. W. Schoenlein, W. P. Leemans, A. H. Chin, P. Volfbeyn, T. E. Glover, P. Balling, M. Zolotorev, K. J. Kim, S. Chattopadhyay, and C. V. Shank, "Femtosecond X-ray Pulses at 0.4 A Generated by 90ÂňâĹđ Thomson Scattering: A Tool for Probing the Structural Dynamics of Materials," Science **274,** 236–238 (1996).

[83] P. A. Franken, A. E. Hill, C. W. Peters, and G. Weinreich, "Generation of Optical Harmonics," Phys. Rev. Lett. **7,** 118–119 (1961).

[84] R. Hörlein, Y. Nomura, J. Osterhoff, Z. Major, S. Karsch, F. Krausz, and G. D. Tsakiris, "High harmonics from solid surfaces as a source of ultra-bright XUV radiation for experiments," Plasma Phys. Contr. F. **50,** 124002 (2008).

[85] D. H. Ko, K. T. Kim, J. Park, J. hwan Lee, and C. H. Nam, "Attosecond chirp compensation over broadband high-order harmonics to generate near transform-limited 63 as pulses," New J. Phys. **12,** 063008 (2010).

[86] M. Schultze, A. Wirth, I. Grguras, M. Uiberacker, T. Uphues, A. Verhoef, J. Gagnon, M. Hofstetter, U. Kleineberg, E. Goulielmakis, and F. Krausz, "State-of-the-art attosecond metrology," J. Electron Spectrosc. Relat. Phenom. **184,** 68 – 77 (2011), advances in Vacuum Ultraviolet and X-ray Physics, The 37th International Conference on Vacuum Ultraviolet and X-ray Physics (VUVX2010).

[87] B. Kim, J. An, Y. Yu, Y. Cheng, Z. Xu, and D. E. Kim, "Optimization of multi-cycle two-color laser fields for the generation of an isolated attosecond pulse," Opt. Express **16,** 10331–10340 (2008).

[88] M. Ferray, A. L'Huillier, X. F. Li, L. A. Lompre, G. Mainfray, and C. Manus, "Multiple-harmonic conversion of 1064 nm radiation in rare gases," J. Phys. B-At. Mol. Opt. **21,** L31–L35 (1988).

[89] C. Spielmann, N. H. Burnett, S. Sartania, R. Koppitsch, M. Schnurer, C. Kan, M. Lenzner, P. Wobrauschek, and F. Krausz, "Generation of Coherent X-rays in the Water Window Using 5-Femtosecond Laser Pulses," Science **278,** 661–664 (1997).

[90] E. A. Gibson, A. Paul, N. Wagner, R. Tobey, D. Gaudiosi, S. Backus, I. P. Christov, A. Aquila, E. M. Gullikson, D. T. Attwood, M. M. Murnane, and H. C. Kapteyn, "Coherent Soft X-ray Generation in the Water Window with Quasi-Phase Matching," Science **302,** 95–98 (2003).

[91] N. H. Burnett, H. A. Baldis, M. C. Richardson, and G. D. Enright, "Harmonic generation in CO(2) laser target interaction," Appl. Phys. Lett. **31,** 172–174 (1977).

[92] P. B. Corkum, "Plasma perspective on strong field multiphoton ionization," Phys. Rev. Lett. **71,** 1994–1997 (1993).

[93] M. Lewenstein, P. Balcou, M. Y. Ivanov, A. L'Huillier, and P. B. Corkum, "Theory of high-harmonic generation by low-frequency laser fields," Phys. Rev. A **49,** 2117–2132 (1994).

[94] R. Santra and A. Gordon, "Three-Step Model for High-Harmonic Generation in Many-Electron Systems," Phys. Rev. Lett. **96,** 073906 (2006).

[95] M. F. Kling and M. J. J. Vrakking, "Attosecond Electron Dynamics," Annual Review of Physical Chemistry **59,** 463–492 (2008).

[96] L. V. Keldysh, "Ionization in the field of a strong electromagnetic wave," Sov. Phys. JETP-USSR **20,** 1307–1314 (1965).

[97] P. Colosimo, G. Doumy, C. I. Blaga, J. Wheeler, C. Hauri, F. Catoire, J. Tate, R. Chirla, A. M. March, G. G. Paulus, H. G. Muller, P. Agostini, and L. F. DiMauro, "Scaling strong-field interactions towards the classical limit," Nat. Phys. **4,** 386–389 (2008).

[98] M. W. Walser, C. H. Keitel, A. Scrinzi, and T. Brabec, "High Harmonic Generation Beyond the Electric Dipole Approximation," Phys. Rev. Lett. **85,** 5082–5085 (2000).

[99] P. M. Paul, E. S. Toma, P. Breger, G. Mullot, F. AugâĹŽ©, P. Balcou, H. G. Muller, and P. Agostini, "Observation of a Train of Attosecond Pulses from High Harmonic Generation," Science **292,** 1689–1692 (2001).

[100] U. Teubner and P. Gibbon, "High-order harmonics from laser-irradiated plasma surfaces," Rev. Mod. Phys. **81,** 445–479 (2009).

[101] M. Fieß, Ph.D. thesis, Universität München, 2010.

[102] Y. Mairesse, A. de Bohan, L. J. Frasinski, H. Merdji, L. C. Dinu, P. Monchicourt, P. Breger, M. Kovacev, R. Taieb, B. Carre, H. G. Muller, P. Agostini, and P. Salieres, "Attosecond Synchronization of High-Harmonic Soft X-rays," Science **302,** 1540–1543 (2003).

[103] Y. Mairesse, A. de Bohan, L. J. Frasinski, H. Merdji, L. C. Dinu, P. Monchicourt, P. Breger, M. Kovačev, T. Auguste, B. Carré, H. G. Muller, P. Agostini, and P. Salières, "Optimization of Attosecond Pulse Generation," Phys. Rev. Lett. **93,** 163901 (2004).

[104] K. J. Schafer, B. Yang, L. F. DiMauro, and K. C. Kulander, "Above threshold ionization beyond the high harmonic cutoff," Phys. Rev. Lett. **70,** 1599–1602 (1993).

[105] V. V. Strelkov, A. F. Sterjantov, N. Y. Shubin, and V. T. Platonenko, "XUV generation with several-cycle laser pulse in barrier-suppression regime," J. Phys. B-At. Mol. Opt. **39,** 577 (2006).

[106] E. Goulielmakis, Z.-H. Loh, A. Wirth, R. Santra, N. Rohringer, V. S. Yakovlev, S. Zherebtsov, T. Pfeifer, A. M. Azzeer, M. F. Kling, S. R. Leone, and F. Krausz, "Real-time observation of valence electron motion," Nature **466,** 739–743 (2010).

[107] T. Pfeifer, M. J. Abel, P. M. Nagel, W. Boutu, M. J. Bell, Y. Liu, D. M. Neumark, and S. R. Leone, "Measurement and optimization of isolated attosecond pulse contrast," Opt. Lett. **34,** 1819–1821 (2009).

[108] E. Magerl, S. Neppl, A. L. Cavalieri, E. M. Bothschafter, M. Stanislawski, T. Uphues, M. Hofstetter, U. Kleineberg, J. V. Barth, D. Menzel, F. Krausz, R. Ernstorfer, R. Kienberger, and P. Feulner, "A flexible apparatus for attosecond photoelectron spectroscopy of solids and surfaces," Rev. Sci. Instrum. **82,** 063104 (2011).

[109] E. M. Bothschafter, A. Schiffrin, V. S. Yakovlev, A. M. Azzeer, and F. Krausz, "Collinear generation of ultrashort UV and XUV pulses," Opt. Express **18,** 9173–80 (2010).

[110] A. Baltuska, T. Udem, M. Uiberacker, M. Hentschel, E. Goulielmakis, C. Gohle, R. Holzwarth, V. Yakovlev, A. Scrinzi, T. Hansch, and F. Krausz, "Attosecond control of electronic processes by intense light fields," Nature **421,** 611–615 (2003).

[111] M. Drescher, M. Hentschel, R. Kienberger, M. Uiberacker, V. Yakovlev, A. Scrinzi, T. Westerwalbesloh, U. Kleineberg, U. Heinzmann, and F. Krausz, "Time-resolved atomic inner-shell spectroscopy," Nature **419,** 803–807 (2002).

[112] M. Hofstetter, M. Schultze, M. Fieß, A. Guggenmos, J. Gagnon, E. Magerl, E. Bothschafter, R. Ernstorfer, R. Kienberger, E. Gullikson, F. Krausz, and U. Kleineberg, "First Attosecond Pulse Control by Multilayer Mirrors above 100 eV Photon Energy," International Conference on Ultrafast Phenomena p. PDP8 (2010).

[113] A. Apolonski, A. Poppe, G. Tempea, C. Spielmann, T. Udem, R. Holzwarth, T. W. Hänsch, and F. Krausz, "Controlling the Phase Evolution of Few-Cycle Light Pulses," Phys. Rev. Lett. **85,** 740–743 (2000).

[114] N. G. Johnson, O. Herrwerth, A. Wirth, S. De, I. Ben-Itzhak, M. Lezius, B. Bergues, M. F. Kling, A. Senftleben, C. D. Schröter, R. Moshammer, J. Ullrich, K. J. Betsch, R. R. Jones, A. M. Sayler, T. Rathje, K. Rühle, W. Müller, and G. G. Paulus, "Single-shot carrier-envelope-phase-tagged ion-momentum imaging of nonsequential double ionization of argon in intense 4-fs laser fields," Phys. Rev. A **83,** 013412 (2011).

[115] V. S. Yakovlev and A. Scrinzi, "High Harmonic Imaging of Few-Cycle Laser Pulses," Phys. Rev. Lett. **91,** 153901 (2003).

[116] M. Yabashi, K. Tamasaku, and T. Ishikawa, "Measurement of X-Ray Pulse Widths by Intensity Interferometry," Phys. Rev. Lett. **88,** 244801 (2002).

[117] J. Itatani, F. Quéré, G. L. Yudin, M. Y. Ivanov, F. Krausz, and P. B. Corkum, "Attosecond Streak Camera," Phys. Rev. Lett. **88,** 173903 (2002).

[118] S. Neppl, D. Menzel, P. Feulner, R. Ernstorfer, R. Kienberger, A. L. Cavalieri, E. Magerl, M. Stanislawski, N. Karpowicz, and F. Krausz, "Attosecond-Time-Resolved Studies of Electron Dynamics on Surfaces," Ultrafast Phenomena XVII p. FA2 (2010).

[119] Y. Mairesse and F. Quéré, "Frequency-resolved optical gating for complete reconstruction of attosecond bursts," Phys. Rev. A **71,** 011401 (2005).

[120] J. Gagnon, E. Goulielmakis, and V. Yakovlev, "The accurate FROG characterization of attosecond pulses from streaking measurements," Appl. Phys. B-Lasers O. **92,** 25–32 (2008).

[121] J. Gagnon and V. S. Yakovlev, "The robustness of attosecond streaking measurements," Opt. Express **17,** 17678–17693 (2009).

[122] R. Trebino, K. W. DeLong, D. N. Fittinghoff, J. N. Sweetser, M. A. Krumbügel, B. A. Richman, and D. J. Kane, "Measuring ultrashort laser pulses in the time-frequency domain using frequency-resolved optical gating," Rev. Sci. Instrum. **68,** 3277–3295 (1997).

[123] courtasy to Stefan Neppl.

[124] E. Louis, A. E. Yakshin, P. C. Goerts, S. Oestreich, R. Stuik, E. L. G. Maas, M. J. H. Kessels, F. Bijkerk, M. Haidl, S. Muellender, M. Mertin, D. Schmitz, F. Scholze, and G. Ulm, "Progress in Mo/Si multilayer coating technology for EUVL optics,", Sematech Workshop on EUVL, 2000.

[125] S. Hendl, Ph.D. thesis, Universität Bielefeld, Januar 2009.

[126] I. V. Kozhevnikov, L. L. Balakireva, A. I. Fedorenko, I. A. Kopealets, V. E. Levashov, A. N. Stetsenko, I. I. Struk, and A. V. Vinogradov, "Synthesis and measurement of Os—Si multilayer mirrors optimized for the wavelength 380 Å," Opt. Commun. **125,** 13 – 17 (1996).

[127] S. Bajt, D. Stearns, and P. Kearne, "Investigation of the amorphous-to-crystalline transition in Mo/Si multilayers," J. Appl. Phys. **90,** 1017–1025 (2001).

[128] K. M. Skulina, C. S. Alford, R. M. Bionta, D. M. Makowiecki, E. M. Gullikson, R. Soufli, J. B. Kortright, and J. H. Underwood, "Molybdenum/beryllium multilayer mirrors for normal incidence in the extreme ultraviolet," Appl. Opt. **34,** 3727–3730 (1995).

[129] B. Sae-Lao and C. Montcalm, "Molybdenum–strontium multilayer mirrors for the 8–12-nm extreme-ultraviolet wavelength region," Opt. Lett. **26,** 468–470 (2001).

[130] S. Braun, R. Dietsch, M. Haidl, T. Holz, H. Mai, S. Müllender, and R. Scholz, "Mo/Si-multilayers for EUV applications prepared by Pulsed Laser Deposition (PLD)," Microelectron. Eng. **57-58,** 9 – 15 (2001).

[131] K. Siraj, M. K. ur Rahman, M. Rafique, M. Munawar, S. Naseem, and S. Riaz, "Pulsed laser deposition and characterization of multilayer metal-carbon thin films," Appl. Surf. Sci. **257,** 6445 – 6450 (2011).

[132] F. Hamelmann, G. Haindl, J. Schmalhorst, A. Aschentrup, E. Majkova, U. Kleineberg, U. Heinzmann, A. Klipp, P. Jutzi, A. Anopchenko, M. Jergel, and S. Luby, "Metal oxide/silicon oxide multilayer with smooth interfaces produced by in situ controlled plasma-enhanced MOCVD," Thin Solid Films **358,** 90–93 (2000).

[133] M. Grigonis and Émile J. Knystautas, "C/Si multilayer mirrors for the 25–30-nm wavelength region," Appl. Opt. **36,** 2839–2842 (1997).

[134] K. Sakano and M. Yamamoto, "Development of soft x-ray multilayer mirrors for a wavelength of 3 nm," P. Soc. Photo-Opt. Ins. **3767,** 238–241 (1999).

[135] T. Chassé, H. Neumann, B. Ocker, M. Scherer, W. Frank, F. Frost, D. Hirsch, A. Schindler, G. Wagner, M. Lorenz, G. Otto, M. Zeuner, and B. Rauschenbach, "Mo/Si multilayers for EUV lithography by ion beam sputter deposition," Vacuum **71,** 407 – 415 (2003), symposium on Plasma Surface Engineering at the Spring Meeting of the German Physical Society, Regensburg, Germany, March 11-15 2002.

[136] A. J. Devasahayam, *Nexus IBD Sales Presentation*, Veeco Instruments, 2002.

[137] photographs in courtasy to Thorsten Naeser.

[138] G. Aston and H. R. Kaufman, "Ion beam divergence characteristics of three-grid accelerator systems," International Electric Propulsion Conference p. 16 (1978).

[139] K. H., D. Röder, and V. Karanov, 2008, private email communication.

[140] J. F. Ziegler, U. Littmark, and J. P. Biersack, *The stopping and range of ions in solids* (Pergamon, New York :, 1985), p. 321 p. :.

[141] U. Kleineberg, 2008, private communication.

[142] D. Ksenzov, Ph.D. thesis, Universität Siegen, 2010.

[143] E. M. Gullikson, S. Mrowka, and B. B. Kaufmann, "Recent Developments in EUV Reflectometry at the Advanced Light Source," **4343,** 363–373 (2001).

[144] F. Schaefers, M. Mertin, and M. Gorgoi, "KMC-1: A high resolution and high flux soft x-ray beamline at BESSY," Review of Scientific Instruments **78,** 123102 (2007).

[145] A.-N. Jens and M. Des, *Elements of Modern X-ray Physics* (John Wiley and Sons LTD, 2001).

[146] A. K. J. Zuerner, Doeblinger, C. M., Braeuchle, and Bein, "Visualizing single-molecule diffusion in mesoporous materials," Nature **450,** 705–708 (2007).

[147] F. Company, "Datasheet supplied by FEI," Titan$^{\text{TM}}$ S/TEM Family-The World's Most Advanced S/TEM Solutions (2006).

[148] H. G. Tompkins and E. A. Irene, *Handbook of ellipsometry* (William Andrew Publishing/ Springer Verlag GmbH, 2005).

[149] *Easy-to-Use Acquisition/Analysis Software for Spectroscopic Ellipsometry (EASE^{TM})*, 1.16 ed., J. A. Woollam Co., Inc.

[150] M. Cardona and L. Ley, *Photoemission in Solids I. General Principles*, photoemission in solids 1. ed. (Springer-Verlag Berlin; New York, 1978), .

[151] J. C. Fuggle and N. Mårtensson, "Core-Level Binding Energies in Metals," J. Electron Spectrosc. Relat. Phenom. 21 (1980).

[152] J. A. Bearden and A. F. Burr, "Reevaluation of X-Ray Atomic Energy Levels," Rev. Mod. Phys. **39,** 125–142 (1967).

[153] R. Soufli and E. M. Gullikson, "Absolute photoabsorption measurements of molybdenum in the range 60 to 930 eV for optical constant determination," Appl. Opt. 37 (1998).

[154] R. Soufli and E. M. Gullikson, "Reflectance measurements on clean surfaces for the determination of optical constants of materials in the EUV/soft x-ray region," Appl. Opt. 36 (1997).

[155] R. Soufli, A. L. Aquila, F. Salmassi, M. Fernández-Perea, and E. M. Gullikson, "Optical constants of magnetron-sputtered boron carbide thin films from photoabsorption data in the range 30 to 770 eV," Appl. Opt. **47,** 4633–4639 (2008).

[156] A. Aquila, F. Salmassi, E. Gullikson, F. Eriksson, and J. Birch, "Measurements of the Optical Constants of Scandium in the 50-1300eV Range," Proceedings of SPIE, Optical Constants of Materials for UV X-Ray Wavelength **5538,** 64 (2004).

[157] Y. A. Uspenskii, J. Seely, N. Popov, A. Vinogradov, Y. Pershin, and V. Kondratenko, "Efficient method for the determination of extreme ultraviolet optical constants in reactive materials: application to scandium and titanium," J. Opt. Soc. Am. A 21 (2004).

[158] B. L. Henke, E. M. Gullikson, and J. C. Davis, "X-Ray Interactions: Photoabsorption, Scattering, Transmission, and Reflection at E = 50-30,000 eV, Z = 1-92," Atom. Data Nucl. Data **54,** 181–342 (1993).

[159] R. L. Kronig, "On the theory of dispersion of X-rays," J. Opt. Soc. Am. **12,** 547–556 (1926).

[160] H. A. Kramers, "La Diffusion de la Lumière par les Atomes," Atti. Congr. Intern. Fis. Como. **2,** 545–557 (1927).

[161] B. Kjornrattanawanich, D. L. Windt, J. A. Bellotti, and J. F.Seely, "Measurement of dysprosium optical constants in the 2-830 eV spectral range using a transmittance method, and compilation of the revised optical constants of lanthanum, terbium, neodymium, and gadolinium," Appl. Opt. **48,** 3084–3093 (2009).

[162] J. F. Seely, Y. A. Uspenskii, B. Kjornrattanawanich, and D. L. Windt, "Coated photodiode technique for the determination of the optical constants of reactive elements: La and Tb," Advances in X-Ray/EUV Optics, Components, and Applications **6317,** 63170T (2006).

[163] M. Altarelli, D. L. Dexter, H. M. Nussenzveig, and D. Y. Smith, "Superconvergence and Sum Rules for the Optical Constants," Phys. Rev. B **6,** 4502–4509 (1972).

[164] E. Chi, J. Shim, J. Kwak, and H. Baik, "Silicide formation by solid-state diffusion in MO/Si multilayer thin films," J. Mater. Sci **31,** 3567–3572 (1996).

[165] P. B. Corkum and F. Krausz, "Attosecond science," Nature Physics **3,** 381–387 (2007).

[166] T. Rohwer, S. Hellmann, M. Wiesenmayer, C. Sohrt, A. Stange, B. Slomski, A. Carr, Y. Liu, L. M. Avila, M. Kallane, S. Mathias, L. Kipp, K. Rossnagel, and M. Bauer, "Collapse of long-range charge order tracked by time-resolved photoemission at high momenta," Nature advance online publication (2011).

[167] Y. A. Uspenskii, V. E. Levashov, A. V. Vinogradov, A. I. Fedorenko, V. V. Kondratenko, Y. P.Pershin, E. N. Zubarev, S. Mrowka, and F. Schäfers, "Sc-Si normal incidence mirrors for a VUV interval of 35-50 nm," Nucl. Instrum. Meth. A **448,** 147–151 (2000).

[168] E. Goulielmakis, M. Schultze, M. Hofstetter, M. Uiberacker, J. Gagnon, V. Yakovlev, U. Kleineberg, and F. Krausz, "Sub-100-as soft x-ray pulses," Ultrafast Phenomena XVI **92,** 3–5 (2009).

[169] E. Goulielmakis, M. Schultze, F. Reiter, U. Graf, J. Gagnon, M. Hofstetter, V. Yakovlev, R. Kienberger, U. Kleineberg, and F. Krausz, "En route to the generation and attosecond control of intense single-cycle light pulses," LEOS Annual Meeting Conference Proceedings (2009).

[170] M. Hofstetter, A. Aquila, M. Schultze, Guggenmos, S. Yang, E. Gullikson, M. Huth, B. Nickel, J. Gagnon, V. S. Yakovlev, E. Goulielmakis, F. Krausz, and U. Kleineberg, "Lanthanum-molybdenum multilayer mirrors for attosecond pulses between 80 and 130 eV," New J. Phys. 13 (2011).

[171] S. Bajt, "Molybdenum–ruthenium/beryllium multilayer coatings," J. Vac. Sci. Technol. A **18,** 557–559 (2000).

[172] C. Montcalm, B. T. Sullivan, S. Duguay, M. Ranger, W. Steffens, H. Pépin, and M. Chaker, "In situ reflectance measurements of soft-x-ray/extreme-ultraviolet Mo/Y multilayer mirrors," Opt. Lett. **20,** 1450–1452 (1995).

[173] T. W. Barbee, S. Mrowka, and M. C. Hettrick, "Molybdenum-silicon multilayer mirrors for the extreme ultraviolet," Appl. Opt. **24,** 883–886 (1985).

[174] J. Gagnon, K. Lee, D. Rayner, P. Corkum, and V. Bhardwaj, "Coincidence imaging of polyatomic molecules via laser-induced Coulomb explosion," J. Phys. B-At. Mol. Opt. **41,** 215104 (2008).

[175] Y. Ménesguen, S. de Rossi, E. Meltchakov, and F. Delmotte, "Aperiodic multilayer mirrors for efficient broadband reflection in the extreme ultraviolet," App. Phys. A-Mater. **98,** 305–309 (2010).

[176] M. Kitzler, N. Milosevic, A. Scrinzi, F. Krausz, and T. Brabec, "Quantum Theory of Attosecond XUV Pulse Measurement by Laser Dressed Photoionization," Phys. Rev. Lett. **88,** 173904,173905 (2002).

[177] S. Kaesdorf, "http://www.kaesdorf.de/,".

[178] J. Gagnon and V. Yakovlev, "The direct evaluation of attosecond chirp from a streaking measurement," Appl. Phys. B-Lasers O. pp. 1–7 (2011).

[179] A. P. Zwicker, S. P. Regan, M. Finkenthal, H. W. Moos, E. B. Saloman, R. Watts, and J. R. Roberts, "Peak reflectivity measurements of W/C, Mo/Si, and Mo/B4C multilayer mirrors in the 8–190-Å range using both Kα line and synchrotron radiation," Appl. Opt. **29,** 3694–3698 (1990).

[180] D. Häussler, E. Spiecker, W. Jäger, M. Störmer, R. Bormann, C. Michaelsen, J. Wiesmann, G. Zwicker, R. Benbalagh, J.-M. Andre, and P. Jonnard, "Quantitative TEM characterizations of La/B4C and Mo/B4C ultrathin multilayer gratings by the geometric phase method," Microelectron. Eng. **84,** 454 – 459 (2007), nanoscale imaging and metrology of devices and innovative materials, Procedings of the European Materials Research Society 2006 symposium F.

[181] K. V. Popov, J. A. Dobrowolski, A. V. Tikhonravov, and B. T. Sullivan, "Broadband high-reflection multilayer coatings at oblique angles of incidence," Appl. Opt. **36,** 2139–2151 (1997).

[182] R. Szipöcs, K. Ferencz, C. Spielmann, and F. Krausz, "Chirped multilayer coatings for broadband dispersion control in femtosecond lasers," Opt. Lett. **19,** 201–203 (1994).

[183] V. Pervak, I. Ahmad, M. K. Trubetskov, A. V. Tikhonravov, and F. Krausz, "Double-angle multilayer mirrors with smoothdispersion characteristics," Opt. Express **17,** 7943–7951 (2009).

[184] courtesy to Elisabeth Magerl.

[185] L.-Y. Peng, F. Tan, Q. Gong, E. A. Pronin, and A. F. Starace, "Few-cycle attosecond pulse chirp effects on asymmetries in ionized electron momentum distributions," Phys. Rev. A **80,** 013407 (2009).

[186] Y. Li, J. Lewellen, Z. Huang, V. Sajaev, and S. V. Milton, "Time-Resolved Phase Measurement of a Self-Amplified Free-Electron Laser," Phys. Rev. Lett. **89,** 234801 (2002).

Abbreviations

List of abbreviations used throughout this thesis:

Elements

Mo	Molybdenum
Si	Silicon
La	Lanthanum
B_4C	Boron carbide
Sc	Scandium
Zr	Zirconium
Be	Beryllium
Pd	Palladium
Kr	Krypton
Ar	Argon
Sr	Strontium
Y	Yttrium
Xe	Xenon
Mn	Manganese

Units:

as	attosecond
fs	femtosecond
nm	nanometer
cm	centimeter
mm	millimeter
eV	electron volt
keV	kilo electron volt
$mbar$	millibar

Technical terms:

IR	infrared
VIS	visible
UV	ultraviolet
XUV	(also EUV) extreme ultraviolet radiation
$CE(P)$	carrier envelope (phase)
$HH(G)$	high harmonic (generation)
GD	group delay
GDD	group delay dispersion
TOD	third order dispersion
XRR	X-ray reflectometry
$FROG$	frequency resolved optical gating
$(-CRAB)$	(for complete reconstruction of attosecond bursts)
IBD	ion beam deposition
PBN	plasma bridge neutralizer
RF	radio frequency
CPA	chirped pulse amplification
FEL	free electron laser
MSE	mean square error
$FWHM$	full width at half maximum
rpm	rounds per minute

Institutions:

LMU	Ludwig-Maximillians-Universität München
MPQ	Max Planck Institut für Quantenoptik
$CXRO$	Center for X-ray Optics
ALS	Advance Light Source
$BESSY$	Berliner Elektronenspeicherring-Gesellschaft für Synchrotronstrahlung
$LCLS$	Linac Coherent Light Source

Acknowledgments

First of all, I would like to express my thanks to my advisor Professor Ulf Kleineberg for giving me the opportunity to graduate in this great research environment. He supported me throughout my PHD with his knowledge and ideas and provided conditions, which allowed me to work autonomously and to take responsibility. The close collaboration and the short communication paths to Ferenc Krausz and all attosecond beam-line colleagues enabled the iterative optimization of optics for the generation of attosecond pulses, taylor-made for each individual experiment and was one important reason for many successful results presented in this thesis.

My special thanks go to my colleague and successor Alexander Guggenmos, for his input, dedication, enthusiasm and friendship in the last year of my PHD. I had the pleasure to be in a group together with nice colleges Casey SooHoon Chew, Jürgen Schmidt, Ralph Kleinschek, Michael Kranjec, Chrisitian Späth and Jingquan Lin with many fruitful discussions and ideas in a motivating working environment. I had a great time with Andrew Aquila, together with whom I was working on different projects between Munich and Berkeley and who was always most helpful in discussions.

I would like to thank the attosecond beam-line colleagues, first of all Martin Schultze for his fair and friendly support throughout my PHD, for information, data and discussions. The dedicated work of Markus Fieß, Martin Schultze and Benjamin Dennhardt provided a perfectly running AS2 beamline to carry out the "dispersive control by multilayer mirror" experiment. Further thanks to Eleftherios Goulielmakis for his support, his ideas, his staying power and dedication, Matthias Uiberacker for a fantastic introduction, Ralph Ernstorfer, Elisabeth Magerl, Elisabeth Bothschafter, Stefan Neppl, Wolfram Helml, Agustin Schiffrin, Nicholas Karpowicz and Adrian Cavalieri for the great and friendly collaboration in AS3 experiments, further, Matthias Kling, Adrian Wirth, Irina Znakovskaya, Boris Bergues, Mohammed Hassan and Sergey Zherebtsov and all other collaborators involved in joint experiments and discussions for their ideas and the friendly working atmosphere, and last but not least to Reinhard Kienberger for supervising many experiments and being always there to help with any questions.

My work was supported by theory assistance and informative discussions

Peer-Reviewed Publications by the Author

M. Schultze, E. Goulielmakis, M. Uiberacker, <u>M. Hofstetter</u>, J. Kim, D. Kim, F. Krausz, and U. Kleineberg. Powerful 170-attosecond xuv pulses generated with few-cycle laser pulses and broadband multilayer optics. *New Journal of Physics*, 9(7):243, 2007.

E. Goulielmakis, M. Schultze, M. Uiberacker, <u>M. Hofstetter</u>, U. Kleineberg, and F. Krausz. Isolated 170 as pulse generation in the *XUV*. *Acta Physica Polonica*, 112, 751, 2007.

E. Goulielmakis, M. Schultze, <u>M. Hofstetter</u>, V. S. Yakovlev, J. Gagnon, M. Uiberacker, A. L. Aquila, E. M. Gullikson, D. T. Attwood, R. Kienberger, F. Krausz, and U. Kleineberg. Single-Cycle Nonlinear Optics. *Science*, 320(5883): 1614-1617, 2008.

M. Schultze, M. Fieß, N. Karpowicz, J. Gagnon, M. Korbman, <u>M. Hofstetter</u>, S. Neppl, A. L. Cavalieri, Y. Komninos, T. Mercouris, C. A. Nicolaides, R. Pazourek, S. Nagele, J. Feist, J. Burgdörfer, A. M. Azzeer, R. Ernstorfer, R. Kienberger, U. Kleineberg, E. Goulielmakis, F. Krausz, and V. S. Yakovlev. Delay in photoemission. *Science*, 328(5986):1658-1662, 2010.

<u>M. Hofstetter</u>, M. Schultze, M. Fieß, A. Guggenmos, J. Gagnon, E. Magerl, E. Bothschafter, R. Ernstorfer, R. Kienberger, E. Gullikson, F. Krausz, and U. Kleineberg. First attosecond pulse control by multilayer mirrors above 100 eV photon energy. in *International Conference on Ultrafast Phenomena*, PDP8. Optical Society of America, 2010.

M. Fieß, M. Schultze, E. Goulielmakis, B. Dennhardt, J. Gagnon, M. Hofstetter, R. Kienberger, and F. Krausz. Versatile apparatus for attosecond metrology and spectroscopy. *Review of Scientific Instruments*, 81(9):093103, 2010.

M. Hofstetter, M. Schultze, M. Fieß, B. Dennhardt, A. Guggenmos, J. Gagnon, V. S. Yakovlev, E. Goulielmakis, R. Kienberger, E. M. Gullikson, F. Krausz, and U. Kleineberg. Attosecond dispersion control by extreme ultraviolet multilayer mirrors *Optics Express*, 19(3):1767-1776, 2011.

M. Schultze, A. Wirth, I. Grguras, M. Uiberacker, T. Uphues, A. Verhoef, J. Gagnon, M. Hofstetter, U. Kleineberg, E. Goulielmakis, and F. Krausz. State-of-the-art attosecond metrology. *Journal of Electron Spectroscopy and Related Phenomena*, 184(3-6):68 -77, 2011.

E. Magerl, S. Neppl, A. L. Cavalieri, E. Bothschafter, M. Stanislawski, T. Uphues, M. Hofstetter, U. Kleineberg, J. V. Barth, D. Menzel, F. Krausz, R. Ernstorfer, R. Kienberger, and P. Feulner. A flexible apparatus for attosecond photoelectron spectroscopy of solids and surfaces. *Review of Scientific Instruments*, 82:6, 2011.

M. Hofstetter, A. Aquila, M. Schultze, A. Guggenmos, S. Yang, E. Gullikson, M. Huth, B. Nickel, J. Gagnon, V. S. Yakovlev, E. Goulielmakis, F. Krausz, and U. Kleineberg. Lanthanum-molybdenum multilayer mirrors for attosecond pulses between 80 and 130 eV. *New Journal of Physics*, 13:063038, 2011.